Observations of small-scale flows in sunspot penumbrae

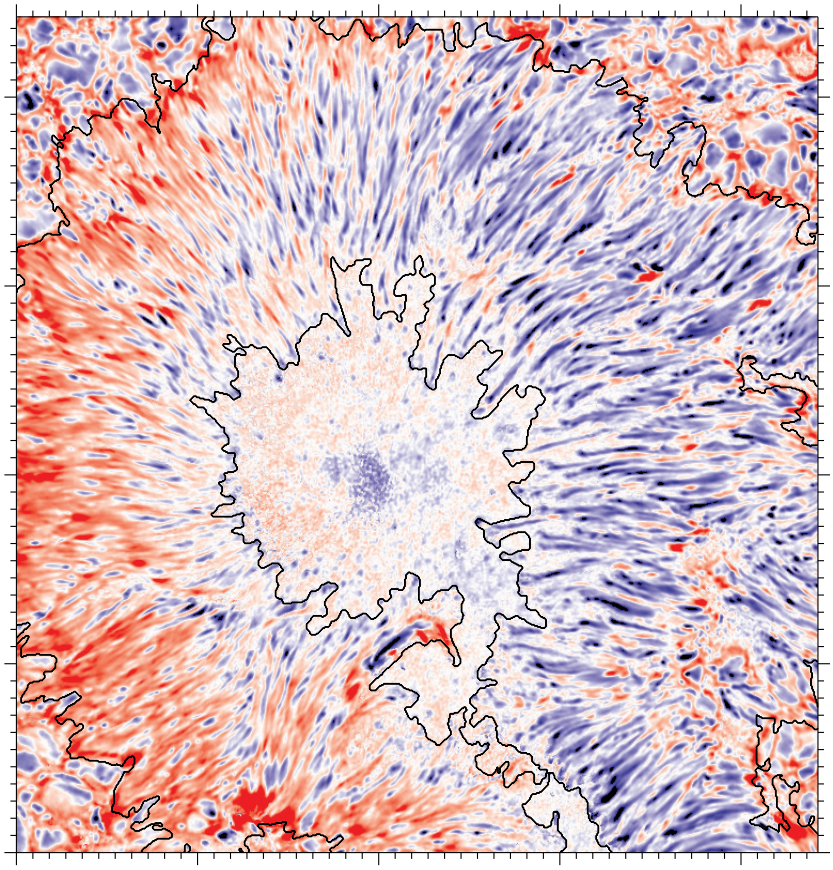

Sara Esteban Pozuelo

INSTITUTO Đ ASTROFÍSICA Đ ANDALUCÍA

Consejo Superior de Investigaciones Científicas

Programa de Doctorado

FÍSICA Y CIENCIAS DEL ESPACIO

Universidad de Granada

Observations of small-scale flows in sunspot penumbrae

Memoria que presenta
Dña. Sara Esteban Pozuelo
para obtener el grado de
Doctora en Astrofísica.

Director de tesis
Dr. D. Luis R. Bellot Rubio

INSTITUTO Đ ASTROFÍSICA Đ ANDALUCÍA

Consejo Superior de Investigaciones Científicas

Editor: Universidad de Granada. Tesis Doctorales
Autora: Sara Esteban Pozuelo
ISBN: 978-84-9125-478-2
URI: http://hdl.handle.net/10481/42207

La doctoranda Sara Esteban Pozuelo y el director de la tesis Dr. Luis R. Bellot Rubio. Garantizamos, al firmar esta tesis doctoral, que el trabajo ha sido realizado por el doctorando bajo la dirección del director de la tesis y hasta donde nuestro conocimiento alcanza, en la realización del trabajo, se han respetado los derechos de otros autores a ser citados, cuando se han utilizado sus resultados o publicaciones.

Granada, 25 de Noviembre 2015

Director de la Tesis

Fdo.: Dr. Luis R. Bellot Rubio

Doctorando

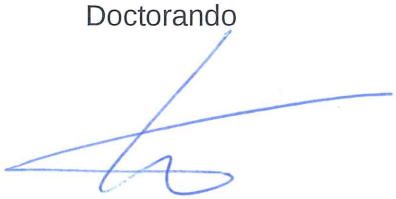

Fdo.: Sara Esteban Pozuelo

Don't ever let somebody tell you
you can't do something, not even me.
Alright? Your dream, you gotta protect it.
People can't do something themselves,
they wanna tell you you can't do it.
If you want something, go get it.

Chris Gardner to his son,
from 'The Pursuit of Happiness'

Contents

Resumen

Esta tesis estudia la evolución temporal y las propiedades físicas de los flujos de pequeña escala en la penumbra de las manchas solares desde un punto de vista observacional.

La penumbra es un medio magnetizado en el que el transporte convectivo debería estar inhibido. Sin embargo, se observa como una región repleta de filamentos brillantes de diferentes tamaños que evolucionan en cuestión de minutos, lo que conlleva a la pregunta de cómo se transporta la materia en la penumbra. Desde el descubrimiento del efecto Evershed en 1909, modelos teóricos y estudios observacionales han tratado de explicar qué ocurre en la penumbra. Sin embargo, estos no han podido explicar totalmente las observaciones. Recientemente, se han realizado simulaciones magnetohidrodinámicas en tres dimensiones que permiten probar los modelos y compararlos con las observaciones. Los resultados de las últimas simulaciones publicadas apoyan que la convección por rebosamiento (Scharmer et al., 2008) es la responsable del movimiento del flujo penumbral que continúa siendo cuestionada debido a la necesidad de deconvolucionar los datos con parámetros inciertos para detectar la presencia de downflows laterales. Además, los downflows supersónicos en la penumbra continúan siendo objeto de debate. Gracias a las mejoras en instrumentación, se han podido caracterizar con más detalle y conocer más aspectos de estos. Sin embargo, (van Noort et al., 2013) describe downflows supersónicos con velocidades del orden de 20 km s^{-1} y campos magnéticos de 7 kG, siendo los valores más altos obtenidos en la penumbra y generando ciertas dudas en la comunidad.

Lo novedoso de esta tesis es el uso de secuencias temporales de datos espectropolarimétricos en la línea Fe I 6173 Å de alta resolución espacial y cadencia ($\sim 0\farcs15$ y 32 s, respectivamente) obtenidos con el espectropolarímetro CRISP en el Telescopio Solar Sueco (SST). Esto permite estudiar movimientos de flujo de pequeña escala y, además, resolver espacialmente estructuras. Además, la utilización de secuencias temporales permite filtrar las oscilaciones subsónicas que introducen un patrón indeseado en el campo de velocidad, especialmente cuando se buscan señales débiles.

Mediante el cálculo de velocidades en la línea de visión (LOS) utilizando la técnica de los bisectores y el filtrado de estas, hemos detectado downflows laterales por toda la penumbra. Esta es la primera vez que se consigue sin utilizar datos deconvolucionados de luz difusa. Los downflows laterales aparecen cerca o en los bordes de los filamentos penumbrales y se mueven acompañando a los canales de flujo a los que están asociados. Son intermitentes, produciéndose continuamente uniones y fragmentaciones. La velocidad de los downflows laterales es muy pequeña, del orden de 200 m s^{-1}, su tiempo de vida es de 6 minutos y se desplazan hacia el exterior de la mancha. Gracias a la inversión de los perfiles de los cuatro parámetros de Stokes, hemos podido caracterizar también su campo magnético. La intensidad del campo magnético es de unos 1.5 kG. La inclinación no sugiere la presencia de polaridad opuesta, pero al inspeccionar los perfiles de Stokes V hemos observado la existencia de un lóbulo rojo adicional que sugiere la presencia de campos de polaridad opuesta. La convección por rebosamiento, los rollos convectivos (Danielson, 1961) y los tubos de flujo helicoidal (Borrero, 2007) son compatibles con los resultados, aunque se prioriza a la convección por rebosamiento porque está apoyada por las simulaciones. Sin embargo, la velocidad que se obtienen en las simulaciones son mayores que en las observaciones lo que genera ciertas dudas. Es importante destacar que en las simulaciones aparece una inversión de polaridad entre $\tau = 1$ y 0.1 y que sería interesante observar para poder relacionar los downflows laterales con flujos de polaridad opuesta.

A partir de la inversión de dos componentes en píxeles de parches que albergan downflows supersónicos hemos caracterizado sus propiedades físicas y su evolución temporal. Estos parches aparecen en la penumbra media y externa, se mueven hacia el exterior. Estos coinciden con estructuras brillantes situadas al final de filamentos. Los downflows supersónicos se caracterizan por tener velocidades fuertes ($\sim$8 km s^{-1}) y campos magnéticos de unos 1.5 kG con polaridad opuesta a la de la mancha (45°). Su tiempo de vida oscila de uno a diez minutos y pueden ser recurrentes. Los parches que los albergan pueden unirse o fragmentarse, variando su velocidad, forma e intensidad. Según estos resultados, los downflows supersónicos podrían ser frenados abruptamente en capas inferiores más densas produciéndose un choque. Como consecuencia, habría un aumento de la temperatura hacia arriba, apareciendo estructuras más brillantes.

Summary

In this thesis we analyze the temporal evolution and the physical properties of small-scale flux in sunspot penumbrae.

The penumbra is a magnetized medium where convection should be inhibited. However, it is observed as a plethora of bright filaments of different sizes that evolve in a few minutes, leading us to ask how matter moves in the penumbra. Since the discovery of the Evershed flow in 1909, theoretical models and observational studies have attempted to explain what it is happening in the penumbra, but none have totally explained observations. Recently, 3D MHD simulations have enable us to test models and to compare them with observations. Results from the latest published simulations support overturning convection (Scharmer et al., 2008) as the responsible of the penumbral flow motions, which is begin questioned due to the necessity of deconvolve data with uncertain parameters for stray light compensation in order to detect the presence of lateral downflows. In addition, supersonic downflows in the penumbra are still a matter of debate. Thanks to improvements in instrumentation, they have been characterized in detail and more aspects are known. Nevertheless, (van Noort et al., 2013) have described supersonic downflows with LOS velocities of order 20 km s^{-1} and magnetic field strengths of about 7 kG, being these values the greatest ever obtained in the penumbra and raising doubts in the community.

A novel aspect of this thesis is the use of time sequences of high spatial resolution and high cadence spectropolarimetric data of the Fe I 6173Å spectral line obtained with the CRISP spectropolarimeter at the Swedish 1-m Solar Telescope (SST). This enables us to study small-scale flow motions and, moreover, spatially resolve structures. In addition, time series allow us to filter for subsonic oscillations that introduce an undesired imprint in the velocity field, specifically when searching for weak signals.

By means of line-of-sight (LOS) velocities using the bisector technique and filtering them for subsonic oscillations, we have detected lateral downflows throughout the penumbra. This is the first time that it is achieved without using stray light compensated data. Lateral downflows appear close

or at the edges of the penumbral filaments and move according to the flow channel which is associated with. They are intermittent, occurring permanently mergings and fragmentations. The LOS velocity of the lateral downflows is very weak, of order 200 m s^{-1}, their lifetime is of 6 minutes and they move outward. Through their four Stokes profiles inversion, we have characterized also their magnetic field. The magnetic field strength is of about 1.5 kG. Their inclination does not suggest the presence of inverse polarity, but after examining the Stokes V profiles we have observed the existence of an additional red lobe that suggests the presence of reverse-polarity magnetic fields. The overturning convection, the convective rolls (Danielson, 1961) and the twisted flux magnetic tubes (Borrero, 2007) are compatible with our results, although we prioritize the overturning convection because it is supported by simulations. However, the velocity obtained from simulations are greater than that from observations, which raises doubts. It is important to emphasize that simulations show a polarity inversion between $\tau = 1$ and 0.1, and it might be interesting to study in order to relate lateral downflows with inverse-polarity fields.

From two-component inversions of the pixels within patches harboring supersonic downdlows, we have characterized their physical properties and their temporal evolution. These patches appear in the middle and outer penumbra and move outward. They coincide with bright intensity structures located at the end of penumbral filaments. The supersonic downflows are characterized for having strong LOS velocities ($\sim$8 km s^{-1}), magnetic field strengths of about 1.5 kG with opposite polarity to the sunspot (45°). Their lifetime varies between one and ten minutes, and can be recurrent. Patches harboring them undergo mergings and fragmentations, changing their LOS velocity, shape and intensity. According to these results, supersonic Evershed downflows might be abruptly stopped in lower and denser layers occurring a shock. As a consequence, there might produce a temperature enhancement going upward, appearing bright intensity structures.

1

Introduction

There are things known and there are things unknown,
and in between are the doors of perception.
Aldous Huxley

1.1 The photosphere

The photosphere is the most accesible layer of the Sun. The majority of the spectral lines in the visible solar spectrum are formed there. However, many of the features observed in this layer are not well understood. How magnetic flux appears and disappears, how sunspots are formed or how gas moves in sunspot penumbrae are some questions that are still debated.

Etymologically, the photosphere receives its name from Ancient Greek, *photos* ($\phi\omega\tau o\varsigma$) meaning light and *sphaira* ($\sigma\phi\alpha\iota\rho\alpha$) meaning sphere, in reference to the fact that it is a spherical surface emitting light. It is a layer a few hundred kilometers thick where the plasma changes from being almost completely opaque to transparent to electromagnetic radiation going outwards. Spectral lines are formed in the photosphere, allowing us to study the thermodynamic state, the chemical composition, and the dynamic and magnetic properties of the solar photosphere as a function of depth. Its effective temperature is about 5780 K, decreasing to roughly 4400 K in the temperature minimum region (the interface with the chomosphere above).

In intensity images of the solar photosphere one can see large structures produced by magnetic fields, such as sunspots. The left panel of Figure 1.1 shows active regions in a filtergram obtained with the Helioseismic and Magnetic Imager (HMI; Scherrer et al., 2012; Schou et al., 2012) onboard the Solar Dynamics Observatory (SDO; Pesnell et al., 2012). To detect more features due to the solar magnetism, one may use special filters or mag-

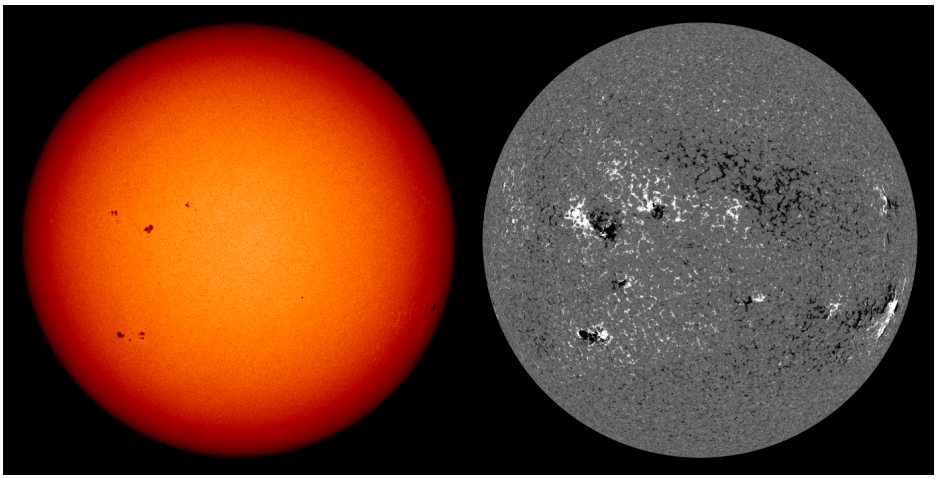

FIGURE 1.1:— Intensity image (left) and magnetogram (right) of the solar disk on September 24, 2015 at 15:06:54 UT. They were obtained by the HMI instrument onboard the SDO. Taken from http://umbra.nascom.nasa.gov/images/latest.html

netograms. As can be seen in the right panel of Figure 1.1, the strongest signals, corresponding to active regions, are located on both sides of the solar equator. They are surrounded by many magnetic patches that cover the solar surface forming the so-called photospheric network[1]. In these magnetograms, most of the solar surface seems to be nonmagnetic. This is the so-called quiet Sun.

Although the quiet Sun is an interesting research field, this thesis focuses on active regions, specifically on sunspots.

1.2 Sunspots

Humans have observed the Sun since long. Archaeological materials have revealed several antique myths concerning the vision of spots on the Sun. The first observations of sunspots might have done by the Ancient Chinese (13^{th} to mid 11^{th} century BC). Some time later, thanks to the high solar activity during the 5^{th} century BC, it is probable that Ancient Greeks observed sunspots (Yau, 1988). As a matter of fact, it is well known that the pre-Socratics were keen observers. The greek philosopher Anaxagoras of Clazomenai (500 - 428 BC) might have observed a spot in 467 BC as well as Aratus (315 - 240 BC) and Virgil (70 - 19 BC), who mentioned them in the ancient literature. However, none of the early observers could explain them. In addition, the high influence of Aristotle, who held the view that the Sun

[1]The network is produced by the concentration of magnetic flux at the boundaries of supergranular cells (e.g., Livingston & Harvey, 1975; Smithson, 1975). Supergranulation is a convective pattern visible on the solar surface on scales of ∼20 Mm.

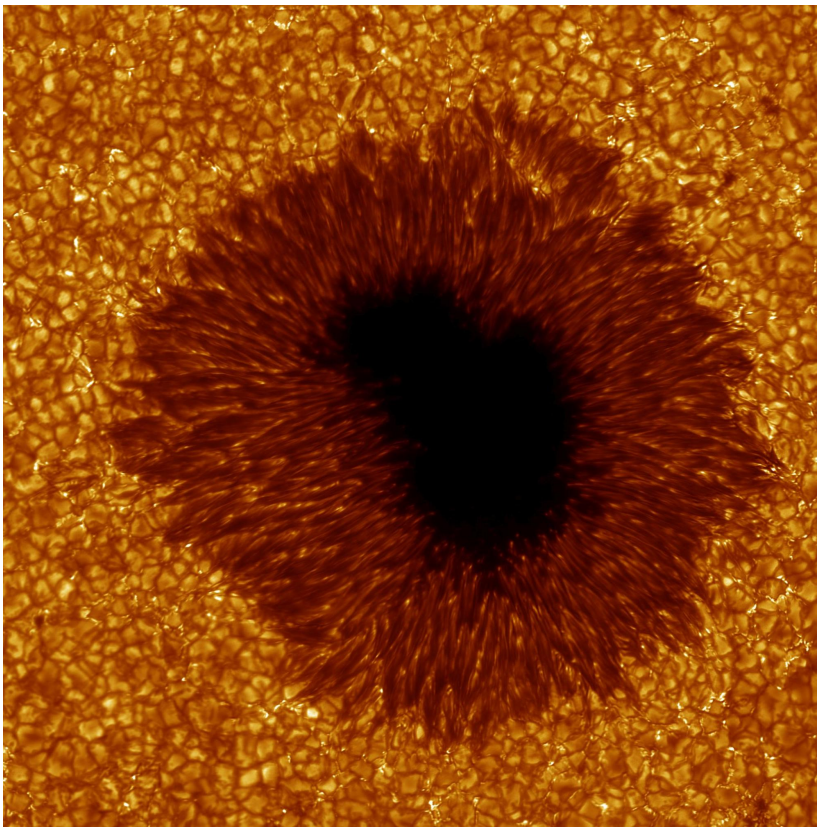

FIGURE 1.2:— G-Band image of a large regular sunspot observed at the Swedish 1-m Solar Telescope on July 3, 2003. Courtesy Institute for Solar Physics (Stockholm University).

and the heavens were ideal, interfered with the process of understanding. Thus, the first systematic recordings were performed by astronomers of the Ancient China during 28 BC.

Undoubtedly, the invention of telescope revolutionized astronomy. However, the first known instrumental observation of a sunspot was performed using a camera obscura by Kepler in May 1607[2]. The first telescopic observations of sunspots were probably done by T. Harriot in 1610, but were first published by J. Fabricius in the same year. In 1613, Galileo was the first to measure the positions and motions of sunspots over the solar disk.

At the beginning of the 20^{th} century, sunspots were the first astronomical objects that were related to magnetic fields (Hale, 1908). Today, it is known that sunspots are formed by magnetic flux tubes rising from the base of the convection zone into the photosphere. The intersection of these magnetic flux tubes with the solar photosphere is what we observe as sunspots.

A sunspot consists of two parts: a dark nucleus called the umbra and a

[2]Although he interpreted his observations as a transit of Mercury across the Sun.

brighter halo named the penumbra (see Figure 1.2).

1.2.1 Umbra

In the umbra, convective energy transport is inhibited because the magnetic field is large and almost vertical (Biermann, 1941; Cowling, 1953). This circumstance lowers its temperature to $T_{umbra}(\tau = 1) \sim 3500$ – 5000 K appearing darker than the quiet Sun. In the umbra, energy is transported by radiation. The magnetic field is oriented vertically with respect to the solar surface, except at the umbra-penumbra boundary where it is slightly inclined ($\gamma \sim 20$ – $40°$). The magnetic field strength ranges between 2000 and 3500 G, being stronger in big sunspots. For a more complete view of the umbra, we refer the reader to Solanki (2003) or Borrero & Ichimoto (2011).

The umbral fine structure is composed of umbral dots. These are roundish bright structures with typical sizes around $0\farcs2$. Although in principle convection is inhibited there, Ortiz et al. (2010) found that they manifest some sort of convective phenomena in the umbra.

1.2.2 Penumbra

Why sunspots have a penumbra and what processes occur there are still open questions. Understanding the structure, brightness and dynamics of the penumbra represents a challenge, because our ability to make progress strongly depends on improvements in the spatial resolution of the observations.

Usually, the penumbra is divided in three regions depending on their physical conditions: inner, mid and outer penumbra. According to Mathew et al. (2003), the magnetic field strength decreases from the umbra-penumbra boundary (2000–2500 G) to the outer penumbral edge (500–1000 G). The magnetic field inclination also suffers variations inside the penumbra. It increases from $40°$ in the inner penumbra to more than $90°$ in the outer penumbra, where the magnetic field lines return to the solar surface (e.g. Solanki, 2003). The temperature of the penumbra (around 5500 K at $\tau = 1$) is slightly lower than that of the quiet Sun.

The penumbral fine structure consists of a well-organized radial distribution of bright and dark filaments (Scharmer et al., 2002). Each filament is formed by a dark core flanked by two bright edges (see Figure 1.3). Time-resolved observations of penumbral filaments enable us to identify the dark core and its two lateral brightenings as an unity that has a proper motion (Sütterlin et al., 2004). Considering penumbral filaments taken near the umbra (where there is less clutter and penumbral filaments can be distinguished individually), their typical length is of order 3000 km and their width is 150 km. Their lifetimes range from 1 to 2 hours.

It is accepted that filaments start in bright, roundish structures called

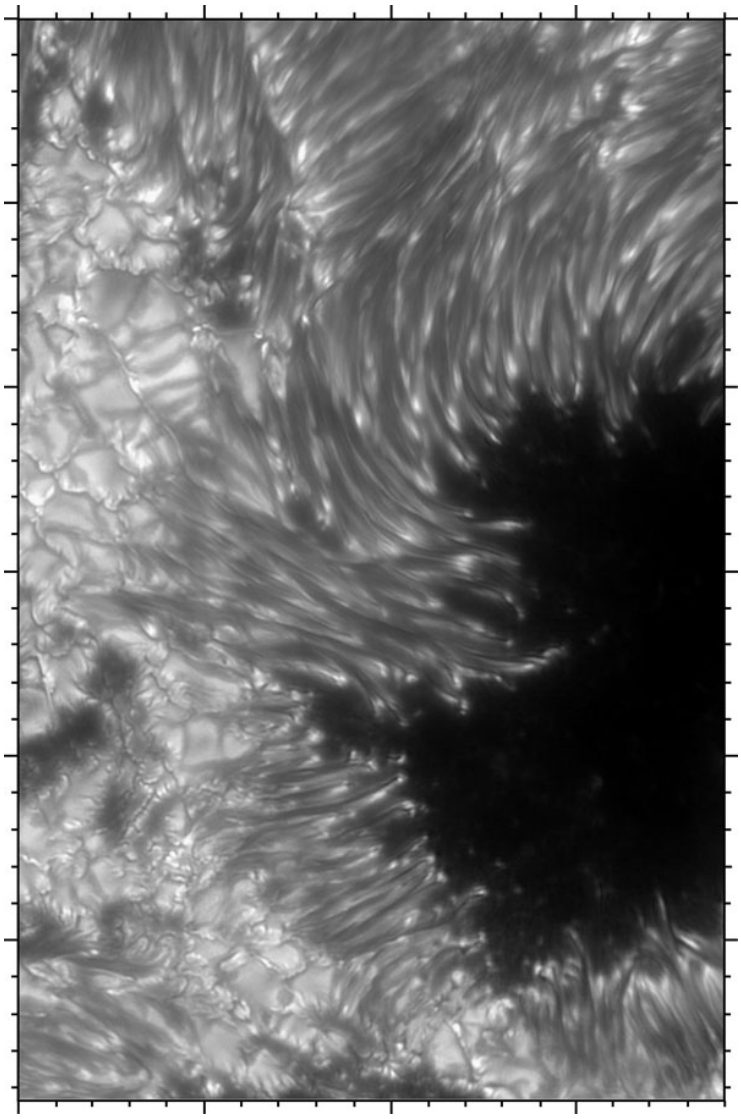

FIGURE 1.3:— Part of the largest spot in AR 10030 observed in the G-band with the Swedish 1-m Solar Telescope on July 15, 2002. From Scharmer et al. (2002).

penumbral grains. At that moment, the dark core of the penumbral filament is not present, and only a bright structure can be observed (Rouppe van der Voort et al., 2004). Penumbral grains are located at the head of the filaments (Figure 1.3). They show horizontal speeds around 0.5–1 km s^{-1}, but their direction of motion depends on their location. In the inner penumbra, they move radially toward the umbra (inward), whereas in the middle and outer penumbra they move outward (e.g. Sobotka & Sütterlin, 2001).

As mentioned before, the penumbral magnetic field is strong, so convection should be limited. However, the penumbra is observed as a bright

region, reaching an intensity of 75 % that of the quiet Sun. Therefore, the penumbra is hotter than the umbra. This raises another question: how enhanced brightness of the penumbra is produced.

1.3 The Evershed effect

At the Kodaikanal Observatory (India), Evershed (1909) observed several spectral lines in many sunspots located at different heliocentric angles (different radial distances from the center of the solar disk). Considering the Doppler shift, Evershed discovered an outward flow from the umbra to the outer penumbral boundary. This is the so-called Evershed effect. Besides, he found that its behavior varies on each side of the umbra. Observing in the center side penumbra[3], the lines were blueshifted, whereas on the limb side[4] they were shifted to the red.

Furthermore, Evershed (1909) demonstrated that the velocity associated with this flow increases radially toward the outer penumbra. Indeed, he found that there was a velocity maximum at the outer boundary and, then, the flow disappeared abruptly. More than 100 years later, the fate of the flow at the outer penumbral boundary is still a matter of debate. Some authors (e.g. Brekke & Maltby, 1963; Wiehr et al., 1986; Hirzberger & Kneer, 2001) also found a sharp decrease of the Evershed flow at the outer boundary of sunspots. In contrast, other authors (Küveler & Wiehr, 1985; Dialetis et al., 1985) did not observe evidence of an abrupt decrease. Sheeley (1972) pointed out the existence of a horizontal flow in regions surrounding sunspots. Later, Solanki et al. (1994) found that the sunspot magnetic field continues beyond the sunspot border, forming an extended canopy[5] that contains about 10 % of the Evershed flow. Pursuing this further, Rezaei et al. (2006) analyzed simultaneous full Stokes spectropolarimetric observations of different sunspots and their surroundings in visible and near-infrared neutral iron lines. They did not find any abrupt change within their spatial resolution (1″) and interpreted the radial outflow of the canopy as the continuation of a fraction of the penumbral Evershed flow. In addition, they demonstrated that there is a radial outflow beyond the sunspot related to the moat flow. However, in Solanki et al. (1994) and Rezaei et al. (2006), the remainder of the Evershed flow must disappear within the penumbral region to conserve mass.

[3] This is the penumbral region located closer to the solar disk center.

[4] Penumbral region that is closer to the solar limb.

[5] Outside the sunspot boundary, the magnetic field continues into the chromosphere and forms a magnetic canopy-like structure in the surroundings of the sunspot. According to Solanki et al. (1992), it rises with distance to the spot reaching a height of ∼800 km.

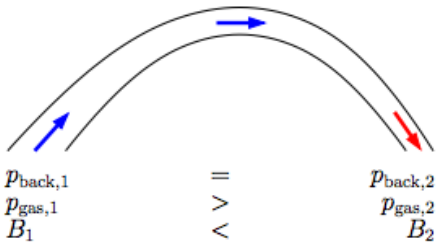

FIGURE 1.4:— Principle of the siphon flow mechanism. From Schlichenmaier (2002a).

1.4 Penumbral fine structure models

Penumbral fine structure models can be divided into two groups: those based on magnetic flux tubes and the gappy penumbral model. Each group is explained below.

1.4.1 Models based on magnetic flux tubes

The first model proposed to explain the Evershed flow was the siphon flow model (Meyer & Schmidt, 1968). According to it, a magnetic field strength difference between the footpoints of a flux tube induces a gas pressure difference[6]. Consequently, a gas flow directed toward the footpoint with lower gas pressure sets in (Figure 1.4). This means that the footpoint located further from the umbra must have a stronger magnetic field than that closer to the umbra to produce a radial outflow. However, the magnetic field strength decreases as the radial distance increases. To solve this shortcoming, Montesinos & Thomas (1997) proposed that the outer footpoint is located in a magnetic element outside the sunspot, for example in a so-called magnetic knot[7]. However, the siphon flow model does not completely explain the observations, leaving important issues unanswered, such as the dynamical character of the penumbral filaments or the origin of the magnetic field strength difference between footpoints.

In parallel, Jahn & Schmidt (1994) proposed a tripartite sunspot model where the enhanced brightness of the penumbra was produced by heat transfer through the magnetopause, i. e., the layer that separates the penumbra from the quiet Sun. This additional heat was distributed horizontally by interchange convection of magnetic flux tubes. Later, this idea was developed by Schlichenmaier et al. (1998) who proposed the so-called moving tube model. The model assumes a flux tube located below the photosphere that is heated and gains buoyancy, so it emerges into the photosphere where it loses

[6]It is assumed that the medium pressure at both footpoints is strictly the same.
[7]The magnetic field strength inside a magnetic knot is of order 1500 G (Spruit, 1981).

energy, cooling down as the Evershed flow is accelerated. At the same time, the inner footpoints migrate toward the umbra. Schlichenmaier (2002a) showed that such a tube adopts a sea-serpent shape due to magnetoconvective overshoot (see Schlichenmaier, 2003). This sea-serpent shape helps explain the disappearance of the flow, the penumbral heating problem, and the existence of supersonic velocities within the penumbra. A scheme of this model is shown in Figure 1.5.

Many theoretical models are based on a penumbra consisting of at least two magnetic components, as the Stokes profile shapes suggest. These components are referred to as *spines* and *intraspines* to distinguish the component harboring the more vertical and the more horizontal magnetic field, respectively (Lites et al., 1993). In the same year, Solanki & Montavon (1993) proposed the uncombed penumbral model. According to it, the penumbra is made up of horizontal magnetic flux tubes that carry most of the Evershed flow. They are embedded in a background medium whose magnetic field is more vertical. Besides, the magnetic field strength of the flux tubes is weaker than that of the background.

In order to determine the magnetic and kinematic structure of a sunspot, Bellot Rubio et al. (2004) performed an inversion of the observed Stokes profiles[8] using the SIR code (Stokes Inversion based on Response functions; Ruiz Cobo & del Toro Iniesta, 1992). Using a two-component model, their results backed up the uncombed penumbral model. One of the main results is the alignment between the velocity and the magnetic field vectors. The Evershed flow is predominantly found in the dark cores (Bellot Rubio et al., 2005) and appears in deep photospheric layers (Jurcák et al., 2007). Hence, a very important conclusion of this model is that the Evershed flow is related to the flux tube component, to wit: the Evershed flow is magnetized. Ruiz Cobo & Bellot Rubio (2008) solved the 2D stationary heat transfer equation in a stratified atmosphere considering the uncombed penumbral model. They found that this model produces bright filaments with dark cores, in agreement with the observations. Finally, they demonstrated that the Evershed flow could naturally cause the enhanced penumbral brightness.

Despite these achievements, it is not clear yet how the uncombed penumbral model could explain some observational features, such as the small-scale twisting motions along penumbral filaments discovered in intensity images by Ichimoto et al. (2007a). Furthermore, according to Scharmer & Spruit (2006), an horizontal flattening of the flux tube could appear because the magnetic field strength of the background component is stronger at the top and at the bottom of the tube. However, Borrero (2007) demonstrated that a very small azimuthal component in the magnetic field vector of the tube

[8] $1''$ spatial resolution data from the Tenerife Infrared Polarimeter(Martínez Pillet et al., 1999; Collados et al., 1999a) at the German Vacuum Tower Telescope (Teide Observatory, Spain).

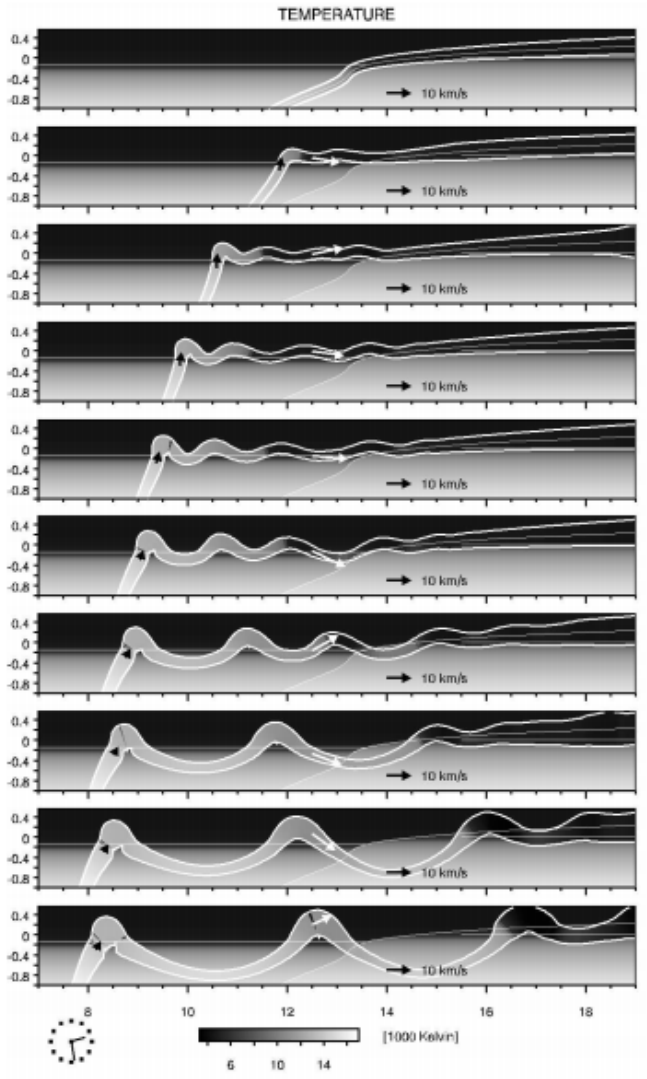

FIGURE 1.5:— Evolution of a thin magnetic flux tube in a sunspot penumbra. Snapshots of the tube (magnified by a factor of 4) are displayed every 1000 s. Temperature is represented by the gray scale. Arrows indicate the flow direction along the tube. The umbra is to the left. From Schlichenmaier (2003).

is enough to prevent such a flattening from occurring.

Alternatively, Sánchez Almeida & Lites (2000) and Sánchez Almeida (2005) proposed a sunspot model based on the assumption that the penumbra is formed by optically thin magnetic strands interlaced along the line of sight, i. e., a MIcroStructured Magnetic Atmosphere (MISMA). Using this model, Sánchez Almeida (2009) suggested that the penumbra is full of tiny magnetic loops. Although the MISMA model is able to reproduce many

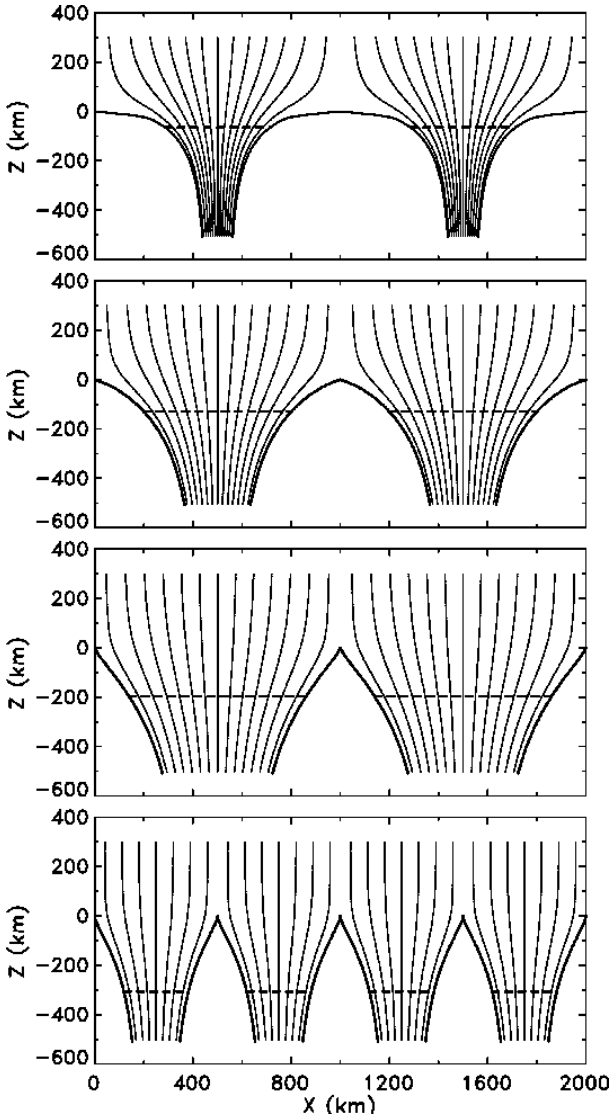

FIGURE 1.6:— Sketch of penumbral filaments in the gappy penumbral model. Shown are gap shapes (thick lines) and field lines in the outer penumbra (top panel), the mid penumbra (second and third panels) and the inner penumbra (bottom). The dashed horizontal line indicates the height where the gas pressure in the magnetic component is equal to that of the field-free component at z = 0 km. From Scharmer & Spruit (2006).

observational features, direct evidence for such loops is still to be found.

1.4.2 The gappy penumbra model

Spruit & Scharmer (2006) and Scharmer & Spruit (2006) suggested an alternative model called the gappy penumbral model. It is based on the idea that the penumbral magnetic field is potential and there are free-field gaps

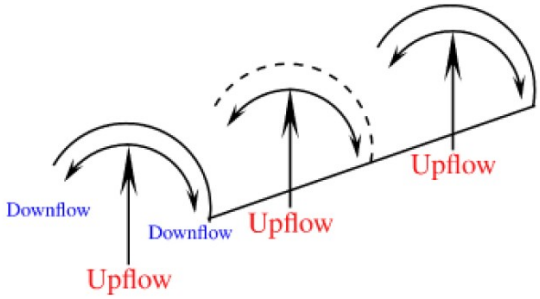

FIGURE 1.7:— Sketch of a penumbral filament and its expected convective motions. From Borrero & Ichimoto (2011).

located just below the penumbral filaments. These gaps open through the sunspot from below, contributing to heat up the penumbra by regular convection. So, the Evershed flow was identified as a free-field flow occurring at the top of each gap. Due to the difference between their magnetic field strengths, the dark core and the two lateral brightenings would not be located at the same height. Moreover, the shape of the gaps varies with radial distance in the penumbra (Figure 1.6). Thus, the magnetic field inclination at the top of the gap in the outer penumbra is larger than in the inner penumbra.

However, there is observational evidence of the magnetic nature of the Evershed flow (see Bellot Rubio, 2010, and references therein). Hence, the gappy penumbral model was revised by Scharmer et al. (2008) to include magnetic fields, with convection being responsible for the gas motion. So, as stated by this model, the Evershed flow is always directed radially outward the sunspot and corresponds to the horizontal flow component of overturning convection ocurring in gaps with strongly reduced magnetic field strength. Thus, upflows appear in the inner parts of the gaps and most of the gas moves outward or sideways, descending back to the solar surface. Therefore, it predicts that upflows and downflows appear azimuthally around the penumbra. This is because Borrero & Ichimoto (2011) refers to the lateral bending of part of the hot upflows on the filaments sides and the returning back to deeper layers as the azimuthal convection (see Figure 1.7). The contribution of the horizontal component would be greater than the azimuthal one. The downward flows at the filament edges will be called *lateral downflows* in this thesis. This velocity field reminds us of that observed in the quiet Sun: from high-resolution observations, it is clear that the bright quiet Sun granules are upward-moving hot material and the dark intergranular lanes are cooler downflows (for more information, see Stix, 2002).

This physical scenario is similar to that proposed by Danielson (1961). He suggested that penumbral filaments represent convective rolls (cells) lying

next to each other, with their axes being parallel to the horizontal component of the magnetic field. Two of these rolls would form a filament as they turn in opposite directions, creating a bright upflow in the center and two downflows on each side.

The main problem with this model is that it is just hypothetical and does not resolve the energy equation. As matter of fact, it is not based on any numerical calculation that: (1) demonstrates the solving of the enhanced brightness of the penumbra and (2) explains the observed Stokes profiles from visible and infrarred spectral lines, and is not observationally corroborated, contrary to the moving magnetic tube or the uncombed penumbral models.

1.5 Penumbral fine structure simulations

Schüssler & Vögler (2006) performed the first realistic magnetohydrodynamical (MHD) simulations of umbral dots and, since then, they have become an effective tool to test physical scenarios in sunspots. Soon after, Heinemann et al. (2007) carried out the first 3D MHD simulations of a sunspot in slab geometry[9] to support the gappy penumbral model. Their results indicated a magnetic field reduction in the penumbral filament center and the existence of overturning convection. Although Heinemann et al. (2007) were able to reproduce some observational features, such as penumbral grain motions, they did not match the observed dimensions and duration of penumbral filaments correctly.

In the same way, Rempel et al. (2009b) made simulations in slab geometry that backed up overturning convection. They showed a positive correlation between brightness and vertical velocity in penumbral filaments, which is a proof of the convective nature of the penumbra. According to these simulations, the penumbral energy transport is asymmetric, producing elongated convective cells in the radial direction. This suggests that the Evershed flow results from the combination of convection and the magnetic field anisotropy. Once again, these simulations were not able to mimic the filaments morphology due to their limited spatial resolution. Kitiashvili et al. (2009) suggested that the flow speed achieved in earlier simulations was not sufficiently high and their simulations pointed to nonlinear magnetoconvection (which has properties of traveling waves in the presence of a strong, highly inclined magnetic field) as the key driver of the Evershed flow. However, observational evidence of nonlinear magnetoconvection has not been found yet.

Advances in numerical methods and computational capabilities have enabled 3D MHD simulations of circular sunspots with enough resolution to investigate morphological details (umbral dots or penumbral filaments),

[9] Only a narrow slice through the center of the sunspot is simulated.

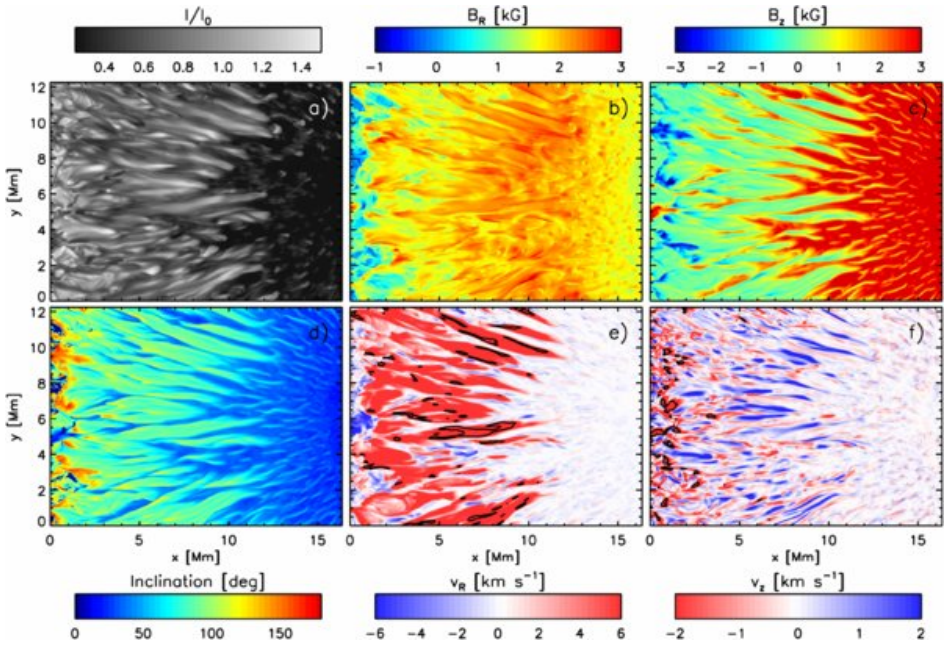

FIGURE 1.8:— Sunspot fine structure at $\tau = 1$. The panels show: a) bolometric intensity, b) radial and c) vertical magnetic field, d) field inclination, e) radial and f) vertical flow velocities. An inclination of 0° corresponds to the same polarity as the umbra, 90° to horizontal and 180° to opposite polarity. Solid contours enclose downflow regions with radial velocities greater than 10 km s^{-1} in panel e and greater than 5 km s^{-1} in panel f. From Rempel (2011b).

such as those by Rempel et al. (2009a), Rempel (2011a,b,c) and Rempel (2012). Figure 1.8 shows details of sunspot fine structure simulated by Rempel (2011b). According to Rempel (2011a), the bulk of energy and mass is transported on scales smaller than the radial extent of the penumbra and stong horizontal outflows are due to a redistribution of kinetic energy that is facilitated mainly by the Lorentz force. This redistribution was analyzed in detail by Rempel (2011b), finding that the Lorentz force causes an energy exchange between motions in the vertical and horizontal directions (see Figure 1.9). Besides, he showed a strong reduction of the vertical magnetic field but an enhancement of the horizontal component within filaments, which means that the Evershed flow is indeed magnetized. Therefore, overturning convection in the presence of strong magnetic fields was supported by these simulations as the mechanism that better reproduces the available Evershed flow observations.

Rempel (2012) performed a in-depth analysis of his simulations. One of the main results concerned the magnetic field in downflowing regions: most of the returning mass flux was not associated with opposite magnetic polarities, indicating that it returns mostly by submerging magnetic fields rather than by flowing along downward directed field lines. Thus, it is expected that more

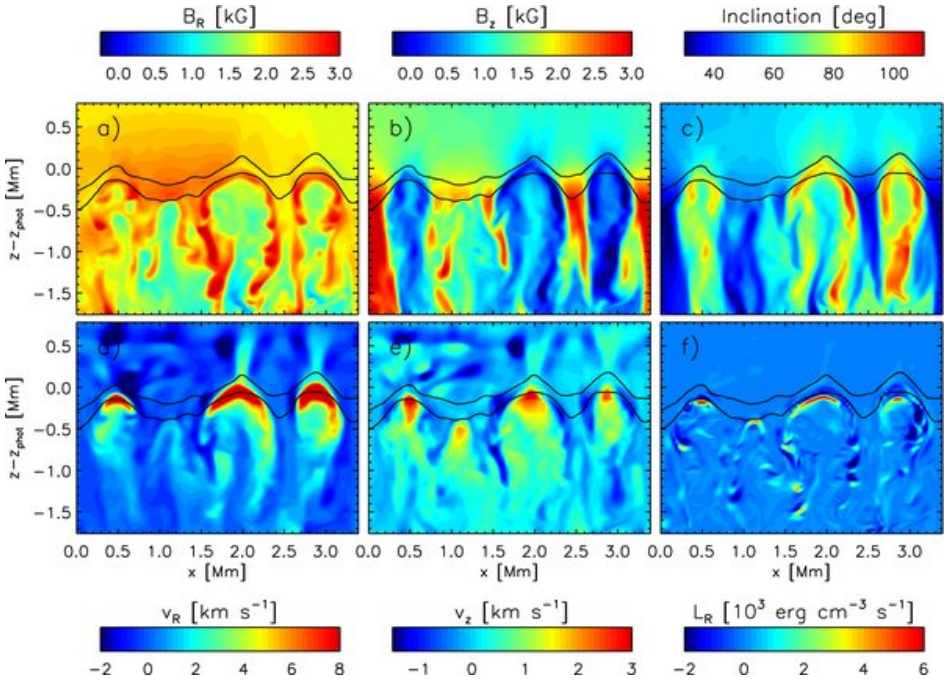

FIGURE 1.9:— Vertical cross section of filaments in the inner penumbra. The quantities shown are: a) radial and b) vertical field strength, c) field inclination, d) radial and e) vertical velocity and f) energy conversion by the horizontal Lorentz force along filaments. Positive values in vertical velocity correspond to upflows, while negative to downflows. Solid lines indicate the $\tau = 1$ and 0.01 levels. From Rempel (2011b).

than half of the returning mass flux in the penumbra is found in regions that have the same polarity as the sunspot umbra.

1.6 Searching for lateral downflows

Although MHD simulations support the existence of overturning convection, there are no unambiguous proofs of this mechanism from observations. While the horizontal component of convection—the Evershed flow—has been studied by many authors (e.g., Bellot Rubio et al., 2004; Borrero et al., 2005; Franz & Schlichenmaier, 2009; Bellot Rubio et al., 2010; Franz, 2011), the azimuthal component has been more elusive. In those studies, no indications of the existence of lateral downflows were found. Therefore, the confirmation of overturning convection needs an unequivocal detection of lateral downflows.

Recently, the independent studies of Scharmer et al. (2011) and Joshi et al. (2011) reported observations of lateral downflows. These authors used high-resolution spectropolarimetric measurements in the C I 5380 Å line acquired with the CRisp Imaging Spectro-Polarimeter (CRISP; Scharmer,

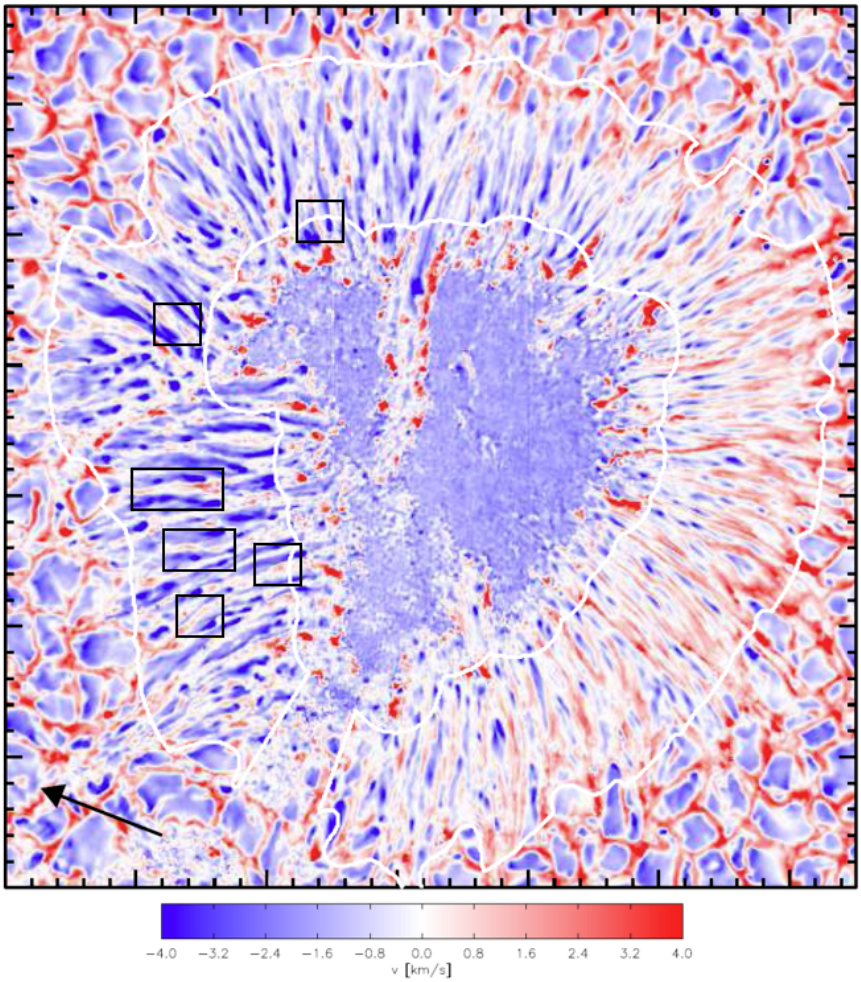

FIGURE 1.10:— Straylight-compensated Dopplergram with stray light ratio of 58 % and a Gaussian PSF of FWHM of 1.″2, obtained from the Supporting Online Material (SOM) of Scharmer et al. (2011). Black rectangles mark examples of lateral downflows. The arrow points to the disk center.

2006) at the Swedish 1-m Solar Telescope (SST; Scharmer et al., 2003a). This line is formed very deep in the photosphere, about 40 km above the continuum forming layer (Stürenburg & Holweger, 1990). Figure 1.10 shows lateral downflows located in between blueshifted channels as reported by Scharmer et al. (2011). In both studies, a single snapshot of a sunspot located relatively far from the disk center was used. Soon after, more papers about lateral downflows were published. Scharmer & Henriques (2012) found indications of lateral downflows in the Fe I 630 nm line pair. Ruiz Cobo & Asensio Ramos (2013) and Scharmer et al. (2013) inferred lanes of reversed polarity fields at the border of penumbral filaments using the SpectroPo-

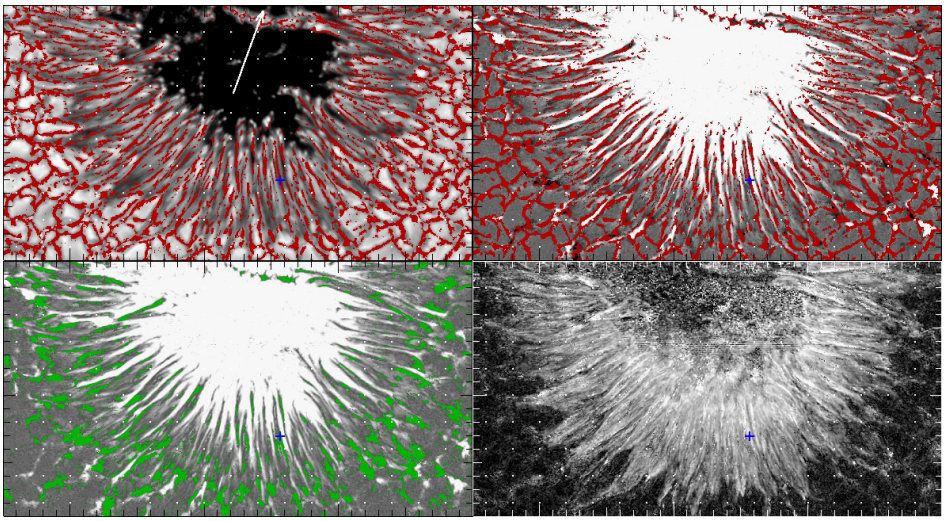

FIGURE 1.11:— Opposite polarity fields in a sunspot penumbra. *Upper row:* Downflow lanes in red overlaid on a temperature map (scaled between 5000 and 6600 K) at $\tau_c = 1$ *(left)* and on the LOS magnetic field map (saturated between -1.0 and 1.4 kG) at $\tau_c = 1$ *(right). Lower row:* Opposite polarity fields less than -200 G in green overplotted on the LOS magnetic field map *left* and the magnitude of the horizontal field (in the local frame) scaled from 150 G to 1800 G.

larimeter (SP; Lites, 2001) of the Solar Optical Telescope (SOT; Tsuneta et al., 2008) aboard the Hinode (Kosugi et al., 2007) and SST/CRISP data, respectively. Figure 1.11 displays the findings of Scharmer et al. (2013), where patches of opposite polarity are cospatial with narrow downflow lanes in the inner part of the penumbra. Finally, Tiwari et al. (2013) determined the physical properties of a *standard* penumbral filament using Hinode/SP data. Table 1.1 summarizes some important aspects of the cited publications.

In all of these studies, the data were subject to non-standard treatments (fourth row in Table 1.1). Scharmer et al. (2011), Joshi et al. (2011), Scharmer & Henriques (2012) and Scharmer et al. (2013) deconvolved their data to compensate for stray light[10] that was hiding the weak signals expected from the lateral downflows. According to Scharmer et al. (2011), a full characterization of stray light in ground-based solar observations is not possible because there are no robust methods to infer it, and thus this treatment was used as an approximate way to correct for stray light contamination. On the one hand, in Scharmer et al. (2011), Scharmer & Henriques (2012) and Scharmer et al. (2013), the deconvolution parameters were estimated using a comparison between observed and synthetic line profiles computed from a 3D hydrodynamical granulation simulation that does not include magnetic fields (Stein & Nordlund, 1998). On the other hand, Joshi et al. (2011) assumed that most of the stray light comes from the vicinity of the pixel under

[10]This stray light comes up from turbulences in the Earth's atmosphere.

TABLE 1.1:— Summary of previous publications about lateral downflows findings

Reference	**Instrument**	**Spectral line**	**Heliocentric angle**	**Data extra-treatment**	**Lateral downflow LOS velocity**
Scharmer et al. (2011)	SST/CRISP	C I 5380 Å	15°	Deconvolution of the observed Stokes profiles with a Gaussian PSF of FWHM of 1.″2 and stray light ratio of 58 %	1 km s^{-1}
Joshi et al. (2011)	SST/CRISP	C I 5380 Å	32°	Deconvolution of the observed intensity profiles with a slightly modification of a Wiener filter	2 km s^{-1}
Scharmer & Henriques (2012)	SST/CRISP	Fe I 6301.5 Å	15°	As Scharmer et al. (2011), using a FWHM of 1.″2 and stray light ratio of 50 %	1 km s^{-1}
Ruiz Cobo & Asensio Ramos (2013)	Hinode/SP	Fe I 6301.5 Å & 6302.5 Å	12.8°	Deconvolution of the Stokes parameters with the Hinode PSF	3 km s^{-1}
Scharmer et al. (2013)	SST/CRISP	Fe I 6301.5 Å	15°	As Scharmer et al. (2011), using a FWHM of 1.″8 and stray light ratio of 40 %	1.3 km s^{-1}
Tiwari et al. (2013)	Hinode/SP	Fe I 6302.5 Å	6°	Convolution of synthetic Stokes profiles with the Hinode PSF at the spatially coupled inversions (van Noort 2012)	0.5 km s^{-1}

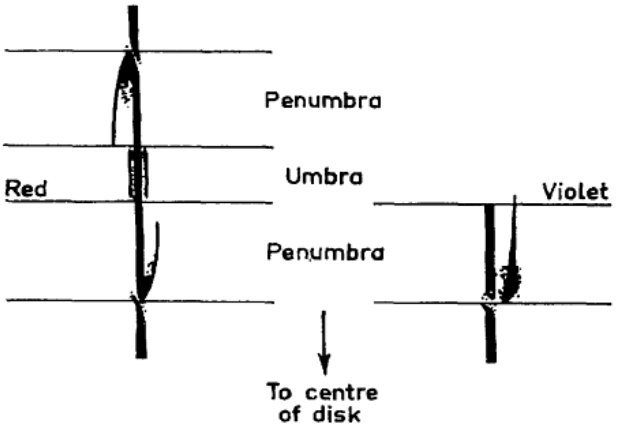

FIGURE 1.12:— Drawing of line flags in sunspot spectral line as reported by Bumba (1960).

consideration. According to Löfdahl & Scharmer (2012), the origin of the stray light in SST data is still unknown and, therefore, the use of uncertain deconvolution parameters raises doubts on the reliability of the results. In the case of Ruiz Cobo & Asensio Ramos (2013), the Stokes profiles were deconvolved using the PSF of the Hinode SOT, which is known. By contrast, Tiwari et al. (2013) used a spatially coupled inversion (van Noort, 2012) and convolved their synthetic Stokes profiles with the Hinode PSF.

It is not possible to directly measure the three components of the velocity field vector. Instead of the velocity vector, we observe the LOS velocity that is the projection of the velocity vector to the LOS. Measuring the vertical velocity is only possible if observations are acquired at the disk center, i. e., at an heliocentric angle of 0°. So, the larger the heliocentric angle, the larger the projection of the velocity is. In consequence, the Evershed effect is more efficient hiding the weak signals expected for lateral downflows. Therefore, in order to identify lateral downflows as redshifts in Dopplergrams, a sunspot at or close to the disk center must to be observed. In view of Table 1.1, all the sunspots studied so far were located relatively far from the disk center, except that of Tiwari et al. (2013).

1.7 Supersonic Evershed downflows

Observations at high spectral resolution show all types of spectral line asymmetries in sunspot penumbrae. Bumba (1960) noticed the existence of *line flags*[11], an extreme case of asymmetry. As seen in Figure 1.12, near the outer spot boundary but still within the penumbra, a satellite line shifted

[11]Nomenclature depends on the author. They are also called line flares (Holmes, 1961), kink lines (Maltby, 1964) or, most commonly, satellite lines.

in opposite direction appears on the two sides of the spot with velocities greater than 6 km s^{-1}. Bumba (1960) suggested that line flags are a result of Doppler shifts, but the line is not shifted as a whole. According to Holmes (1961), this phenomenon was previously observed by Evershed (1909), but it was related to the Zeeman splitting rather than to a Doppler effect where matter moves away from the umbra. Maltby (1964) considered flag lines to be characteristic for the Evershed effect. Actually, in the 1960s, it was accepted that the line shift induced by the Evershed effect is accompanied by an asymmetry where the line wings are more strongly displaced than the line core. It is important to mention that if the satellite is not resolved, then the line just appears asymmetric.

Line flags were interpreted as a shifted satellite line superposed on an almost unshifted main component, which originate from unresolved fine structures (Stellmacher & Wiehr, 1971). In the same way, Wiehr (1995) suggested that the main component corresponds to bright penumbral structures while the satellite line comes from dark structures with velocities greater than 5 km s^{-1}.

Later, Bellot Rubio et al. (2004) found that the velocity and magnetic field vectors are aligned and go downward in the outer penumbra (see Section 1.4.1). Besides that, they showed that the average LOS velocity close to the outer penumbral border is greater than 6 km s^{-1}, i.e., almost supersonic. In a similar way, Westendorp Plaza et al. (1997) related downward mass motions to opposite polarity fields in the outer penumbral border using data from the Advanced Solar Polarimeter (ASP; Elmore et al., 1992). They obtained LOS velocities of order 3 km s^{-1}, which are far from being supersonic.

Supersonic downflows are not only present near the outer penumbral boundary. They are found also in the inner penumbra (del Toro Iniesta et al., 2001). According to these authors, Evershed downflows are mostly concentrated in very cold magnetic tubes and can be found also in the middle penumbra. Besides, they obtained downflows of order 16 km s^{-1}. As a matter of fact, del Toro Iniesta et al. (2001) confirmed the existence of supersonic flows along the downstreaming legs of magnetic channels as predicted by the siphon flow model. However, there were no clues of the upstreaming arch footpoint.

Ichimoto et al. (2007b) detected the presence of supersonic downflows in the mid and outer penumbra using a set of magnetograms in the far wing[12] of the Fe I 6302Å line. In the Stokes V map corresponding to the blue wing (at -277 mÅ), there are structures with the same polarity as the sunspot that are associated with upflows. In the red wing (at 277 mÅ), a number of patches are distributed preferentially in the mid-outer penumbra. They

[12]These are circular polarization maps at ± 277 mÅ, corresponding to a LOS velocity of 13 km s^{-1}.

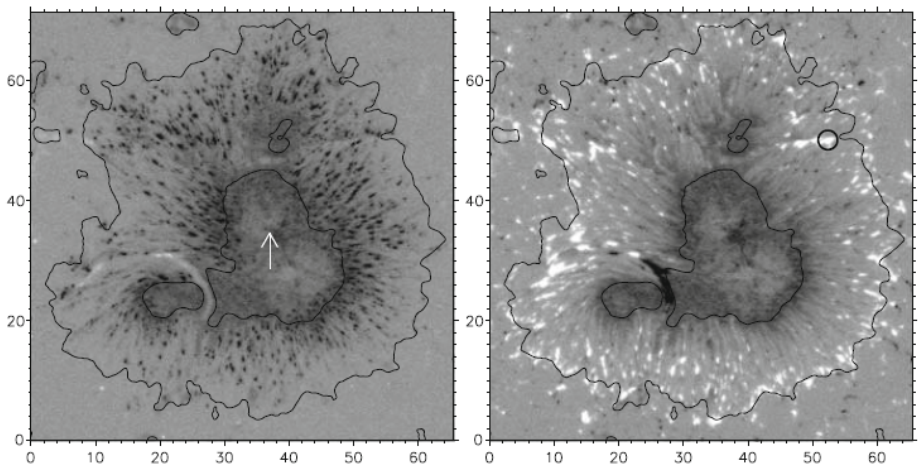

FIGURE 1.13:— Magnetograms at ± 277 mÅ from the center of the Fe I 630.25 nm line (right and left panels, respectively). The circle overplotted in the right panel marks the downflowing patch shown in Figure 1.14. Distances are expressed in arcsec. The arrow points to the disk center. From Bellot Rubio et al. (2010).

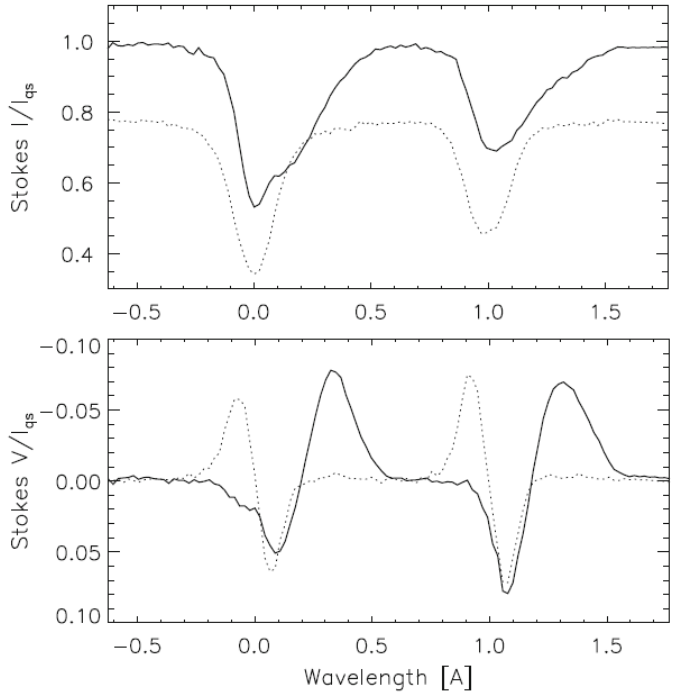

FIGURE 1.14:— Stokes I and V profiles of the downflowing patch enclosed within a circle in the right panel of Figure 1.14 (solid lines). The dotted lines represent typical signals in the outer penumbra, with the polarity of the spot and very small flows. From Bellot Rubio et al. (2010).

have a polarity opposite to that of the sunspot and are related to strong downflows. These structures are believed to be the sources and the sinks of the Evershed flow. The differences of the V-signal in each wing are illustrated in Figure 1.13. Some of these structures are supersonic. Figure 1.14 shows the Stokes I and V profiles of the downflowing patch marked with a circle in the right panel of Figure 1.13. At that position, the Stokes profiles reveal the presence of opposite polarity fields with a LOS velocity of about 9 km s^{-1}, i. e., supersonic. Apart from this, Franz & Schlichenmaier (2009) found that returning Evershed flows also exhibit 3-lobed Stokes V profiles. However, this does not mean that all 3-lobed Stokes V profiles harbor supersonic downflows.

The fine structure of the Evershed downflows has been investigated by van Noort et al. (2013). They described the dynamics of these downflows using a spatially coupled inversion technique. They inferred LOS velocities of order 20 km s^{-1} and magnetic strengths of 7 kG, which are the greatest values ever obtained in the penumbra and therefore controversial.

1.8 Motivation of this work

The penumbra is a strongly magnetized medium and, therefore, convection is expected to be inhibited if not completely suppressed (Biermann, 1941; Cowling, 1953). However, it is observed to harbor a plethora of mass motions. Since the discovery of the Evershed effect, numerous authors have proposed mechanisms to explain the velocity field of the penumbra (e.g. Meyer & Schmidt, 1968; Solanki & Montavon, 1993; Montesinos & Thomas, 1997; Schlichenmaier, 2002a; Bellot Rubio et al., 2004; Scharmer & Spruit, 2006), but none of them accounts for all observational facts. Therefore, we still have to explain the various penumbral flows and their relation with the magnetic field, i. e., understand how the gas moves in the presence of strong magnetic fields. 3D MHD simulations (Heinemann et al., 2007; Rempel et al., 2009a,b; Rempel, 2011a,b, 2012) support magnetoconvection as the mechanism behind mass motions, but we do not have unambiguous observational proofs of it yet.

The main goal of this thesis is to shed light on how mass is transported in the penumbra. Specifically, we want to study the least known aspects of the velocity field in the penumbra, paying special attention to the smallest spatial scales and the temporal evolution of the flows.

For this purpose, we use temporal sequences of high cadence, spatial resolution spectropolarimetric data. These are, essentially, the four factors needed to perform the analysis contained in this thesis:

- High-spatial resolution. Some penumbral structures have already been observed and studied, such as supersonic Evershed downflows (e.g. Westendorp Plaza et al., 1997; del Toro Iniesta et al., 2001; van Noort

et al., 2013), but with a spatial resolution poorer than $\sim 0\farcs3$. For these structures, we firstly resolve them spatially and corroborate undoubtedly their existence. In addition, there are other structures whose presence is in question. Evidence of lateral downflows has been obtained by some authors (e.g. Scharmer et al., 2011; Joshi et al., 2011; Ruiz Cobo & Asensio Ramos, 2013), but not by others (Rimmele & Marino, 2006; Franz & Schlichenmaier, 2009; Bellot Rubio et al., 2010; Franz, 2011). Thus, higher spatial resolution observations are needed to confirm or refute their existence.

- High cadence. The penumbra is not a static region and many phenomena develop rapidly on time scales of minutes. Therefore, high cadence observations are needed to analyze them in detail.

- Time series. Thanks to time sequences, it is possible to observe the evolution of structures during their lifetimes. This kind of study hold the key to understand mass motions in penumbrae. Furthermore, stable sequences allow us to correct for subsonic oscillations, whose effect are undesirable when studying velocity fields (specifically, in the case of weak signals).

- Spectropolarimetric data. Spectropolarimetry is needed to obtain physical information in each pixel. Thanks to it, we are able to infer different atmospheric parameters, such as LOS velocity, magnetic field strength, inclination or azimuth using Stokes profiles inversion techniques and to propose a physical scenario to explain the observations.

Besides clarifying aspects about small-scale flows in sunspots, the results of this thesis can be used in penumbral heating studies and validation of 3D MHD simulations (e.g. Heinemann et al., 2007; Rempel, 2011b, 2012). Furthermore, the implications of this thesis are not exclusively related to the Sun, since they can be extended to other stars. New generation telescopes have been used to search for signals of magnetic fields in other stars and even map out starspots on their surfaces. This information reveals how and why some stars are magnetic and what the implications might be for life in exoplanets (Zodet, 2015). Additionally, the penumbra is an exceptional laboratory to study convection in the presence of magnetic fields. As such, it may help understand processes related to convection in other research areas.

1.9 Overview of the thesis

This Section is a brief outline of the contents that will be elaborating in the following. This thesis is structured in six Chapters. The second Chapter describes the observations and the data reduction. It explains why has been

so important the observation at the Swedish Solar Telescope to secure appropiate data for this study. Chapters three, four and five constitute the body of this thesis, where we study two observational phenomena: lateral downflows in penumbral filaments and supersonic Evershed downflows. They provide us with information about different components of the penumbral velocity field. Chapter six relates all the results obtained in previous Chapters to give an unique framework and formulates questions about future work in view of the main conclusions of the thesis. Specifically:

- The data used on this thesis was acquired with the CRISP instrument at the 1-m Swedish Solar Telescope. This ground-based telescope provides us with high resolution spectropolarimetric data. However, its peculiarities make the data reduction tasks hard, and some specific procedures are necessary to reduce the observation. Chapter 2 answers the questions: What were our data requirements and how are they accomplished by the Swedish 1-m Solar Telescope?

- In Chapter 3, we focus on small-scale magnetoconvection at sunspot penumbrae. This is an issue that has consistently eluded detection. Apart from the Evershed flow, our Dopplergrams show weak and redshifted patches in between the filaments. We demonstrate that these patches are due to the existence of lateral downflows, i. e., the weak downward component of the lateral returning flow. Their temporal behavior, as well as some physical properties, are described and used to identify the factors that may conspire to hide the small-scale magnetoconvection. Finally, there is a comparison of the results with compatible theoretical scenarios, as well as with those obtained from recent simulations. Part of this work was published in The Astrophysical Journal (Esteban Pozuelo et al., 2015).

- Since the early sixties, it is known that there are supersonic flows in the penumbra. Some time after, they were related to the Evershed flow sinks. However, all the studies were based on a single snapshot and higher resolution was called for. Nowadays, thanks to higher spatial resolution observations, we can properly characterize the physical properties and the temporal evolution of the supersonic Evershed downflows that appear all over the penumbra. The fact of seeing closely the penumbra inspires curiosity to ask ourselves if the supersonic Evershed downflows might be related to other structures, such as the Evershed clouds. We also present a comparison between our results and those found in the literature.

- Finally, Chapter 6 summarizes the results obtained in this thesis. As mentioned before, these observational phenomena are different parts

of the same aspect: the velocity field of the penumbra. Therefore, establishing a common framework between them, the conclusion will shed some light on how matter moves in the penumbra at photospheric levels.

2

Observations and data reduction

My fascination with letting images repeat and repeat
–or in film's case 'run on'– manifests my belief that
we spend much of our lives seeing without observing
Andy Warhol

This chapter describes the main steps of the data adquisition and reduction that make the Swedish Solar Telescope observations unique. We needed data with the best possible spatial resolution and temporal cadence. For this purpose, we selected the Swedish Solar Telescope to perform our observations.

The contents is organized as follows. Section 2.2 describes the main aspects of the Swedish 1 m Solar Telescope and Section 2.3 details the CRISP instrument. The data acquisition is discussed in Section 2.4 and the reduction explained in Section 2.5. Each subsection contains some fundamental steps of the data reduction process, namely, flat-field correction (2.5.1), image alignment (2.5.2), image restoration (2.5.3), prefilter correction (2.5.4), and polarimetric calibration (2.5.5).

2.1 What kind of data do we need?

An in-depth study of the velocity field of sunspot penumbrae requires data that satisfy stringent requirements. As mentioned in Section 1.8, previous analyses can give us hints on how to achieve our main goal.

First of all, we need bidimensional spectropolarimetric data. Although the LOS velocity can be obtained just from intensity line profiles, Stokes Q, U and V signals are needed to infer other physical parameters -such as the three components of the magnetic field vector- that will be very useful to understand the penumbra.

Some of the latest penumbral studies (e.g., Franz & Schlichenmaier, 2009; Bellot Rubio et al., 2010; **?**; Ruiz Cobo & Asensio Ramos, 2013; Franz & Schlichenmaier, 2013) pointed out the need of achieving high spatial resolution. This is crucial to analyze the fine structure of the penumbra in detail. IA spatial resolution close to $0\farcs1$ (or even better) is needed to observe smaller structures on sunspot penumbrae.

Furthermore, the computation of the LOS velocity should be accurate to 100 m s^{-1}, i. e., to a Doppler velocity of 2 mÅ, particularly for the detection of small-scale convection (see Chapter 4) since it is expected to produce very weak signals. This last requirement can only be satisfied with careful data reduction, which in turn calls for a complete understanding of the instrument.

Last, but not least, there is a necessity to know how the penumbra evolves with an adequate temporal cadence. The cadence strongly depends on the instrumental elements and the number of wavelength positions used to sample the spectral line.

For these reasons, observations were perfomed at the Swedish 1-m Solar Telescope where all these requirements are satisfied. It provides high-resolution spectropolarimetric data whose reduction is performed in a meticulous way, as it is explained in the following Sections.

2.2 The Swedish 1-m Solar Telescope

The Swedish 1-m Solar Telescope (SST; Scharmer et al., 2003a) is a vacuum refractor telescope sited on the Roque de los Muchachos Observatory (La Palma, Spain). It is managed by the Institute of Solar Physics of Stockholm University. The main aim of its design is to analyze the magnetic fields and the dynamics of the solar atmosphere with high accuracy. To that end, it is capable of delivering diffraction-limited images, i.e., it reaches the theoretical resolution for a telescope of its size, which is $0\farcs1$ (75 km on the solar surface) at 630 nm.

The primary optics system is located on top of the turret (Figure 2.1). It consists of a fused silica lens and two plane Zerodur alt-azimuthal mirrors. The reason why the SST uses a single lens is because it allows for excellent image quality, enabling narrow-band imaging and polarimetry with a minimum of optical surfaces. The lens has a diameter of 1.098 m, an aperture of 0.97 m and a focal length of 20.3 m at a wavelength of 460 mm. It also acts as vacuum window, being the spherical aberration from the vacuum load negligible. Until the inauguration of the NST solar telescope located at the Big Bear Solar Observatory (USA) in 2009, the SST was the largest solar telescope in operation.

If a single lens without any filter were used for simultenous observations over a broad wavelength range, the resulting image would have poor quality

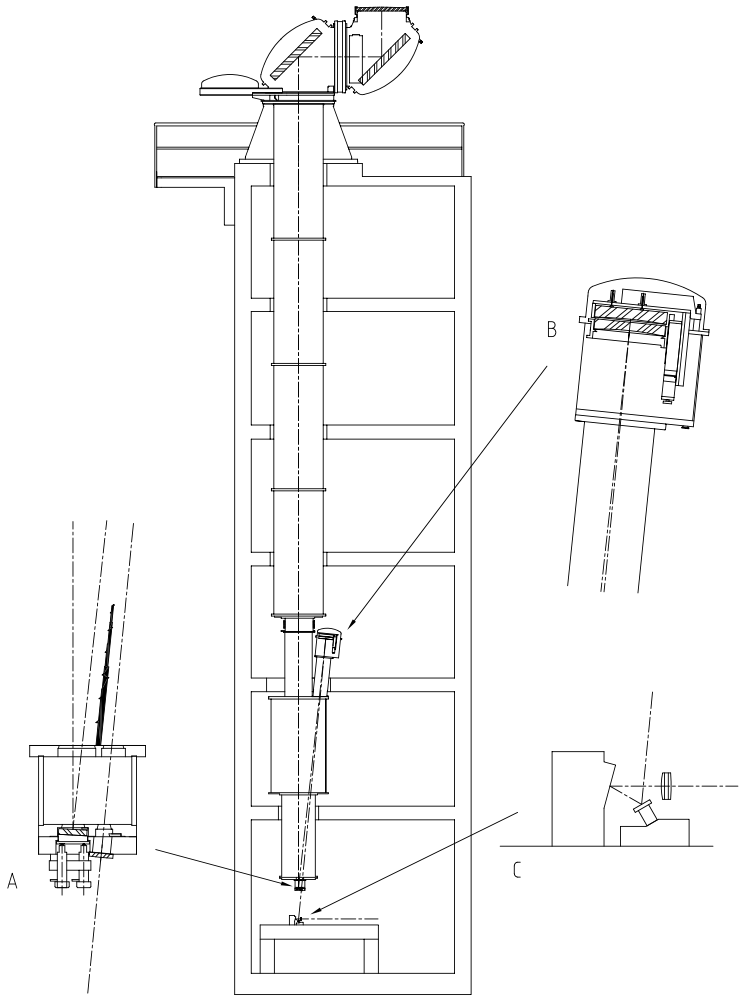

FIGURE 2.1:— Sketch of the SST showing the 1-m lens, the two alt-azimuthal mirrors, the field mirror (A), the Schupmann corrector (B) and the exit window (C). From Scharmer et al. (2003a).

because each wavelength has different focal lengths. To alleviate this situation, a Schupmann corrector is used. After the Schupmann corrector, the light beam reaches the tip-tilt mirror (TM in Figure 2.2) that corrects image motions measured by the correlation tracker (CT in Figure 2.2). Thus, the resulting image will be steady.

2.2.1 The adaptive optics system

An efficient adaptive optics system (AO; Scharmer et al., 2003b) is needed to ensure nearly diffraction-limited spectropolarimetric data. Otherwise,

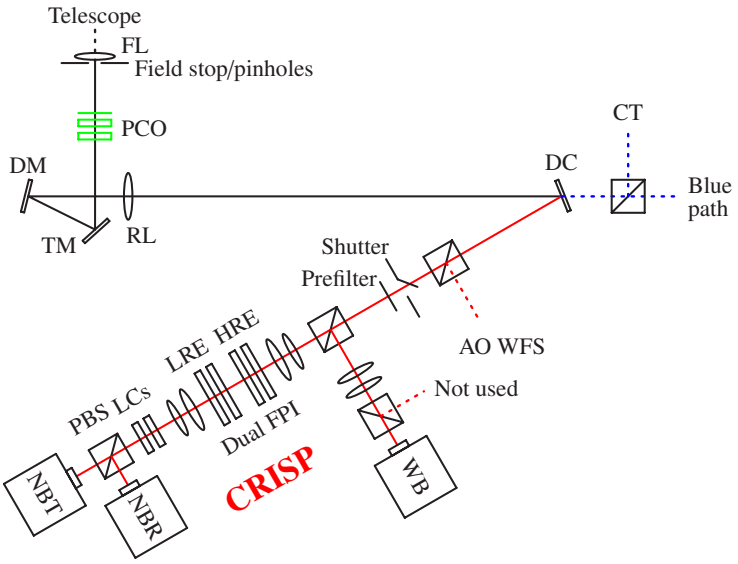

FIGURE 2.2:— Sketch of the optics from the exit window of the telescope to the CRISP instrument. FL = field lens, TM = tip-tilt mirror, DM = deformable mirror, RL = re-imaging lens, DC = dichroic beamsplitter, AO WFS = adaptive optics wavefront sensor, CT = correlation tracker, WB = wideband camera, FPI = Fabry-Pérot Interferometer, HRE = high resolution etalon, LRE = low resolution etalon, NBT = narrowband transmitted camera, NBR = narrowband reflected camera, LCs = liquid crystal variable retarders. From de la Cruz Rodríguez et al. (2015).

the diffraction limit would be reached only during a small portion of the observing time due to seeing perturbations. The AO removes in real time the perturbations generated along the optical path between the target and the telescope. The elements of the AO are a wavefront sensor and a deformable mirror (AO WFS and DM, respectively in Figure 2.2).

The wavefront sensor is of Shack-Hartmann type and consists of (recently installed) 85 microlens and a light detector. It is located in the red beam before a beamsplitter where a small part of the light is sent to it and the rest continues until the CRISP spectropolarimeter. This sensor measures the phase of the wavefront at the pupil using the 36 first terms of Zernike, which are able to fit turbulence induced seeing. On the other hand, deformable mirrors are designed to flattening the phase of the wavefront by deforming their shape. At this moment, the newest deformable mirror installed on the SST has 85 electrodes monomorph mirrors.

After the deformable mirror, there is a re-imaging lens that changes the image scale without altering the corrections applied by the tip-tilt and AO mirrors. Then, the light passes through a beamsplitter where part of it is transmitted to the blue arm of the optical system and the rest is reflected

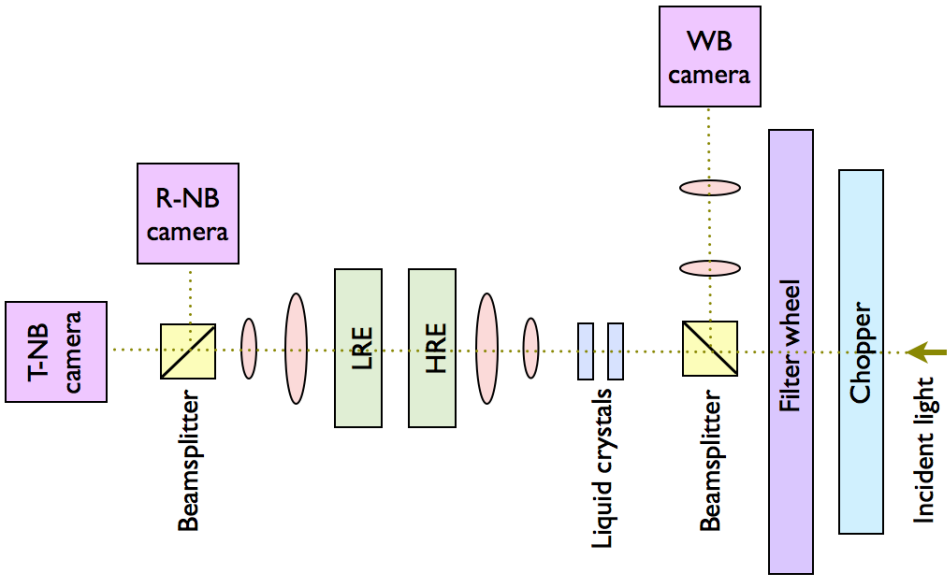

FIGURE 2.3:— Sketch of the 2011 campaign configuration of the CRISP instrument. The current configuration is shown in Figure 2.2.

to the red arm.

2.3 The CRISP Spectropolarimeter

In the red arm of the optical system, there is a dual Fabry-Pérot filtergraph called CRisp Imaging SpectroPolarimeter (CRISP; **?**). It allows for very high cadence and high spatial resolution spectropolarimetric observations and operates in the spectral range between 510 and 860 nm. Its optical system mainly consists of an optical chopper, a filter wheel, two liquid crystal variable retarders (LCs), two etalons, beamsplitter and three cameras, as can be seen in Figure 2.3.

The light passes through an optical chopper that synchronizes the three cameras. It has a rate of 36 Hz allowing an exposure time of 17 ms. After that, there is a filter wheel that isolates the desired wavelength region. At such a position, the light beam is not telecentric and some variations in the central wavelength over the FOV can appear (de la Cruz Rodríguez, , private communication). Next, the light beam is split by a beamsplitter. Ten percent of the light is reflected and recorded by the wideband (WB) camera. The other 90 % is transmitted to the LCs.

CRISP is a dual-beam spectropolarimeter. Thus, it consists of a filtergraph and a polarimeter. The transmitted wavelength positions are set by the Fabry-Pérot etalons. An etalon consists of a cavity with two reflecting plates where the light is reflected several times. These reflections produce a multiple interference pattern. The transmission profile of an etalon, T, is given by

$$T = \frac{1}{1 + \frac{4R}{(1-R)^2} sin^2\left(\frac{\psi}{2}\right)}, \tag{2.1}$$

where R is the reflectivity of the etalon and ψ is the phase difference between successive light reflections. As explained by Kentischer et al. (1998), Fabry-Pérot interferometers produce quasimonochromatic images when a high resolution etalon (HRE) is combined with a low resolution etalon (LRE). The purpose of the HRE is to define the observed wavelength, from the range limited by the prefilter, while the LRE suppresses secondary transmission peaks. Therefore, the transmission profile of CRISP is given by the product of the transmission profiles (Equation 2.1) of the HRE and the LRE. In the case of CRISP, the etalons are mounted in telecentric configuration[1]. Such a scheme optimizes the image quality in the focal plane (Kentischer et al., 1998; **?**). However, this configuration produces pixel-to-pixel variations in the transmission profile of the instrument:

- The surface of the etalons is not completely flat. In fact, when the light is reflected between the plates of the etalon, there are imperfections (called cavity errors) that introduce phase shifts. Therefore, the position of the central wavelength of the transmission profile is not the same for all the pixels. This means that monochromatic images show intensity fluctuations which are artificial, i.e., produced by the cavity errors.

- There are reflectivity variations in the coating of the etalons. This produces differences in the width of the transmission profile across the field of view (FOV).

These effects are corrected during the data reduction to obtain accurate datasets (see Section 2.5).

On the other hand, the polarimeter consists of two LC variable retarders and a linear polarizer (or polarizing beamsplitter). The light is modulated by the two LCs. A retarder is an optical device that resolves a light wave into two orthogonal linear polarization components and produces a phase

[1]The etalons are located close to the focal plane and the telescope pupil is collimated.

shift between them. The LCs create four linear independent combinations of the incoming Stokes parameters[2], so that,

$$\begin{pmatrix} I_1 \\ I_2 \\ I_3 \\ I_4 \end{pmatrix} = \begin{pmatrix} M_{11}\, M_{12}\, M_{13}\, M_{14} \\ M_{21}\, M_{22}\, M_{23}\, M_{24} \\ M_{31}\, M_{32}\, M_{33}\, M_{34} \\ M_{41}\, M_{42}\, M_{43}\, M_{44} \end{pmatrix} \begin{pmatrix} I_{in} \\ Q_{in} \\ U_{in} \\ V_{in} \end{pmatrix} , \tag{2.2}$$

where the conversion coefficients are the elements of the modulation matrix M, $(I_{in}\, Q_{in}\, U_{in}\, V_{in})$ are the Stokes parameters of the incoming light beam and $(I_1\, I_2\, I_3\, I_4)$ are the resulting intensities. LCs are fast enough to change their state during the CCD readout, i.e., which lasts less than 10 ms. Finally, the resulting light is divided by a polarizing beamsplitter in two beams with orthogonal polarization states. They are recorded by two NB cameras -transmitted and reflected, respectively. Later, these two orthogonal polarization states will be combined to remove seeing-induced polarization to first order (Lites, 1987; Casini et al., 2012).

2.4 Data adquisition

The observations used for this thesis were acquired on 28 September 2011 between 09:18:00 and 10:03:52 UT. Figure 2.4 shows the main sunspot of active region AR 11302 that we followed under excellent seeing conditions. Some observational parameters are summarized in Table 2.1.

TABLE 2.1:— Observational parameters of our dataset

Parameters	**Values**
Date	2011.09.28
Target	NOAA AR 11302
Heliocentric angle	6.8°
Starting time	09:18:00 UT
Total duration	43 min 12 s
Cadence	32 s
Exposure time	17 ms
Pixel size	0.059 ″/pixel
Field of view	55″ x 55″
Spectral line	Fe I 6173 Å
SNR[3]	1000

[2]At least four different modulation states are needed to infer the four Stokes vector.

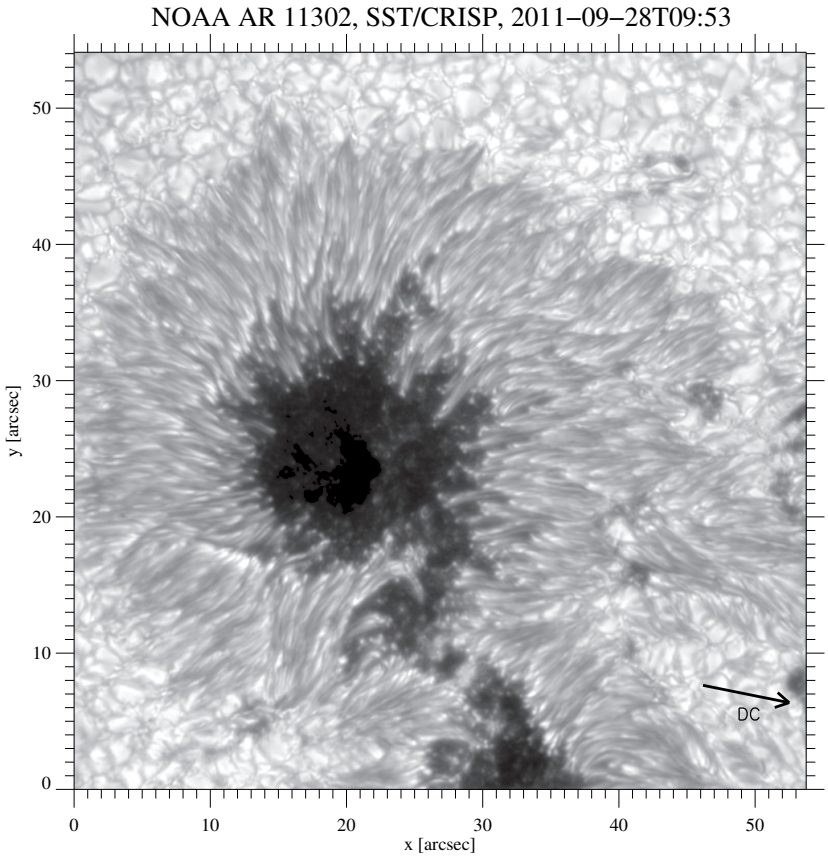

FIGURE 2.4:— Continuum intensity image of the main sunspot of AR 11302 as observed through the narrow-band channel of CRISP at an heliocentric angle of 6.8° on 28 September 2011, 09:53 UT. The arrow points to the disk center.

The data consist of time sequences of full Stokes measurements in the photospheric Fe I 617.3 nm line. CRISP allows us to accurately measure the four Stokes parameters (I, Q, U, V) in each pixel to obtain physical information about the atmosphere.

The diffraction limit of the SST at 617 nm is $\lambda / D = 0\farcs13$, i. e., approximately 90 km on the solar surface. We selected the Fe I 617.3 nm spectral line because it is a narrow photospheric transition suitable for Doppler shift measurements, has a clean continuum and do not show conspicuous line blends or telluric lines nearby. According to the atomic and spectral parameters given in Norton et al. (2006), the Fe I 617.3 nm line has an effective Landé factor of 2.5 and an excitation potential of 2.22 eV. The disk center quiet Sun profile from the Fourier Transform Spectrometer atlas (FTS; Brault & Neckel, 1987) has a depth of 0.66 and a FWHM of 0.102 Å. They also quoted 302 and 16 km for the formation height of the core and the continuum, respectively, supposing the VAL-C atmosphere under non-LTE

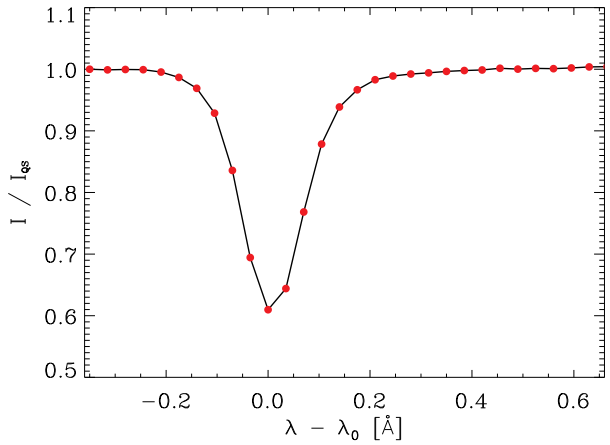

FIGURE 2.5:— Mean quiet Sun intensity profile of the Fe 1 617.3 nm line in the scan taken at 09:34:00 UT. The spectral samples are shown with red circles. The x-axis represents the wavelength scale calibrated using the umbra as a reference.

assumption.

Figure 2.5 shows the spectral sampling of the line. It consists of 30 wavelength positions, from -35.0 to +66.5 pm in steps of 3.5 pm. Each spectral scan was completed in 32 s. We performed 9 acquisitions per modulation state, obtaining 36 images per wavelength position. The exposure time was set by the optical chopper, i.e., 17 ms. The field of view of each scan is approximately 55″x 55″ with a plate scale of 0.″059 per pixel.

2.5 Data reduction

Due to the peculiarities of CRISP, it is necessary to perform some specific steps to reduce the spectropolarimetric data. The following list outlines the typical reduction process (depicted in Figure 2.6):

1. Sum of dark, flat, polarization calibration and pinhole images.

2. Using the summed polarization calibration images, the demodulation matrices of the two beams are obtained. The polarization calibration is carried out as described by van Noort & Rouppe van der Voort (2008) and will be explained in more detail in Section 2.5.5.

3. After summing the flat images, the resulting flats are demodulated using the Mueller matrices calculated in the previous step.

4. Estimation of the cavity and the reflectivity errors. This step is performed fitting the demodulated flats to an estimated quiet Sun profile.

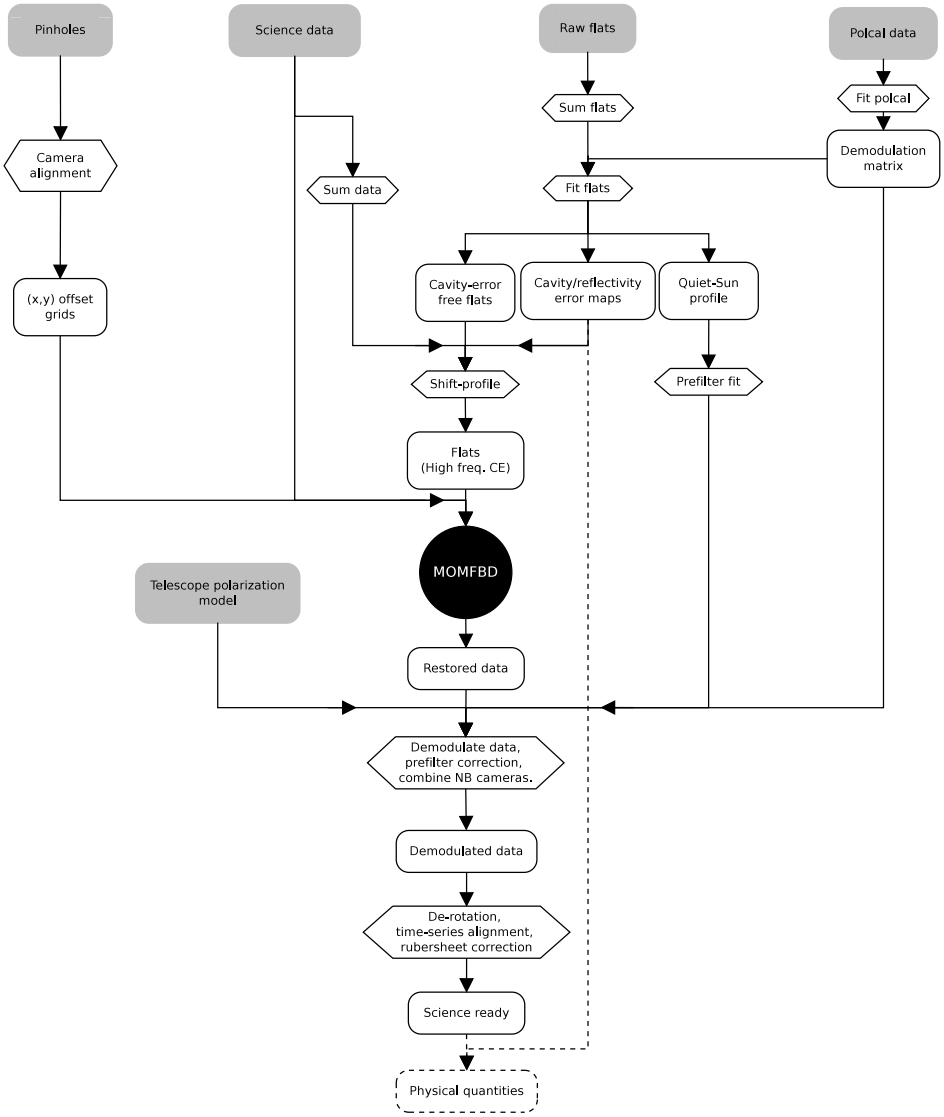

FIGURE 2.6:— Sketch of the CRISPRED pipeline (de la Cruz Rodríguez et al., 2015).

The result are cavity-error-free flat images, where there are no intensity fluctuations due to CRISP imperfections. Further information is given in Section 2.5.1.

5. Using the raw science data, the intensity fluctuations introduced by cavity errors are calculated. Thus, the flats that MOMFBD will use. After that, the cavity errors map is decomposed in low and high frequency components. This step is also explained in Section 2.5.1.

6. Alignment of the pinhole images obtained for each camera (see Sec-

tion 2.5.2). This is an essential procedure to tell the restoration code in a very accurate way how the cameras were shifted from each other. First, it is necessary to align the summed pinhole images of each camera making them coincide to the common FOV and to calculate the shift parameters. Then, this alignment is improved to subpixel precision.

7. Image restoration. We have used the Multi-Object Multi-Frame Blind Deconvolution technique (MOMFBD; van der Noort et al., 2005) as explained in Section 2.5.3.

8. Image restoration does not perfectly compensate for seeing. As a consequence, there are small residual seeing-distortions within a spectral scan. The correction is performed following the strategy of Henriques (2012), which is described in Section 2.5.3.

9. Estimation of the spectral transmission profile of the prefilter given by

$$P(\lambda) = \frac{P_0}{1 + \left(2\,\dfrac{\lambda - \lambda_0}{FWHM}\right)^{2N_{cav}}}\,, \tag{2.3}$$

where P_0 is a global scale factor, λ_0 is the central wavelength of the prefilter, $FWHM$ is the full width half maximum of the prefilter and N_{cav} is the number of the cavities of the prefilter. This procedure is described in Section 2.5.4.

10. The restoration is done individually per scan. Therefore, there might be drifts and jumps between scans. Time dependent corrections and destretching are performed to avoid them. Image rotation is also corrected.

11. Pixel-by-pixel polarimetric calibration of the two beams. Further information about this procedure is found in Section 2.5.5.

12. The dual-beam setup is necessary for removing seeing-induced polarization (e. g., Lites, 1987; Casini et al., 2012). Before combining the demodulated data from the NB cameras, they have to be normalized because the gain of each NB camera is not exactly the same.

13. Telescope polarization compensation using the inverse of the modulation matrix of the telescope (Selbing, 2005)[4].

[4]This telescope model has been recently updated by de la Cruz Rodríguez et al. (2015).

14. Finally, the resulting spectropolarimetric images are stored in data cubes ready to be analyzed.

It should be clear that CRISP gives simultaneous pairs of NB images. The reduction of each one is performed individually and, at the end, they are combined to remove the seeing-induced polarization. Being specific to CRISP, the flat-field correction, image alignment, MOMFBD technique, polarimetric calibration and some additional processes are described in the following subsections.

All these steps are contained in the CRISPRED pipeline (Figure 2.6), which was developed at Stockholm University. More information about CRISPRED can be found in de la Cruz Rodríguez et al. (2015).

2.5.1 Flat-field correction

After the dark correction[5], the flat-field correction is an essential step during image calibration. Each pixel of a CCD has a certain gain, which is different from that of its neighbours. A pixel-by-pixel gain difference gives uneven response between pixels and this needs to be corrected. A flat image can be defined as the telescope-CCD system response to an uniform radiation source. The flat-field correction is performed via a normalization of each pixel by its gain. In solar physics, flat-field images are generated from numerous images obtained while the telescope is moving fast as close as possible to the disk center[6]. Taking into account how flats are obtained, one can expect that the spectrum recorded in each pixel is the spatially-averaged quiet-Sun profile at the disk center.

Due to the telecentric configuration of the etalons (Section 2.3), the filtergrams are affected by cavity and reflectivity errors that induce intensity fluctuations. It is necessary to correct them to perform image restoration, because the MOMFBD technique (see Section 2.5.3) cannot distinguish intensity fluctuations produced by atmospheric distortions from those due to the cavity errors. It computes deconvolutions to reconstruct data and such artificial variations cause artifacts in the restored images (especially during moments of bad seeing).

To achieve high precision, the cavity errors have to be known as accurately as possible. Cavity errors can be characterized by means of flat images following the strategy proposed by Schnerr et al. (2011). The fundamental idea is to distinguish in the summed flats between the spectral line information and the distortions produced by the etalons. According to this strategy, the recorded flat profiles are given by

[5]Even if no light is falling on the detector, charge will accumulate in each CCD's pixel. It is called dark current and arises because the CCD temperature is not 0 K. Thus, there are thermal fluctuations in the silicon lattice that can release electrons.

[6]In order to avoid intensity fluctuations due to the limb darkening (Sánchez et al., 1991).

$$I_{obs}(\lambda) \,=\, c_0\,(I_{QS}(\lambda) \,*\, T(e_{ch}, e_{hr}))\,\left(1 \,+\, \sum_{n=1}^{N} c_n\,\lambda^n\right)\,, \qquad (2.4)$$

where I_{obs} is the intensity observed in the pixel, λ is the wavelength, I_{QS} is the estimate of the spatially-averaged quiet Sun profile, T is the theoretical CRISP transmission profile (Equation 2.1), e_{ch} and e_{rh} are the high-resolution etalon cavity and the reflectivity errors, c_0 is the gain value that scales the entire profile, and the factor $\left(1 \,+\, \sum_{n=1}^{N} c_n\,\lambda^n\right)$ accounts for shifts of the prefilter. The $*$ sign denotes convolution.

The summed flat images are demodulated to avoid intensity fluctuations due to telescope polarization variations. Then, the quiet Sun profile giving rise to the spatially-averaged flat spectrum of each pixel is estimated by using spline interpolation functions. This estimated profile is shifted both in wavelength and intensity to fit it with each pixel spectrum. Thus, a first estimation of the cavity errors and the gain value of each pixel are obtained. In this first iteration, prefilter shifts and reflectivity variations (Equation 2.4) are assumed to be zero.

In the second iteration, the spectra of all the pixels are corrected for the cavity errors and gain values computed before. They are used to estimate a new quiet Sun profile ($I_{QS}(\lambda)$). From the second iteration onwards, the model used to compute CRISP-induced distorsions is more complex, because it includes all the elements shown in Equation 2.4. However, a model simplification is applied following de la Cruz Rodríguez et al. (2013), where reflectivities are considered constant across the FOV and reflectivity fitting is not needed, so that

$$I_{obs}(\lambda) \,=\, c_0\,I_{QS}(\lambda)\,\left(1 \,+\, \sum_{n=1}^{N} c_n\,\lambda^n\right)\,. \qquad (2.5)$$

This assumption greatly reduces the computation time because there are no convolutions and the averaged spectrum is fitted by spline functions. Figure 2.7 shows cavity-error maps obtained for our observations. They are shown in km s^{-1} to notice that these wavelength shifts are not neglectable, reaching values of order $pm1.5$ km s^{-1}. If science images are not corrected for this instrumental error, they will contain significant wavelength fluctuations over all the FOV that affect LOS velocity results, but even more important is this correction when searching for weak wavelength shifts (of order a few hundred m s^{-1}) because they are hidden.

After this procedure, the resulting flats are polarization free, do not contain the quiet Sun profile and do not show variations induced by instrumental errors. These are called cavity-error-free flats. They will be used for image restoration, giving smooth images. Once the filtergrams are restored, they are multiplied by the original flats (the true ones) and divided

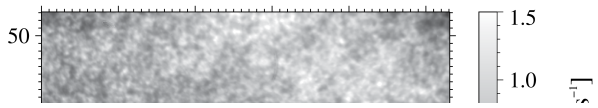

I
s

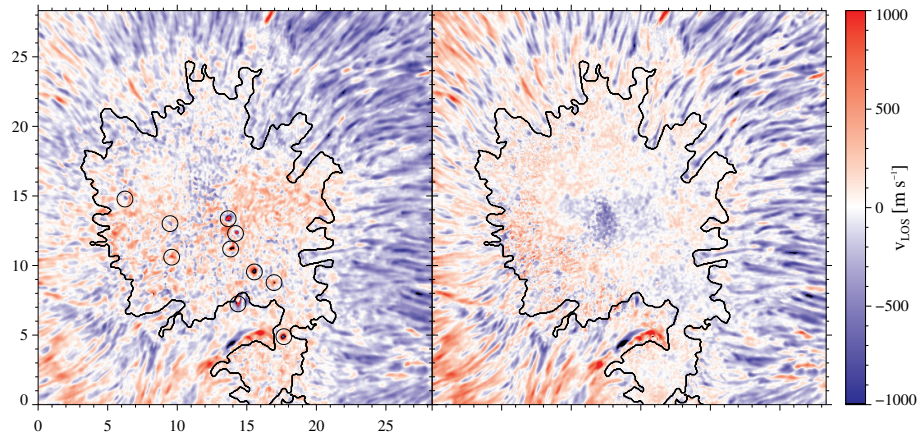

FIGURE 2.8:— Comparison of LOS velocities obtained following the flat-field correction as in Schnerr et al. (2011) (left panel) and as in de la Cruz Rodríguez et al. (2015) (right). Dopplergrams correspond at the 60 % bisector level (corrected for cavity errors, calibrated and filtered for subsonic oscillations). Axes are labelled in arcsecs. Black contours define the umbra-penumbra boundary. Black circles (in the left panel) enclose artifacts due to a bad estimation of the cavity errors.

by cavity-error-free ones. The reason is that cavity-error-free flats are actually used to alleviate shortcomings during the reconstruction process due to artificial intensity fluctuations contained in the flats, and after that, the restored filtergrams have got to be corrected for the original flats.

The left panel in Figure 2.8 shows a snapshot of the resulting LOS velocities in the umbra and in the inner penumbra. These velocities have been corrected for cavity errors and filtered for subsonic oscillations. Black cir-

cles surround examples of artifacts caused by an imprecise estimation of the cavity-errors when following to Schnerr et al. (2011). The LOS velocities of this artifacts are around ± 0.5 km s^{-1}, with values up to ± 2 km s^{-1}. Although they affect to all the FOV, these artifacts are more visible in low contrast regions where signals are more homogeneous (as the umbra and the inner penumbra). These small distortions were firstly detected while observing temporal evolution of LOS velocity because they are fixed to the camera and rotate with the image.

Therefore, the solution proposed by Schnerr et al. (2011) does not always work. The spectrum in sunspot is not similar to that of the quiet Sun, because of its shape and width. Thus, as the cavity errors are estimated using the quiet Sun profile, their effect on sunspots profiles is somehow different (de la Cruz Rodríguez et al., 2015). Therefore, these estimations need an additional correction. All the (non-restored) raw science images taken at the same wavelength are summed and used to calculate the intensity fluctuations introduced by the cavity errors (estimated before) on each pixel at each wavelength. Thus, the flats that are actually used by MOMFBD, $F_{MOMFBD}(\lambda, x, y)$, are computed as

$$F_{MOMFBD}(\lambda, x, y) = F_{cef}(\lambda, x, y) \frac{I(\lambda, x, y)}{I(\lambda - cav(\lambda, x, y), x, y)} \tag{2.6}$$

where $F_{cef}(\lambda, x, y)$ are the cavity-error-free flats, $I(\lambda, x, y)$ are the observed intensity profiles, and $I(\lambda - cav(\lambda, x, y), x, y)$ are the observed profiles corrected for the cavity error that corresponds to the (λ, x, y) position.

However, the correction given by Equation 2.6 is still not perfect because the raw science images are not restored yet and therefore they are affected by atmospheric distortions. To alleviate this problem, the cavity error map is decomposed into a high and a low frequency component following the method explained by de la Cruz Rodríguez et al. (2015). The result is shown in Figure 2.9. Considering that the seeing PSF given by MOMFBD has a limited extension (of order $4''$), the restoration is only affected by high-frequency intensity fluctuations (see the upper panel in Figure 2.9). As will be explained in Section 2.5.3, when restoring data, each image is divided into subfields to assure quasi-isoplanatism. Consequently, if there are non-negligible pixel-to-pixel intensity fluctuations due to the high-frequency cavity errors inside that subfield, artifacts appear in the restored images after deconvolution. Therefore, the flats used by MOMFBD are

$$F_{MOMFBD}(\lambda, x, y) = F_{cef}(\lambda, x, y) \frac{I(\lambda, x, y)}{I(\lambda - (cav(\lambda, x, y) + cav_{HF}(\lambda, x, y), x, y)} \tag{2.7}$$

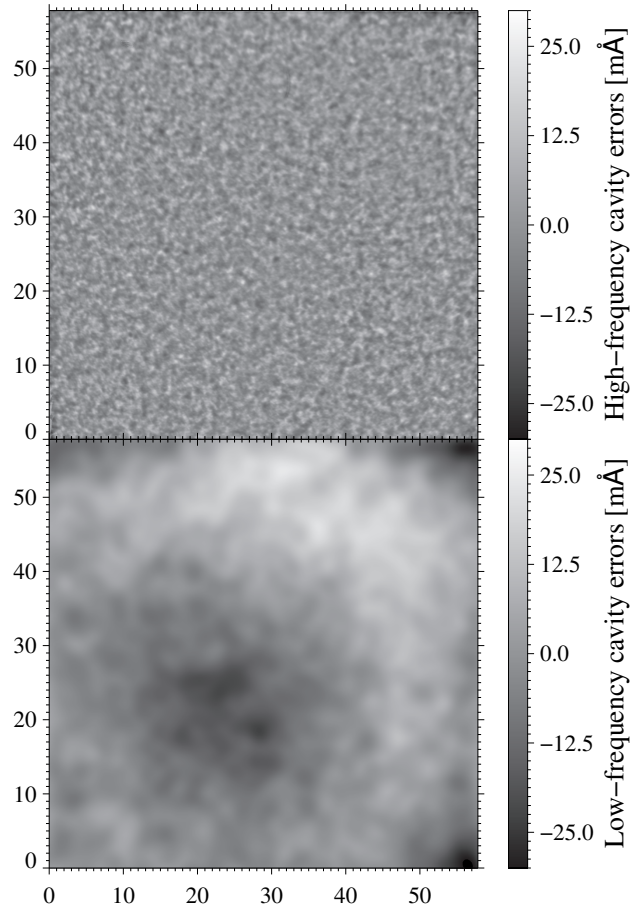

FIGURE 2.9:— Decomposition of the cavity-error map shown at the bottom panel of Figure 2.7 into the high-frequency (top) and the low-frequency (bottom) components. Axes are represented in arcsecs.

where $cav_{HF}(\lambda, x, y)$ are the high frequency intensity fluctuations. On the other hand, the low frequency cavity errors (the lower panel in Figure 2.9) have large scale intensity variations that do not affect image reconstruction. Thus, they can be corrected a posteriori.

Finally, as observed in the right panel of the Figure 2.8, the small-scale distortions present in the left panel have dissapeared and the low contrast regions are clearer when following the flat-field correction of de la Cruz Rodríguez et al. (2015). Therefore, a careful estimation of the cavity errors is crucial to obtain velocities that enable us to search for weak signals.

2.5.2 Image alignment

At the Schupmann focus, there is a pinhole array used to align images taken by the three cameras and to determine the image scale. It consists of an array of 12 x 12 tiny pinholes with a diameter of 30 μm. Their dimensions are very small to have uniform illumination.

Comparing the three summed pinhole images, one per camera, we find the relative orientation (rotation and flipping) and the shifts along the x and y directions. This is done by calculating the cross-correlation of two summed pinhole images with respect to the reference image -currently, the one taken by the transmitted camera-. Sub-pixel precision is needed in order to avoid artifacts during the reconstruction due to misalignments or scale size differences. The resulting parameters are stored and ready to be used by MOMFBD.

2.5.3 Image reconstruction using MOMFBD

Ground-based observations are affected by atmospheric turbulence. This randomly distorts the incoming wavefront, resulting in image motion, blurring, and geometrical distortions. AO is used to reduce low-order aberrations, but there are still some significant residuals due to higher-order aberrations that can be corrected employing image restoration techniques. These include speckle imaging (de Boer et al., 1992; von der Lühe, 1993), speckle deconvolution (Keller & von der Lühe, 1992), phase diversity (Gonsalves, 1982; Paxman et al., 1992; Löfdahl & Scharmer, 1994) and multi-frame blind deconvolution (MFBD; Löfdahl, 1996, 2002). Each one has its downsides, so the use of one or another depends on the characteristics of the observation. A review of image restoration techniques can be found in Löfdahl et al. (2007).

We use the MOMFBD technique to restore our images. MOMFBD is a variant of the MFBD technique that extends to multiple objects, i. e., multiple monochromatic images and polarization states. As MFBD, it considers the observed image as the convolution between an unknown object and an unknown PSF, plus some random noise. The blind deconvolution is able to estimate both quantities, but the problem is not unique. Some constraints need to be imposed: auxiliary information (optics and data collection model) or diversity (multiple frames, different focus positions), see Figure 2.10. MFBD methods work best when there is high contrast, short exposure and low noise. However, these conditions are very difficult to achieve in the observations.

In practice, the method separates the image information, which is fixed, from the variable seeing-induced effects. This is done by combining a large number of images per scan (in our case, 9 acquisitions x 4 polarization states x 30 wavelength positions x 2 NB cameras + 9 acquisitions x 1 WB camera).

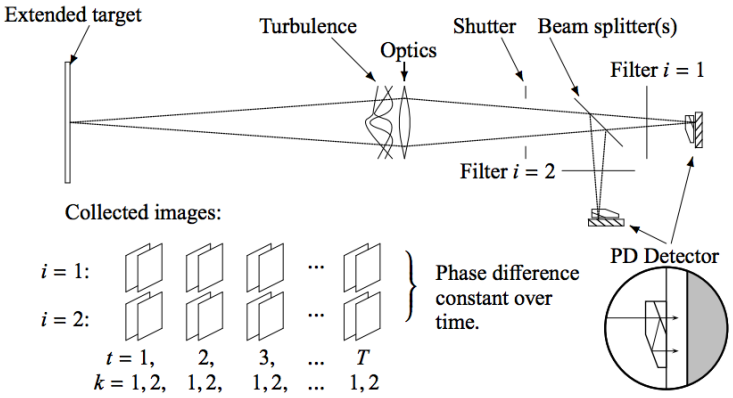

FIGURE 2.10:— Sketch of the data collection model. All the images taken at a certain instant, t, have the same realization of the seeing phase aberration. The *filters* indicate the position where are located polarizers or interference filters (depending on the observational setup) and define different diversity channels. Therefore, different objects i are given by the *filters* despite looking at the same solar region. The *PD detectors* are the cameras that collect images at different focus positions. From van der Noort et al. (2005).

The NB and WB images are restored simultaneously using the alignment information given by the pinhole arrays (van der Noort et al., 2005). As mentioned before, this method requires short exposures to somehow *freeze* the seeing, but as consequence the NB images have a low signal-to-noise ratio (SNR). Therefore, the WB filtergrams are combined to produce an anchor image of high SNR, which helps to constrain the estimated wavefronts. Besides, the images are far from being isoplanatic. For this reason, they are reconstructed in subfields where there is near-isoplanatism. Each subimage is compared to the data model and, using the solution that minimizes the Maximum Likelihood, an estimation of the object and the aberrations is obtained (Schulz, 1993). The latter are a combination of atmospheric turbulence -given by Zernike polynomials and Karhunen-Loève modes (Roddier, 1990)- and aberrations produced by the optical elements -described by Zernike polynomials (Noll, 1976). Therefore, there is a seeing PSF per subfield. Once all sub-images are reconstructed, they are combined again to form a coherent mosaic of the original image.

There are seeing distortions that are not possible to correct using image reconstruction. The NB states are not taken exactly at the same time and this causes residual differential seeing effects. Henriques (2012) suggested a strategy to overcome this problem. Every NB object is simultaneous to one of the WB objects and, hence, both are affected by the same seeing distortions. Thus, an extraset of WB objects (those that are strictly simultaneous to the NB ones) are introduced into MOMFBD. Then, the resulting reconstruction will produce one WB image per each NB image corresponding to a given wavelength and modulation state, where both have been reconstructed in

the same way. Later, each individual WB image will be aligned with the WB reference one to obtain a destretching[7] matrix that will be applied to the corresponding NB images.

2.5.4 Prefilter correction

As we have mentioned in Section 2.3, CRISP uses a prefilter to limit the spectral range. The counterpart is that the obtained spectra are weighted by the prefilter transmission profile and have to be compensated for this effect. To compute the Lorentzian profile of the prefilter (Equation 2.3), a process similar to that by Schnerr et al. (2011) is followed. First, the quiet Sun profile from the FTS atlas is degraded with the theoretical transmission profile of CRISP (Section 2.3) and the theoretical prefilter curve. The latter is a Lorentzian curve described here as

$$P(\lambda; p_1, p2, p_3, p_4, p_5) \;=\; \frac{p_1}{1 \,+\, \left(2 \,\cdot\, \dfrac{\lambda \,-\, p_2}{p_3}\right)^{2p_4}} \,\cdot\, (1 \,+\, \lambda \,\cdot\, p_5)\,, \qquad (2.8)$$

where λ is the wavelength offset from the line center, p_1 is a scaling factor, p_2 is the central wavelength of the prefilter, p_3 is the FWHM of the prefilter, p_4 are the cavities of the prefilter, and p_5 accounts for asymmetries in the prefilter curve. Thus, each parameter is iteratively changed to finally reproduce the quiet Sun profile computed from the flats (Section 2.5.1). After that, each profile in the reduced datacube is corrected for the resulting prefilter curve.

2.5.5 Polarimetric calibration

The polarization of the incoming light changes inside the telescope. It happens from the primary optics system -where there is also a rotation- until the polarizing beamsplitter located before cameras, without mentioning the fact that CRISP has two variable retarders that produce four polarization states as linear combinations of the Stokes parameters. Thus, the four linear independent combinations of the intensity parameters are related to the *real* Stokes vector as follows

$$I_{obs} \;=\; M_{table}(x, y)\, M_{tel}(\theta, \phi)\, I_{real}(x, y)\,, \qquad (2.9)$$

[7] Destretching (or dewarping) is a very useful technique when dealing with temporal sequence of images. It consists in computing geometrical distortions by using cross-correlation to measure differential image motion in small subfields. More information is found in Henriques (2013).

where I_{obs} is the observed Stokes vector, M_{tel} is the telescope matrix, M_{table} is the modulation matrix, and I_{real} is the Stokes vector coming from the Sun.

The strategy to compute M_{table} (Equation 2.2) is that of van Noort & Rouppe van der Voort (2008). By generating known polarization states at the exit window of the telescope, it is possible to compute the modulation matrix. For this purpose, after the observation a set of polarimetric calibration measurements are taken using a linear polarizer and a quarter-wave plate. The linear polarizer is fixed at 0 and 90° and the quarter-wave plate rotates 360° in steps of 10°. From the known input Stokes parameters and the four intensity measurements corresponding to each of them, one can infer the modulation matrix and hence the demodulation matrix. The PSFs obtained for each patch during the MOMFBD process are used to convolve the demodulation matrix and these blurred versions are applied to the reconstructed images on a pixel-by-pixel basis. Then, the NB beams are normalized to the mean intensity -because the gains of each camera are different- and combined to remove seeing-induced polarization.

Next, the telescope polarization is compensated using the inverse of the Mueller matrix of the telescope (Selbing, 2005). This matrix depends on the wavelength and the telescope pointing during the observation.

Afterwards, we obtain homogeneous temporal sequences of WB images computing time dependent corrections. Later, these corrections are applied to the NB images in the same way as in the WB images. Finally, datasets are organized in sequential cubes and ready to be analyzed.

3

Lateral downflows in penumbral filaments

Be less curious about people
and more curious about ideas.
Marie Curie

3.1 Introduction

The transport of gas and energy in sunspots penumbrae has been intensely debated for decades. As mentioned in Chapter 1, existing theoretical models attempt to explain it by means of different mechanisms, such as siphon flows, magnetic flux tubes, or regular convection. There is consensus that convection may exist in the penumbra. Besides, 3D MHD simulations of penumbral filaments have supported overturning convection as the mechanism responsible for mass motions in sunspots (see Section 1.5). According to the simulations, the velocity field of a filament is formed by an upflow at the center, weak downflows at its lateral edges and a stronger downflow at the end (see Section 1.6). This pattern is similar to that of granular cells in the quiet Sun.

Some authors who studied the penumbral velocity field failed to find lateral downflows (e.g., Bellot Rubio et al., 2004; Borrero et al., 2005; Franz & Schlichenmaier, 2009; Bellot Rubio et al., 2010; Franz, 2011). For this reason, there are doubts about the existence of overturning convection . However, recently Scharmer et al. (2011) and Joshi et al. (2011) disclosed the presence of lateral downflows in penumbral filaments in the lower photosphere using high-resolution spectropolarimetric data acquired with CRISP at the SST. After that, other authors have also found the presence of lateral downflows,

such as Scharmer & Henriques (2012), Ruiz Cobo & Asensio Ramos (2013), Scharmer et al. (2013) and Tiwari et al. (2013). However, the limitations of these analyses raise doubts about their results. In some cases, the data were deconvolved (Scharmer et al., 2011; Joshi et al., 2011; Scharmer & Henriques, 2012; Ruiz Cobo & Asensio Ramos, 2013; Scharmer et al., 2013). The sunspots were located relatively far from disk center in all studies (except that of Tiwari et al., 2013). Finally, some of the spectral lines used have problems that may affect the velocity field calculation.

Here, we study the small-scale velocity field of a sunspot penumbra located close to the disk center using a very stable time sequence of high-resolution spectropolarimetric data. We observe lateral downflows at the edges of penumbral filaments. These downflows are visible in the Dopplergrams without any deconvolution of the data. Our main goal is to characterize them and analyze their temporal evolution.

3.2 Data analysis

We construct LOS velocity maps using line bisectors. Bisectors are calculated from the observed intensity profiles using linear interpolation, after spectral gradients due to the CRISP prefilter have been removed (Section 2.5.4).

We focus on bisectors at the 50, 60 and 70 % levels, to progressively sample deeper layers of the photosphere in each pixel. The Evershed flow is stronger close to the continuum forming layer (e.g., Rimmele, 1995; Westendorp Plaza et al., 2001; Bellot Rubio et al., 2003), so in principle bisectors at high intensity levels are advantageous to detect the weak signals expected from lateral downflows.

We have removed the 5-minute photospheric oscillations from the velocity maps using a Fourier filter with cut off speeds of 5 km s^{-1} (Title et al., 1989; Straus et al., 1992).

3.2.1 Calibration of LOS velocity maps

The spectral lines observed in the Sun are shifted in wavelength by a number of reasons. Therefore, it is necessary to calibrate them with respect to a reference zero velocity. Depending on the characteristics of the observed target, there exist different techniques. Due to the very high accuracy required to detect the weak signals created by small-scale convection, it is necessary to emphasize the importance of this step to obtain reliable velocities.

First of all, we must consider the properties of the Fe I 617.3 nm spectral line (Section 2.4) to select the most suitable technique. We cannot use telluric lines to perform the wavelength calibration since none is present in our spectral range. According to Beckers (1977), there are no vertical velocities

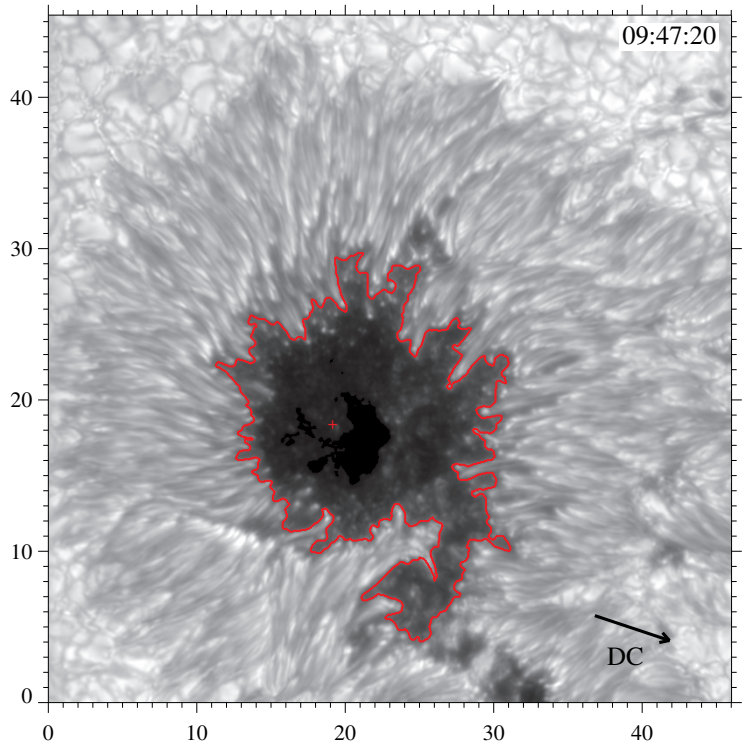

FIGURE 3.1:— Continuum intensity filtergram where the umbra-penumbra boundary is shown with a red contour. The enclosed umbral points have a continuum intensity of less than 0.45 I_{QS}. The axes are labelled in arcsec. The red plus symbol shows the position of the Stokes I and V profiles plotted in Figure 3.2.

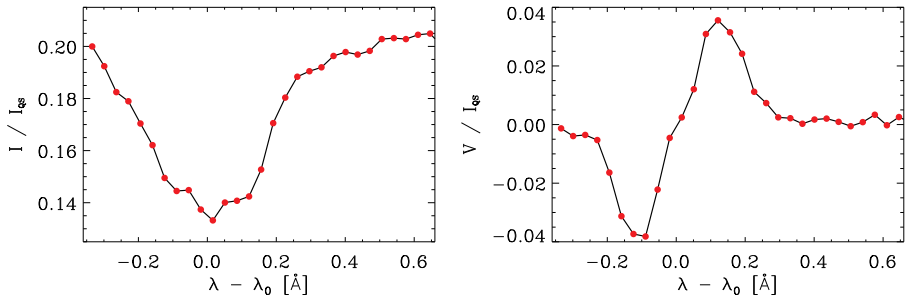

FIGURE 3.2:— Stokes I and V profiles (left and right, respectively) from the umbral point shown with a plus symbol in Figure 3.1.

in sunspot umbrae due to the inhibition of convection. Such a reference should be uncertain by less than 100 m s^{-1}. Therefore, similarly to Watanabe et al. (2012), one can consider the LOS velocities of the darkest umbral

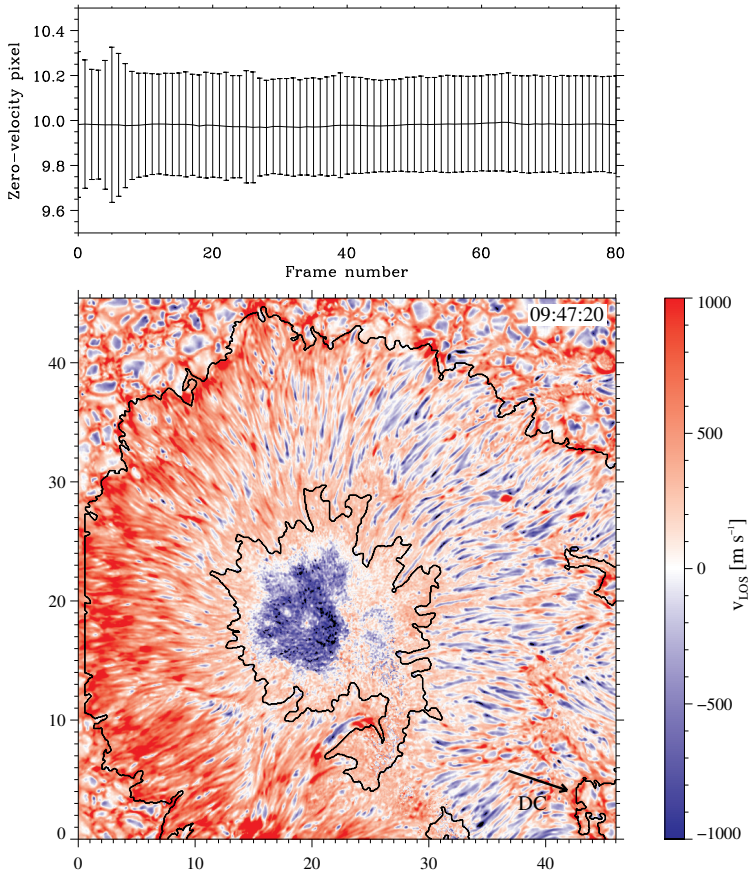

FIGURE 3.3:— The upper plot displays the wavelength reference and its standard deviation per frame using the average 70 % bisector value of the darkest umbral points. The lower panel shows a calibrated Dopplergram. The arrow points to the disk center.

positions (here, where the continuum intensity is less than 0.45 I_{QS}[1], as shown in Figure 3.1) and average them per frame to derive the reference velocity. However, these points have distorted Stokes I profiles (left panel of Figure 3.2). This distortion could be produced by blends. According to Norton et al. (2006), the Fe I 617.33 nm line seems to be affected by an Eu II 617.30 nm blend and two other molecular lines in very cold umbrae.

The lower panel of Figure 3.3 shows a Dopplergram at the 70 % intensity level that has been calibrated using the average 70 % bisector value of the darkest umbral points. The Dopplergram shows a systematic redshift all over the FOV. In fact, the Evershed effect is barely noticeable. LOS velocity variations in the umbra are large, with a strongly blueshifted region. The upper plot shows the zero-velocity reference and the corresponding standard deviation per frame, in pixels along the spectral direction. Although this

[1]We selected this value because it better fits the umbra-penumbra border.

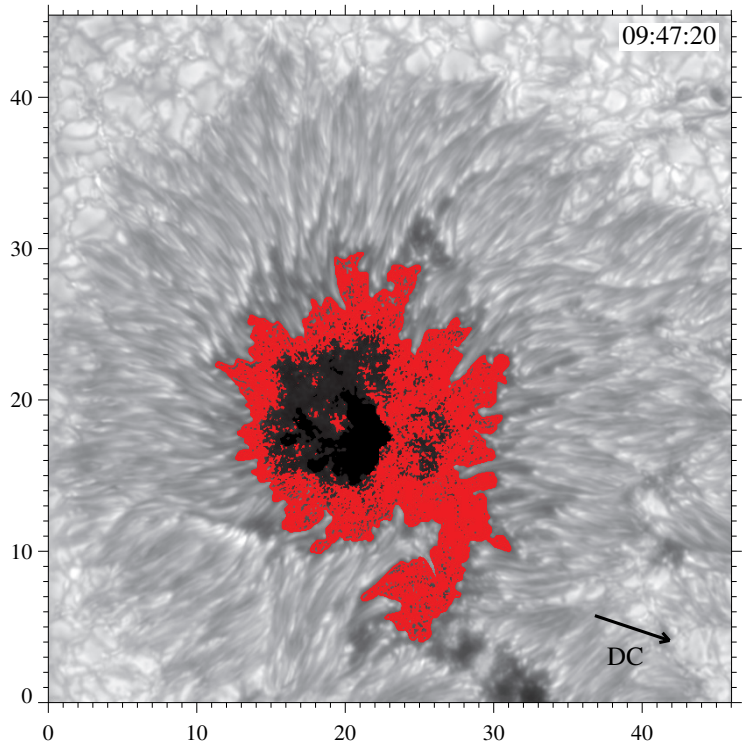

FIGURE 3.4:— Umbral pixels with Stokes V amplitude asymmetry smaller than 4 % overplotted on the continuum intensity filtergram of Figure 3.1. The axes are labelled in arcsecs. The arrow points to the solar disk center.

reference seems to be stable (with an rms fluctuation of 9 m s^{-1}), the typical standard deviation of the LOS velocity of the umbral points used to compute the velocity reference is 380 m s^{-1}, which is very high for a region that is expected to be approximately quiet. So this method was discarded.

The second option was to use the quiet Sun profiles to perform the LOS velocity calibration. It consists in comparing the mean quiet Sun profile of each frame with the FTS profile convolved with the CRISP transmission profile and the prefilter curve (Section 2.3 and 2.5, respectively). However, the sunspot is very big and the quiet Sun regions are confined to the corners of the FOV (see Figure 3.1). Besides, the cavity errors maps are less accurate as we move away from the center (de la Cruz Rodríguez, , private communication). Therefore, this velocity reference would be wrong.

As shown in the right panel of Figure 3.2, the Stokes V profiles observed in the umbra are not distorted. Therefore, we decided to calibrate Dopplergrams using their zero-crossing wavelengths. In order to avoid possible molecular blends, we selected all umbral pixels with Stokes V amplitude asymmetries smaller than 4 %. Each Stokes V lobe was fitted to a parabola using three points around the peak in order to compute the lobe amplitude.

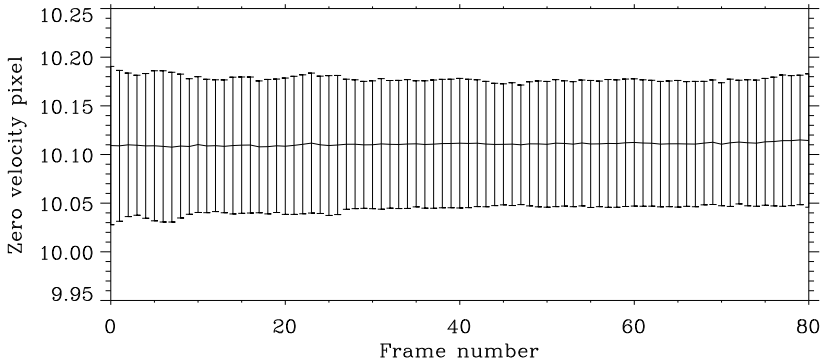

FIGURE 3.5:— Zero-velocity reference and its standard deviation as a function of time using the umbral values with Stokes V amplitude asymmetries smaller than 4 %. One spectral pixel corresponds to $\Delta\lambda = 35$ mÅ, or 1.75 km s^{-1}.

This criterion is met by approximately 60 % of the umbral points, as shows Figure 3.4. For each Dopplergram, the zero point of the velocity scale is taken to be the average Stokes V zero-crossing wavelength of the umbral pixels selected in that frame. Figure 3.5 displays the reference value and its corresponding standard deviation as a function of time. The typical standard deviation of the zero-crossing points used to compute the zero velocity reference is 110 m s^{-1}. This can be considered the uncertainty of our velocity calibration. The standard deviation of the average Stokes V zero-crossing points in the different line scans is 3 m s^{-1}.

3.3 Penumbral velocity field

In this Section, we investigate the penumbral velocity field on all spatial scales accesible to our observations. Figure 3.6 shows a Dopplergram of the spot computed from the bisector at the 70 % intensity level. The full Dopplergram sequence is available at spg.iaa.es/downloads

Despite the small heliocentric angle of the sunspot, the Evershed effect is clearly seen in Figure 3.6. The limb-side and center-side penumbrae are redshifted and blueshifted, respectively, indicating motions away from and to the observer. These motions become stronger toward the outer sunspot boundary. The observed pattern of Doppler shifts demonstrates that the penumbral flow is, to first order, a radially directed outflow whose inclination to the vertical steadily increases toward the outer penumbra. The picture does not differ much from previous results (e.g., Schlichenmaier & Schmidt, 2000; Mathew et al., 2003; Bellot Rubio et al., 2004; Rimmele & Marino, 2006; Franz & Schlichenmaier, 2009). However, the very high spatial resolution of our observations allows us to identify individual flow channels with unpre-

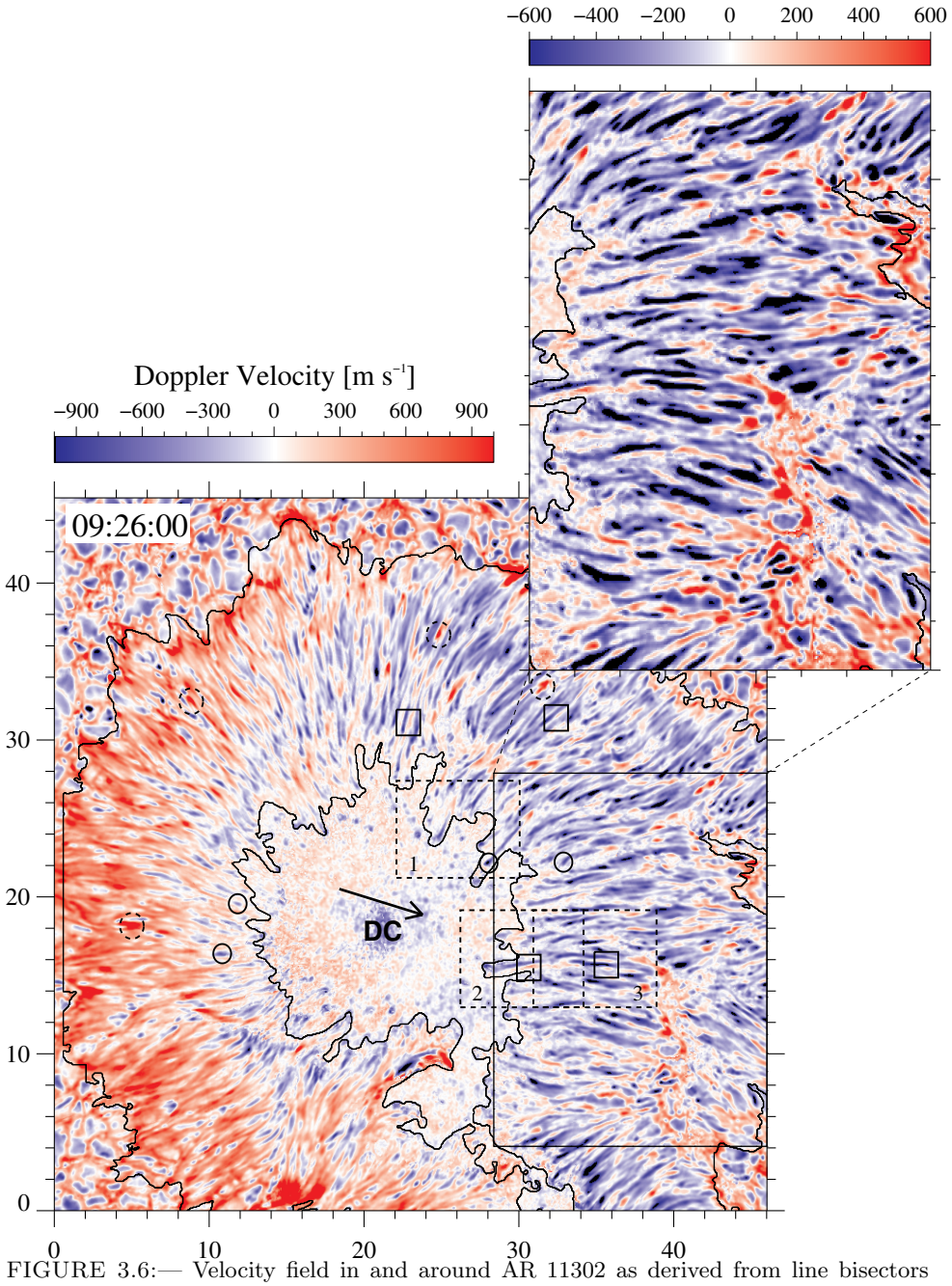

FIGURE 3.6:— Velocity field in and around AR 11302 as derived from line bisectors at the 70 % intensity level in the penumbra and from the Stokes V zero-crossing wavelengths in the umbra. Both axes are in arcsec. The arrow points to the solar disk center and contours outline the inner and outer boundaries of the penumbra. Solid circles show examples of penumbral grains, dashed circles mark strong returning Evershed flows, and small squares enclose lateral downflows. The dashed rectangles labeled 1-3 identify the areas used in Figures 3.9-3.11. A center-side penumbral region is enlarged and displayed with a different scale to better illustrate the existence of lateral downflows at the edges of penumbral filaments.

cedented accuracy. Elongated, extremely thin flow structures are observed to stretch radially outward for a few arcsecsonds in the velocity map. These structures often (but not always) coincide with bright penumbral filaments.

The flow channel heads display conspicuous, localized patches of enhanced blueshifts regardless of their position in the spot, although they are easier to detect in the inner penumbra because this region is less cluttered. The solid circles in Figure 3.6 mark prominent examples. The strong blueshifts represent upward motions and can be considered to be the sources of the hot Evershed flow. They always occur at the position of bright penumbral grains (Rimmele & Marino, 2006; Ichimoto et al., 2007b). Our observations show them with typical sizes of $0\farcs2$, in agreement with previous studies.

The tails of the flow channels, especially those near the outer penumbral edge, often display strong redshifts. These patches represent the locations where the Evershed flow returns to the solar surface (e.g. Westendorp Plaza et al., 1997, 2001), now observed with unprecedented clarity as separate structures. They can be identified most easily in the center-side penumbra, thanks to their large contrasts over the blue background. Examples are marked with dashed circles in Figure 3.6. The downflows occurring in these patches are supersonic and nearly vertical (Bellot Rubio et al., 2010; van Noort et al., 2013), although the bisector analysis yields modest LOS velocities of order 2 km s^{-1}. Such supersonic Evershed flows will be studied in detail in Chapter 5.

3.3.1 Lateral downflows

In addition to these flow structures, our Dopplergrams reveal the existence of a new flow component producing small patches of weak redshifts in between the flow filaments. They are observed everywhere across the spot, except in the limb-side penumbra where the prevailing redshifts hide them efficiently. By contrast, these patches are very conspicuous in the center-side penumbra and the region perpendicular to the symmetry line. Examples of such lateral redshifts are indicated in Figure 3.6 with small squares. Their general properties can be summarized as follows:

1. They are associated with flow channels. Sometimes the redshifts can be observed on both sides of the filament, but most often they appear only on one side.

2. Their sizes vary from small roundish patches $\sim 0\farcs15$ in diameter to elongated, narrow structures flanking the flow filaments for more than $\sim 1''$.

3. In the center-side penumbra, they show bisector velocities ranging from $\sim$100 to $\sim$500 m s^{-1} at the 70 % intensity level. These flows are therefore much weaker than those observed in the adjacent filaments.

4. Their velocities are stronger in deeper photospheric layers. In the center-side penumbra, they exhibit mean maximum velocities of 165, 195 and 210 m s^{-1} at the 50, 60 and 70 % intensity levels, respectively.

What do these flows represent? The Doppler velocities displayed in Figure 3.6 are projections of the actual velocity vector to the LOS. Therefore,

- Along the symmetry line, only radial and vertical motions can contribute to the LOS velocity. The center-side penumbra near the symmetry line is dominated by the blueshifts produced by the radial Evershed outflow. Any redshift observed there must be due to vertical downflows or to inward horizontal motions. The latter can be ruled out because the structures move outward rather than inward (see Section 4.3). Thus, the lateral redshifts must correspond to downflows.

- Perpendicularly to the symmetry line, only horizontal flows along the azimuthal direction (i.e., perpendicular to the penumbral filament axis) and vertical flows can produce non-zero LOS velocities. The global reduction of the LOS velocity observed there is caused by the vanishing contribution of the radial Evershed flow. In that part of the spot, however, we still detect small redshifted patches in between the penumbral filaments. Since they often occur in pairs on either side of the same flow channel, they cannot be due to horizontal motions away from the filament, as those motions would produce velocity patches of opposite sign. In addition, due to the small heliocentric angle of the spot, one would need very large azimuthal flows to explain the observed LOS velocities. Therefore, also in this region we conclude that the redshifted patches represent vertical motions away from the observer, i.e., downflows.

Figure 3.7 shows the location of the downflows relative to the intensity structures. On top of the continuum intensity filtergram, red pixels indicate bisector velocities larger than 100 m s^{-1} at the 70 % intensity level. As can be seen, the lateral downflows tend to appear next to penumbral filaments, but sometimes they occur at their edges or even right on them. As a consequence, the lateral downflows are not always associated with dark structures.

Figure 3.8 displays the intensity profiles emerging from a blueshifted penumbral filament (central panel) and its two lateral downflows (right and left panels). The exact location of the profiles is marked with plus symbols in the close-up of Figure 3.11. Also depicted are the corresponding line bisectors for intensity levels from 0 to 80 %. As can be seen, the profiles emerging from the lateral downflows have slightly darker continua than the flow channel. Other properties such as line widths are similar. The lateral downflows produce bisectors with larger redshifts at higher intensity levels, indicating the existence of velocities that increase with depth in those pixels.

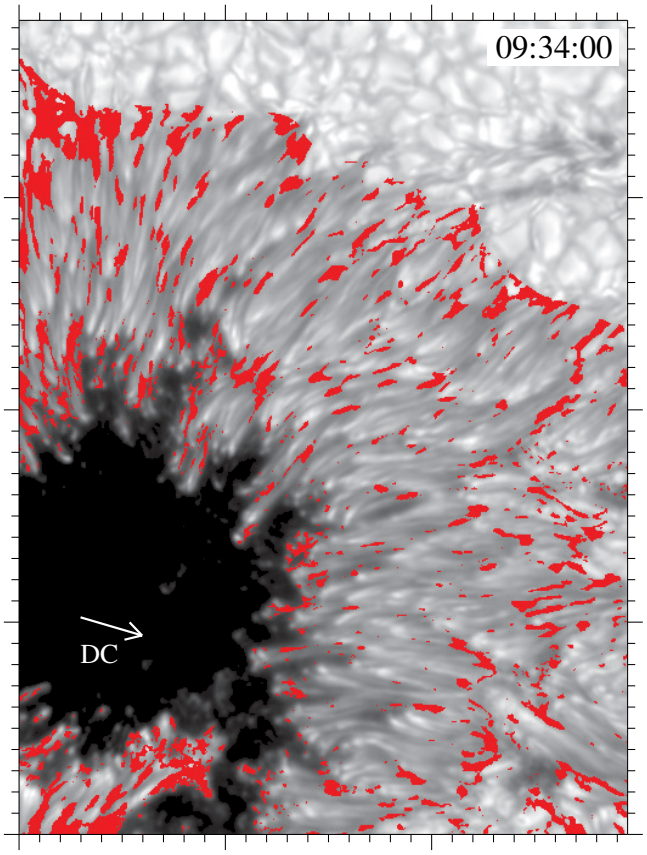

FIGURE 3.7:— Spatial distribution of downflows in the penumbra of AR 11302. Red pixels represent locations with bisector velocities larger than 100 m s^{-1} at the 70 % intensity level, overplotted on the continuum intensity filtergram.

The bisector at the position of the flow channel reveals upflows of order 800 m s^{-1} that do not change much throughout the atmosphere. These spectral properties reveal the different nature of the central upflows along the filament and the lateral downflows.

3.4 Temporal evolution of the lateral downflows

We have selected three examples to illustrate the evolution of the lateral downflows (Figures 3.9-3.11). They are located at different positions across the center-side penumbra (dashed rectangles in Figure 3.6). Movies covering their entire evolution are available at spg.iaa.es/downloads

3.4.1 Example 1

Figure 3.9 shows a region perpendicular to the symmetry line in the inner penumbra. Two bright filaments protruding into the umbra can be

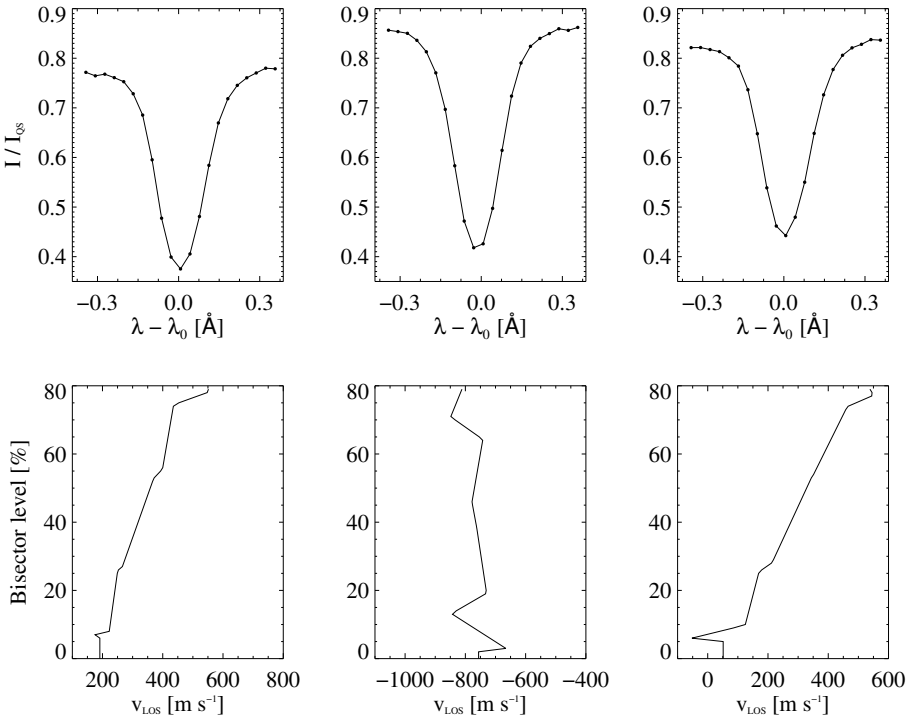

FIGURE 3.8:— Top row: intensity profiles emerging from a blueshifted flow channel (central panel) and its lateral downflowing regions (right and left panels). The positions of the selected pixels are marked in Figure 3.11 with plus symbols. Bottom row: line bisectors calculated between the 0 and 80 % intensity levels.

seen in the intensity maps (left column). They appear in the Dopplergrams (right column) as two blueshifted flow channels headed by roundish patches that also harbor blueshifts. Since the filaments are nearly perpendicular to the symmetry line, the LOS velocity is the result of azimuthal and vertical motions. Following the arguments in Section 3.3, these blueshifts represent the upward component of the Evershed flow in the penumbra, with velocities of up to 800 m s^{-1}.

Small redshifted patches can be seen next to the two penumbral filaments. We have identified them with red contours. They never cover the entire length of the filaments, but appear as patchy, more or less elongated structures close to their edges. In the intensity images, they are located next to bright structures or even superposed on them. Sometimes we see the redshifts only on one side of the filament, sometimes on both sides, evolving independently of each other. Given their location, the redshifts are unlikely to be produced by azimuthal motions and must rather be considered as downward motions.

The lateral downflows depicted in Figure 3.9 are intermittent. They

usually have lifetimes of a few minutes, although the bigger ones are recognizable for up to 10 minutes. Their velocities remain more or less stable with time, but they can split into smaller fragments and/or merge with neighboring patches from one frame to the next. These processes may simply be the result of an inhomogeneous distribution of downward velocities along the filament length, with regions of enhanced flows which are easy to detect and areas of weaker flows that can go largely unnoticed. If these velocities change with time one may get the impression that the patches split and mere, while in reality there exists only one long patch covering the full filament length. An inhomogeneous velocity distribution can also result in apparent drifts of the strongest downflowing patches, as is often observed.

3.4.2 Example 2

Our second example is shown in Figure 3.10. Now, the filaments are located nearly parallel to the symmetry line and the LOS velocity is mostly due to radial and vertical motions. We see a conglomerate of filaments protruding into the umbra. Small patches of redshifts appear and evolve individually around the most prominent one. Again, these redshifts are in the center-side penumbra and must be caused by downward motions.

The lateral downflows of Figure 3.10 are also intermittent, because they appear and disappear with time. They interact with each other, merging and splitting in smaller parts as described before. However, the downflowing patches do not evolve in a completely independent way here. In the first frame we observe the blueshifted channel above a bead-like string of lateral downflows of differents sizes. The blueshifted region moves downward (in the plane of the paper), interchanging position with the lateral downflows in the second frame. There is a similar transition between the fourth and fifth frames, as the blueshifted filament moves upward and interchanges position with the redshifted patches that are mostly seen again on the other side. Therefore, in this example the lateral downflows appear to follow or react to the motion of the flow filament.

3.4.3 Example 3

Our last example corresponds to a mid-penumbral region where the filaments are well aligned with the symmetry line (Figure 3.11). The Dopplergrams show elongated flow channels harboring blueshifts. These structures are difficult to trace in the continuum images because of their low contrast and the complexity of the region. As in the previous example, the LOS velocity represents the projection of the radial and vertical components of the velocity vector, since the azimuthal component is perpendicular to the LOS. The selected region contains several examples of weak lateral downflows, but we will focus on the ones marked with contours.

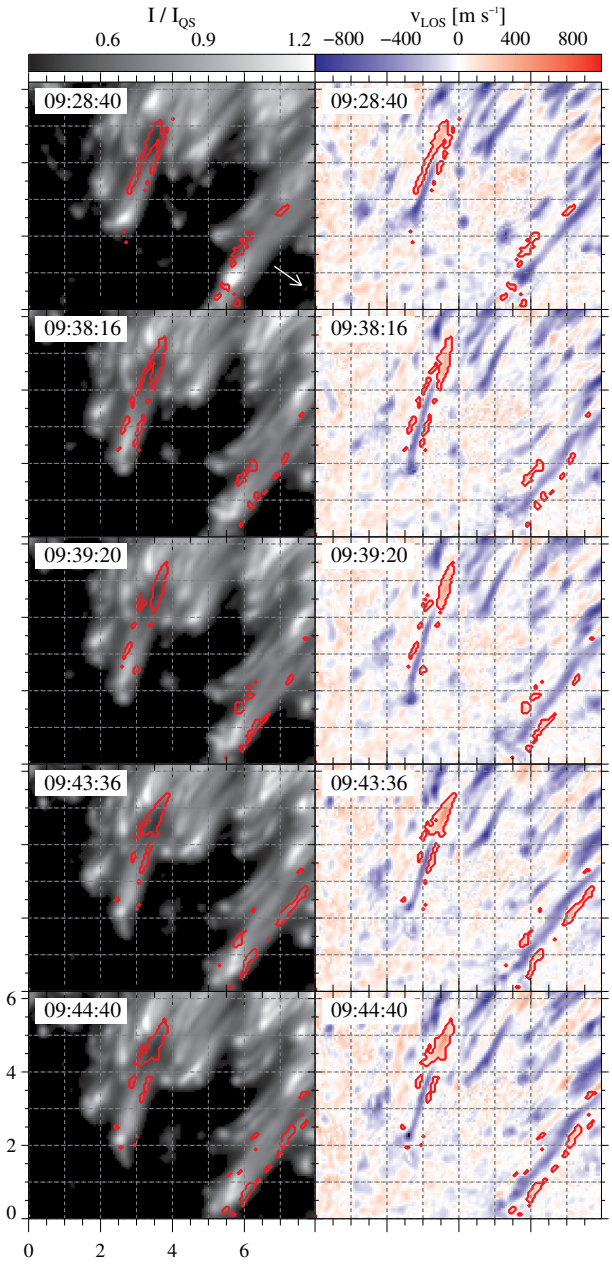

FIGURE 3.9:— Temporal evolution of lateral downflows in penumbral filaments located perpendicularly to the symmetry line (case 1). The intensity filtergrams in the left column have been corrected for a stray light contamination of 40 % (see Section 3.5). The velocity maps in the right column display the bisector velocities at the 70 % intensity level without any stray light correction. Red contours outline redshifts greater than 100 m s^{-1}. The frames are not contiguous in time, as indicated in the upper right corner of each panel. The white arrow plotted in the first intensity panel points to the disk center. Axes are labelled in arcsec.

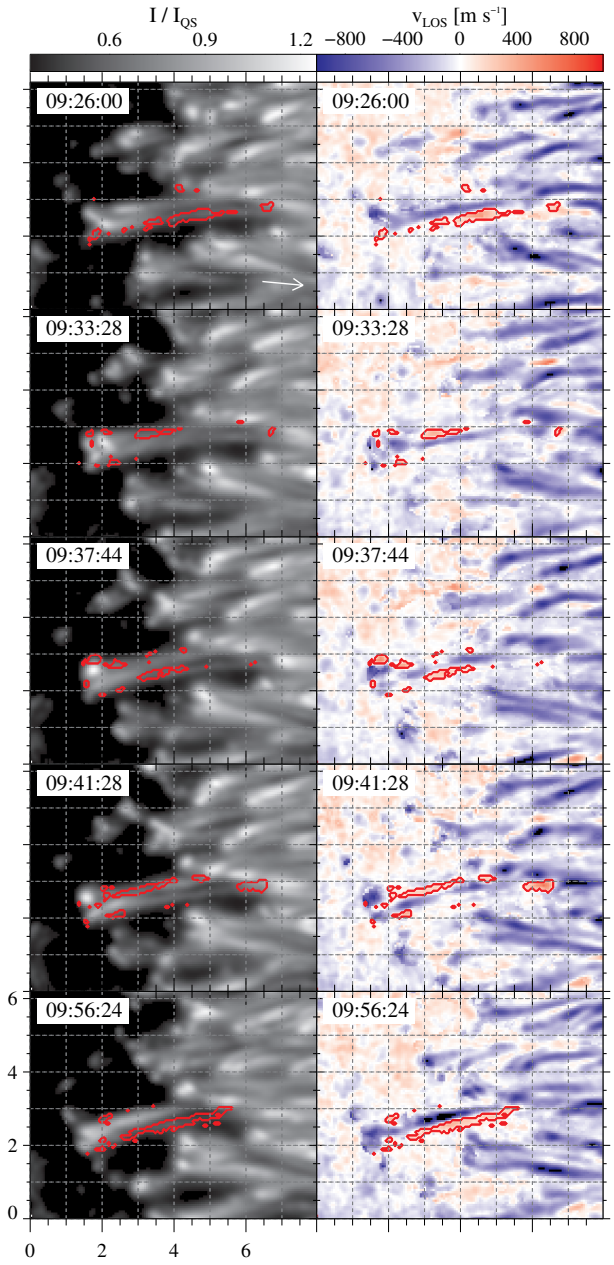

FIGURE 3.10:— Example of lateral downflows located at the edges of a conglomerate of filaments protruding into the umbra near the symmetry line (case 2). The layout is the same as in Figure 3.9.

Initially, no redshifts can be observed at the edges of the central flow channel. In the second frame, two redshifted regions have appeared. The onset of the redshifts is perhaps triggered by a significant velocity increase occurring in the filament, from -500 to -1000 m s^{-1}. The patches are lo-

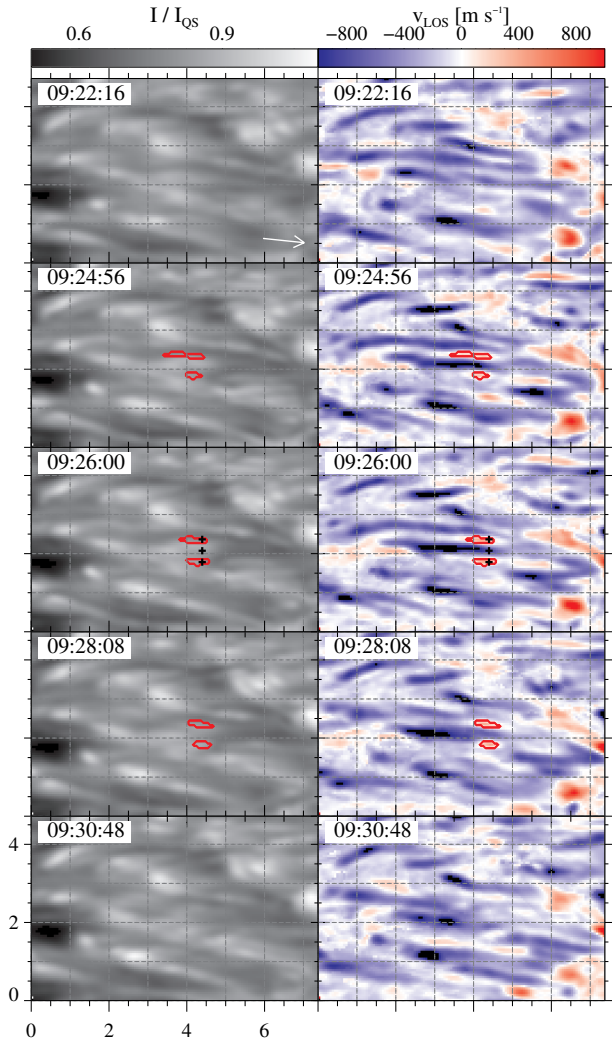

FIGURE 3.11:— Lateral downflows at the edges of a filament located in the middle penumbra near the symmetry line (case 3). The layout is the same as in Figure 3.9. The plus symbols at 09:27:04 UT mark the pixels represented in Figure 3.8.

cated on either side of the filament, approximately at the positions of the strongest blueshifts. One of them is more elongated than the other. The lateral downflows move outward between the second and third frames. By then, their sizes are approximately the same and their velocities have increased from 250 to 400 m s^{-1}. They no longer flank the strongest blueshifts, which have moved slightly inward. In the fourth frame, the redshifts are further outward, close to the filament tail. Their areas are still similar, but the velocities have decreased back to 250 m s^{-1}. In the last frame the redshifts have been replaced by blueshifts. This suggests that the development of blues-

hifts ultimately determines the appearance and visibility of the downflowing patches.

3.5 Stray light compensated data

In this Section we show the velocities resulting from our observations after deconvolving them with different levels of stray light, to allow direct comparisons with Scharmer et al. (2011, 2013) and Scharmer & Henriques (2012). The existence of stray light contamination, its importance, and nature are still a matter of debate (see Löfdahl & Scharmer, 2012; Schlichenmaier & Franz, 2013; Scharmer, 2014).

We compensate for stray light in the same way as Scharmer et al. (2011). Assuming that I_t is the true intensity emerging from a pixel at a given wavelength and polarization state, the observed intensity I_0 is degraded by stray light as

$$I_0 = (1 - \alpha)I_t + \alpha I_t * P \tag{3.1}$$

where α represents the fraction of stray light contamination and P is a Gaussian PSF with a full width at half maximum (FWHM) W. The symbol $*$ denotes convolution. Therefore, to obtain the true intensity one needs to deconvolve the original data with some values of α and W. The parameters used by Scharmer et al. (2011, 2013) and Scharmer & Henriques (2012) are summarized in Table 1.1.

Figure 3.12 shows the lateral redshifts observed in the original Dopplergrams (left) and in the straylight compensated Dopplergrams, for stray light contamination of 40 % (center) and 58 % (right), and FWHM values of $W = 1\farcs8$ and $W = 1\farcs2$, respectively. The velocities correspond to the bisector shifts at the 70 % intensity level. They are overplotted on the continuum images resulting from the different deconvolutions.

As expected, the deconvolved continuum images show higher contrasts than the original data. The granulation pattern stands out more prominently as the stray light fraction increases, primarily because the intergranular lanes become darker. Also the penumbral filaments and the outer penumbral border are more clearly defined. In the deconvolved Dopplergrams, umbral dots, penumbral grains, and dark cores of penumbral filaments show higher contrasts than in the original data.

When no stray light compensation is carried out (left panel in Figure 3.12), the lateral downflows detected in the center-side penumbra have typical velocities of less than 300 m s^{-1}. At the tail of penumbral filaments, we see patches with velocities that often exceed 1500 m s^{-1} and correspond to Evershed flows returning bask to the solar surface. The velocities are always stronger at the center of the patches, for both types of structures.

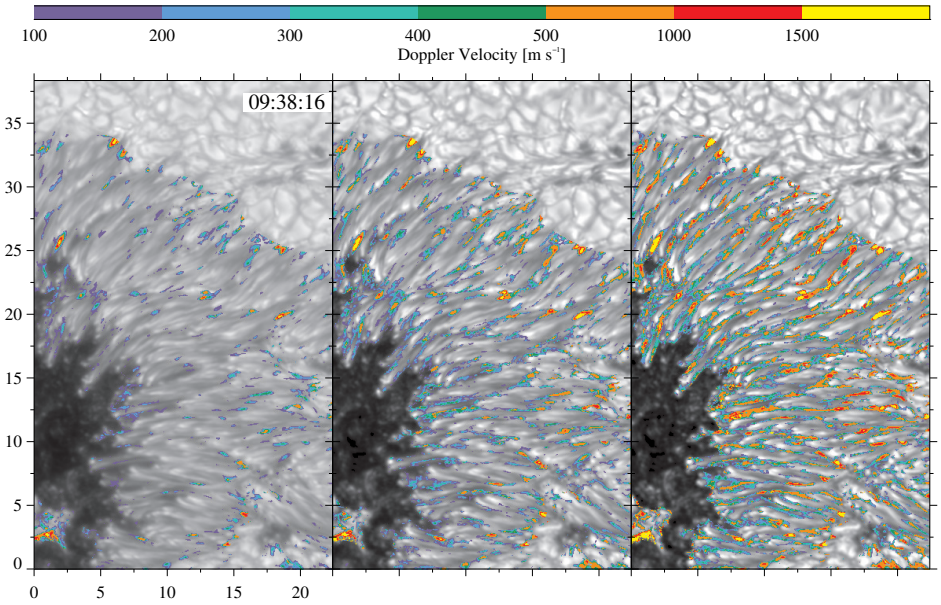

FIGURE 3.12:— Comparison of the Doppler velocities to the red resulting from the original and deconvolved data. From left to right: original observations, compensation for 40 % stray light contamination, and compensation for 58 % contamination.

This translates into concentric LOS velocity contours (most easily seen in the case of the final downflows).

The stray-light-compensated data (center and right panels in Figure 3.12) show the same redshifted patches, with larger areas and LOS velocities, plus new patches that were not visible originally and show up only after deconvolution. Correcting the data for a straylight contamination of 40 % increases the LOS velocities of the lateral downflows by a factor of two on average. Scharmer & Henriques (2012) found a similar behavior. The downflows associated with returning Evershed flows undergo slightly smaller enhancements. As expected, the velocity increase is even stronger in the data compensated for a stray light contamination of 58 %, with individual lateral downflows reaching up to 475 m s^{-1} compared with the ∼150 m s^{-1} of the original data.

Our results suggest that the lateral downflows detected by Scharmer et al. (2011, 2013) and Scharmer & Henriques (2012) in deconvolved images are probably not mathematical artifacts. Some of those redshifts are actually visible in the original observations, and so they are not created by noise amplification or by the data deconvolution (see the examples in Schlichenmaier & Franz, 2013). We cannot say much about the other structures that show up in the deconvolved images, as they are the result of enhancing inconspicuous signals in the original filtergrams.

3.6 Summary

We have analyzed the small-scale velocity field and its temporal evolution of a sunspot penumbra using high-resolution spectropolarimetric measurements in the Fe I 617.3 nm line. The excellent seeing conditions, accurate data reduction, precise wavelength calibration, high temporal cadence and the location of the sunspot very close to the disk center all contribute to make this an unprecedented dataset for sunspot studies.

We report the ubiquituous presence of lateral downflows in penumbral filaments. For the first time, these elusive features are detected without correcting the data for stray light, avoiding the controversies associated with such methods (Schlichenmaier & Franz, 2013). We have removed the undesired imprint of p-modes from the Dopplergrams using Fourier filtering. The resulting velocity maps are less veiled and the signals more stable, as p-modes can make large areas appear completely blueshifted (hiding the lateral downflows) or redshifted (producing artificial downflows). This correction has not been performed previously.

Lateral downflows appear in our Dopplergrams as elongated redshifted patches surrounding the upflowing penumbral filaments. In the centerside penumbra, they stand out conspicuously over the dominant blueshifts associated with the Evershed flow. By studying examples in different parts of the spot we have been able to rule out radial and azimuthal motions as the cause of the redshifts. We summarize the observed properties of these structures as follows:

- The downflows are mostly located in dark areas next to penumbral filaments, but some of them occur on the bright filament edges.
- The LOS velocities observed at the 70 % bisector level typically range from 150 to 300 m s^{-1}. Occasionally, stronger downflows exceeding 500 m s^{-1} are detected.
- During their lifetime, they can fragment, disappear, and reappear. They seem to follow the wiggle of the filaments they are associated with. We speculate that forces derived from horizontal pressure balance are somehow responsible for this behavior.
- The lateral downflows detected in the original Doppler maps are found at the same locations in straylight-compensated data, but with enhanced speeds. Thus, our results suggest that at least some of the downflows seen in data corrected for stray light are not mathematical artifacts.

As other authors, we observe upflows along penumbral filaments and downflows at their tails. The upflows return to the solar surface also at

the edges of the filaments, producing lateral downdrafts. This supports the existence of overturning convection in the penumbra **?**Scharmer et al. (2008).

Sánchez Almeida (2005) was the first to infer the existence of downflows all over the penumbra from the inversion of moderate resolution spectropolarimetric data. However, it is not clear to us that those downflows and ours represent the same phenomenon, given their very different spatial scales (optically thin versus optically thick) and speeds (tens of km s^{-1} versus a few hundred m s^{-1}).

3.7 Conclusions

For the first time, we report the ubiquitous presence of lateral downflows in penumbral filaments without correcting data for stray light and study their temporal evolution.

Lateral downflows are observed as short-lived, elongated, very narrow, and redshifted patches located in between blueshifted channels. These patches have an intermittent life and undergo mergings and fragmentations quite frequently. They follow the same wiggle as the flow channel. When comparing with continuum intensity filtergrams, lateral downflows are located on the sides or overlapping penumbral filaments.

We suggest an scenario where the lateral downflows are produced by elongated convection: adjacent convective cells (filaments) have a predominantly outward flow that returns to the solar surface at their tails, while overturning convection is found along the edges of the filaments. There, matter from neighbouring cells is strongly squeezed and allowed to fall down.

4

Dynamical and magnetic properties of lateral downflows

For most of history, Anonymous was a woman.
Virginia Woolf

4.1 Introduction

First evidences of lateral downflows (Scharmer et al., 2011; Joshi et al., 2011; Scharmer & Henriques, 2012) encouraged the study of their physical characterization. Thus, Ruiz Cobo & Asensio Ramos (2013) and Scharmer et al. (2013) found reversed polarity magnetic flux and lateral downflows at the borders of penumbral filaments using Hinode/SP and SST/CRISP data, respectively. Tiwari et al. (2013) described physical properties of a *standard* filament using Hinode/SP observations. However, as mentioned in Section 4.1, using deconvolved data (Scharmer et al., 2011; Joshi et al., 2011; Scharmer & Henriques, 2012; Ruiz Cobo & Asensio Ramos, 2013; Scharmer et al., 2013), the sunspots location over the solar disk, and the spectral lines selected to carry out these studies have arised some doubts about the reliability of such results.

Here, after reporting the detection and the temporal behavior of the lateral downflows (see Chapter 3), we physically characterize in detail their dynamical and magnetic properties. This study enables us to identify which are the ingredients needed to observe lateral downflows. Finally, we have interpreted our results using theoretical models and compared them with recent simulations.

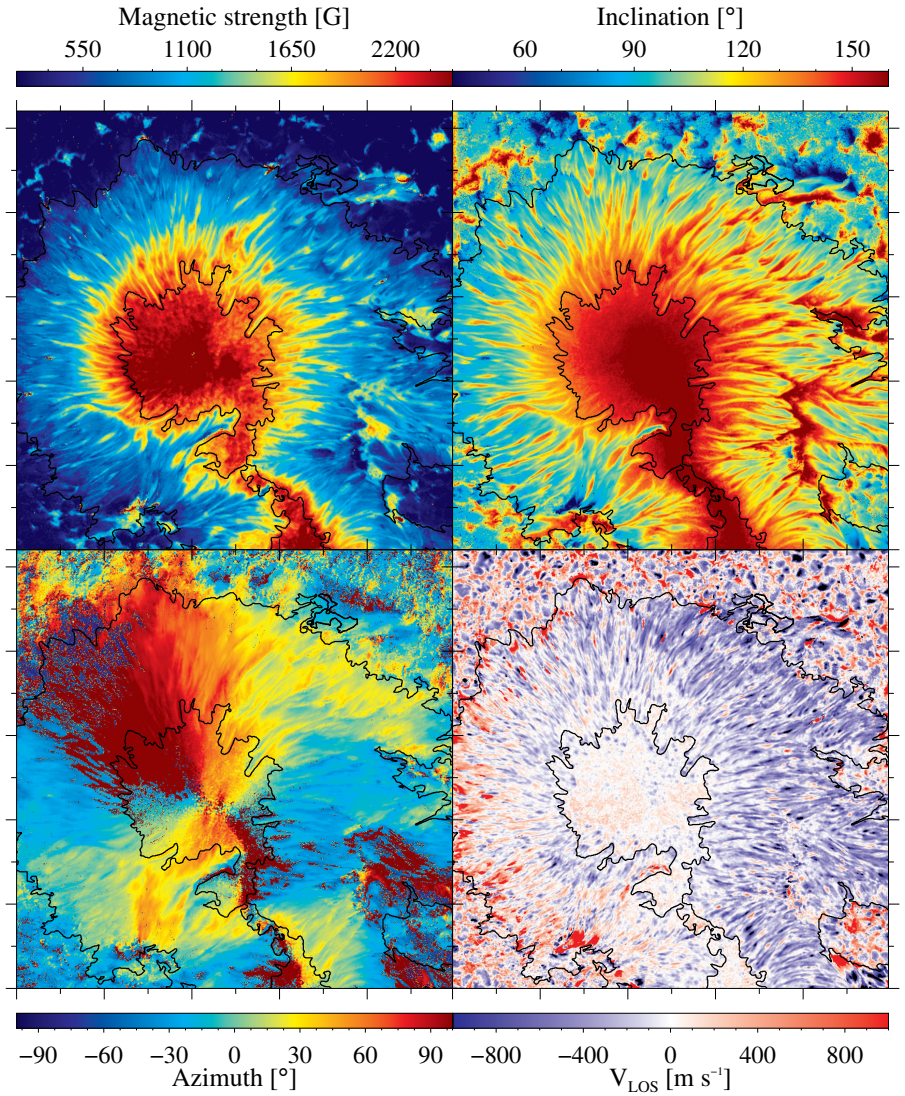

FIGURE 4.1:— Results obtained from the inversion. The corresponding snapshot was acquired at 09:26:00 UT. Each major tickmark represents 10″.

4.2 Stokes profiles and magnetic field vector

In order to obtain information about the magnetic field in lateral downflows, we performed an inversion of the observed Stokes profiles with the SIR code (Ruiz Cobo & del Toro Iniesta, 1992). We used the parallel implementation of Thonhofer et al. (2015). The inversions were carried out considering one node for magnetic field strength, inclination, azimuth and LOS velocity, and three nodes for temperature. Macroturbulence, microturbulence and straylight were set to zero. Figure 4.1 shows maps of the magnetic field

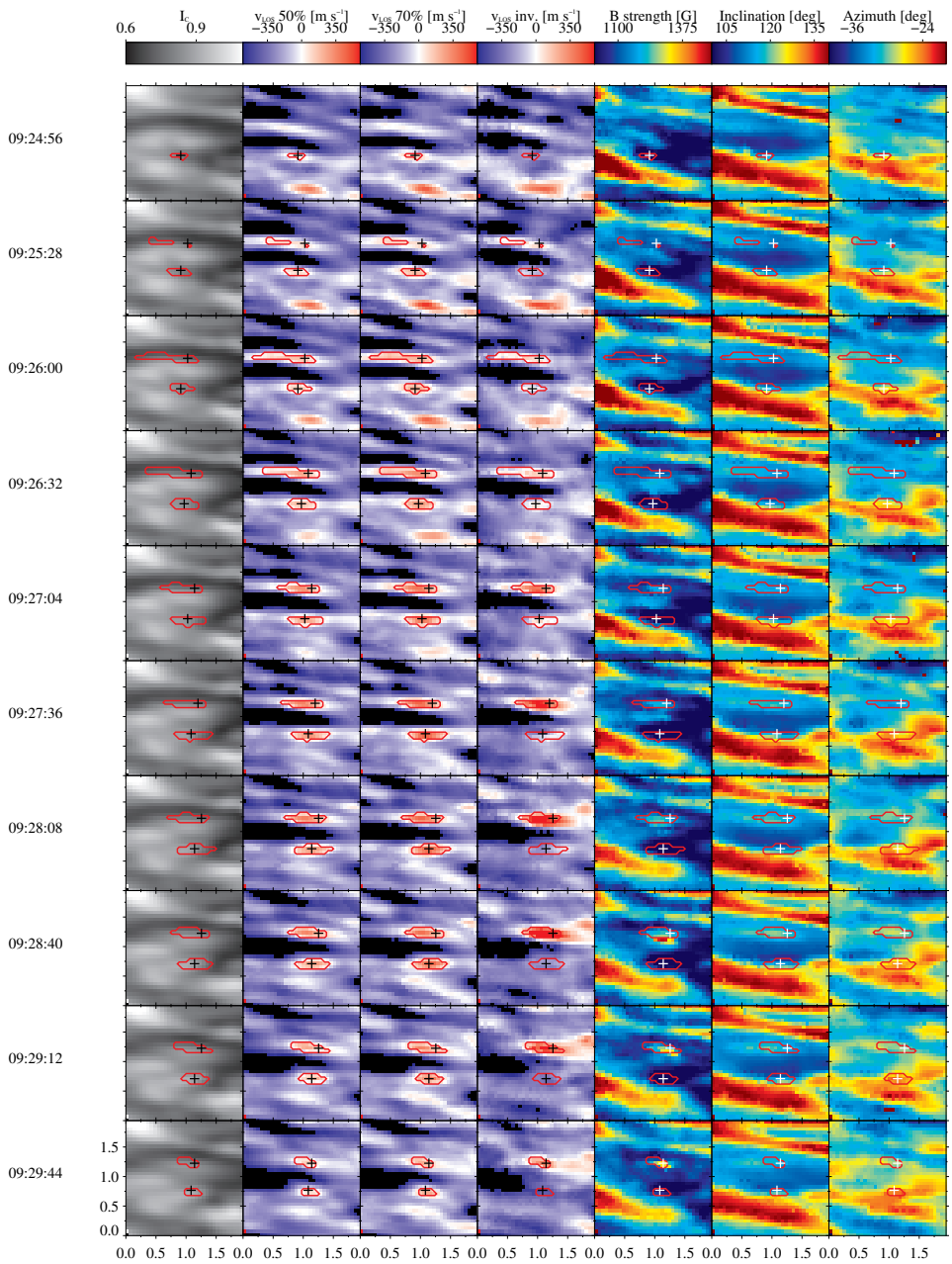

FIGURE 4.2:— Velocity and magnetic properties of lateral downflows (case 3). From left to right: continuum intensity filtergrams compensated for a stray light contamination of 40 %, LOS velocity at the 50 and 70 % bisector levels, LOS velocity, magnetic field strength and inclination obtained from the inversion. Red contours outline pixels where LOS velocity at the 70 % intensity level is greater than 100 m s^{-1}. Plus symbols mark the pixels represented in Figures 4.4-4.5. The UT time of each frame is shown in the leftmost column. Axes are labeled in arcsec.

strength, inclination, azimuth and LOS velocity inferred from this inversion.

Figure 4.2 shows consecutive snapshots of the continuum intensity compensated for a straylight contamination of 40 %, the LOS velocity at the 50 and 70 % bisector levels, the LOS velocity from the inversion[1], the magnetic field strength and the inclination inferred from the inversion for the duration of the downflows in Figure 3.11.

In Figure 4.2 we can see clear differences between the magnetic parameters of the central upflow channel and the lateral downflows. The LOS velocity inferred from the inversion is similar to that computed from the bisector technique, although the former tends to be more blueshifted. In spite of that, the upper lateral downflow reaches a velocity of about 800 m s^{-1} according to the inversion, which doubles the bisector velocities (around 400 m s^{-1}). This is due to the fact that we assumed a height independent velocity in the inversion. Therefore, physical information from different atmospheric layers are mixed. Both lateral downflows have a similar duration according to the second and third columns ($\sim$10 frames). In the fourth column the lower one has a shorter duration (4 frames) with respect to the upper one (10 frames).

The magnetic field strength of the flow channel remains constant at about 1150 G, reaching $\sim$1200 G where the LOS velocity is more blueshifted. The lateral downflows show two behaviors. The magnetic field strength of the lower lateral downflow ranges from 900 to 1000 G, i. e., it is $\sim$200 G weaker than the flow channel. In the upper lateral downflow, it starts at 1000 G and progressively grows. In fact, between 09:26:00 and 09:28:08 UT, the more redshifted region harbors the stronger magnetic field strength ($\sim$1200 G), which is similar to that of the flow channel. At 09:28:40 and 09:29:12 UT, the magnetic field strength increase extends to the interface between the lateral downflow and the blueshifted channel, where values of around 1500 G appear. Finally, in the last panel the LOS velocity of the lower lateral downflow is of order 250 m s^{-1} according to the inversion, and the magnetic field strength is $\sim$1300 G, i. e., 200 G stronger than that of the flow channel.

Regarding the magnetic field inclination, both lateral downflows have the same polarity as the sunspot. During the entire sequence, the blueshifted channel shows an inclination of about 105°, i. e., 15° away from being completely horizontal. The inclination of the lateral downflows are similar but $\sim$10° more vertical than the flow channel. The most notable difference between both lateral downflows is the existence of a few pixels that are more vertical in the upper patch (up to 125°).

Finally, the magnetic field azimuth of the blueshifted channel is roughly constant along the entire sequence (around −30°). The lower lateral downflow has an azimuth of about −25°, meanwhile the upper one is approximately −35°. These values are not very different from one another but they may

[1]The LOS velocity maps obtained from the inversions have been filtered for subsonic oscillations and calibrated as those using bisectors.

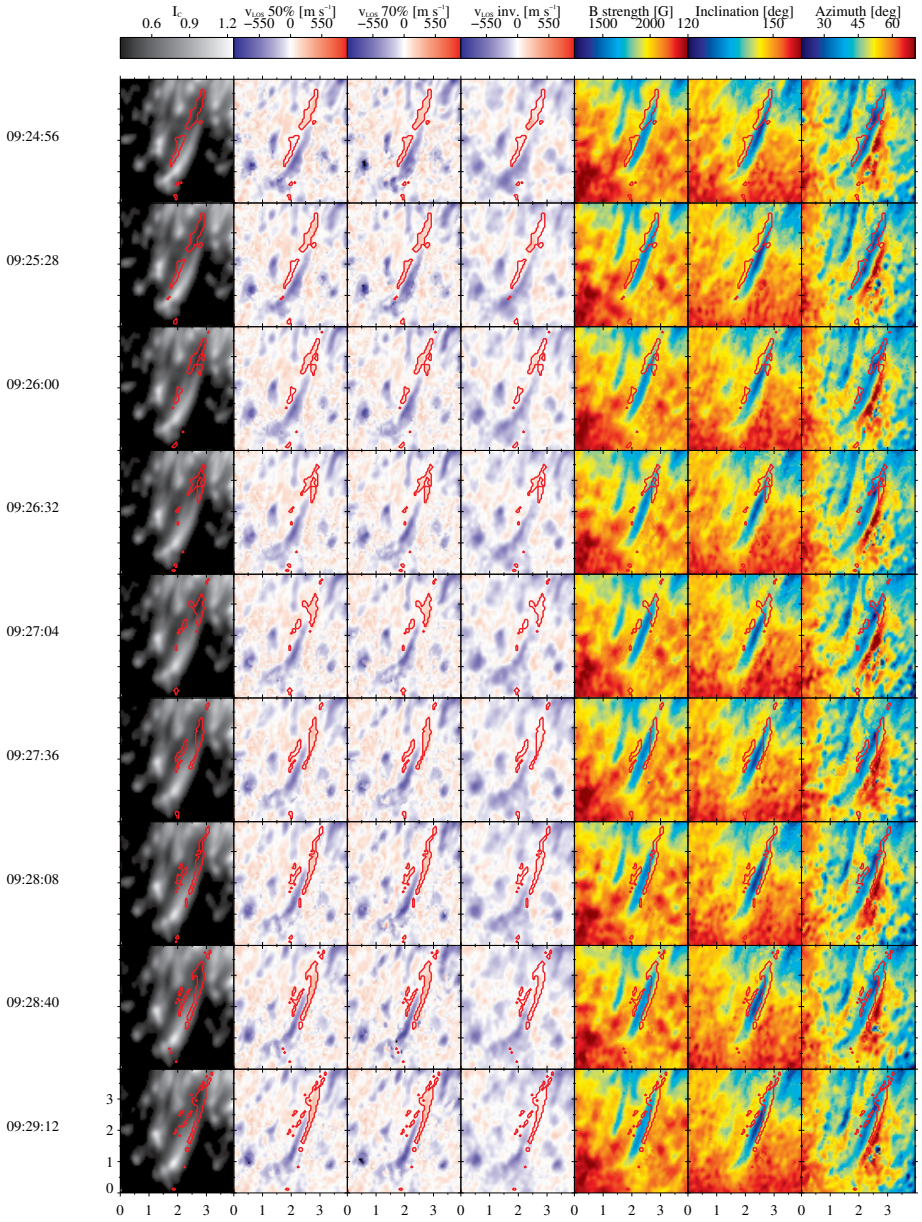

FIGURE 4.3:— Velocity and magnetic properties of lateral downflows (case 1). The layout is the same as in Figure 4.2.

suggest field lines corresponding to each lateral downflow are azimuthally deviated and guided away from the flow channel.

The aspects described in Figure 4.2 are in agreement with the global view of the physical parameters inferred from the inversion shown in Figure 4.1, except in the case of the magnetic field strength (specifically, in the

inner penumbra). In order to illustrate this discrepancy, Figure 4.3 examines the lateral downflow of case 1 during nine consecutive snapshots. The LOS velocity, magnetic field inclination, and azimuth in Figure 4.3 resemble those described previously in Figure 4.2. However, in Figure 4.2, the magnetic field strength of the center of the blueshifted channel is about 1000 G and increases toward its edges, reaching about 1800 G in the lateral downflows. As Figure 4.1, this is an aspect shared with filaments located in or next to the inner penumbra, which are the less cluttered regions.

Although some properties of the lateral downflows have been obtained from the inversion, the Stokes profiles might contain more information that the inversion is unable to retrieve (mainly, because the inversion setting). Then, we are going to examine the Stokes profiles of some pixels located within the lateral downflows. In Figure 4.4, we display the four Stokes profiles emerging from the center of the lowermost lateral downflow marked with a contour in Figure 3.11, as a function of time. Both linear and circular polarization are clearly seen. There is a noticeable asymmetry of Stokes I producing redshifts (the vertical dashed lines indicate the rest position of the line). Redshifts grow with time, reach a maximum, and fade.

The linear polarization spectra do not show features worth of mention, except perhaps their amplitude asymmetries. The circular polarization profiles have positive area asymmetries, with the blue lobe more extended than the red one (the exact values are shown next to the Stokes V profiles). In other patches we observe negative area asymmetries. This indicates the existence of velocity gradients along the LOS, possibly coupled with magnetic field gradients, which is consistent with the information provided by the line bisectors. Other than that, the Stokes V profiles emerging from the redshifted patch have the same sign as in the umbra. Thus, the magnetic field vector does not appear to undergo a polarity reversal there. However, toward the end of the sequence, at 09:29:12 and 09:29:44 UT, the Stokes V spectra exhibit a weak third lobe in the red line wing, close to the continuum. This additional third lobe (marked with arrows) seems to be strongly redshifted and of opposite polarity compared with the main Stokes V lobes. Similar signals are observed in many pixels of the redshifted patch at those times. They occur when the downflowing velocity is decreasing (as seen in the intensity profile), but when the asymmetry of Stokes I is maximum, with a very extended wing toward the red continuum.

Three-lobed profiles have previously been observed in the outer penumbra —both near the sunspot neutral line (Sánchez Almeida & Lites, 1992; Schlichenmaier & Collados, 2002b) and far from it (e.g., Westendorp Plaza et al., 2001; Bellot Rubio et al., 2002)—, at the position of Evershed flows returning to the solar surface (e.g., Ichimoto et al., 2007a; Franz & Schlichenmaier, 2013), and at the edges of penumbral filaments (Ruiz Cobo & Asensio Ramos, 2013). The mere detection of these profiles indicate the coexistence of fields of opposite polarity along the LOS. The opposite pola-

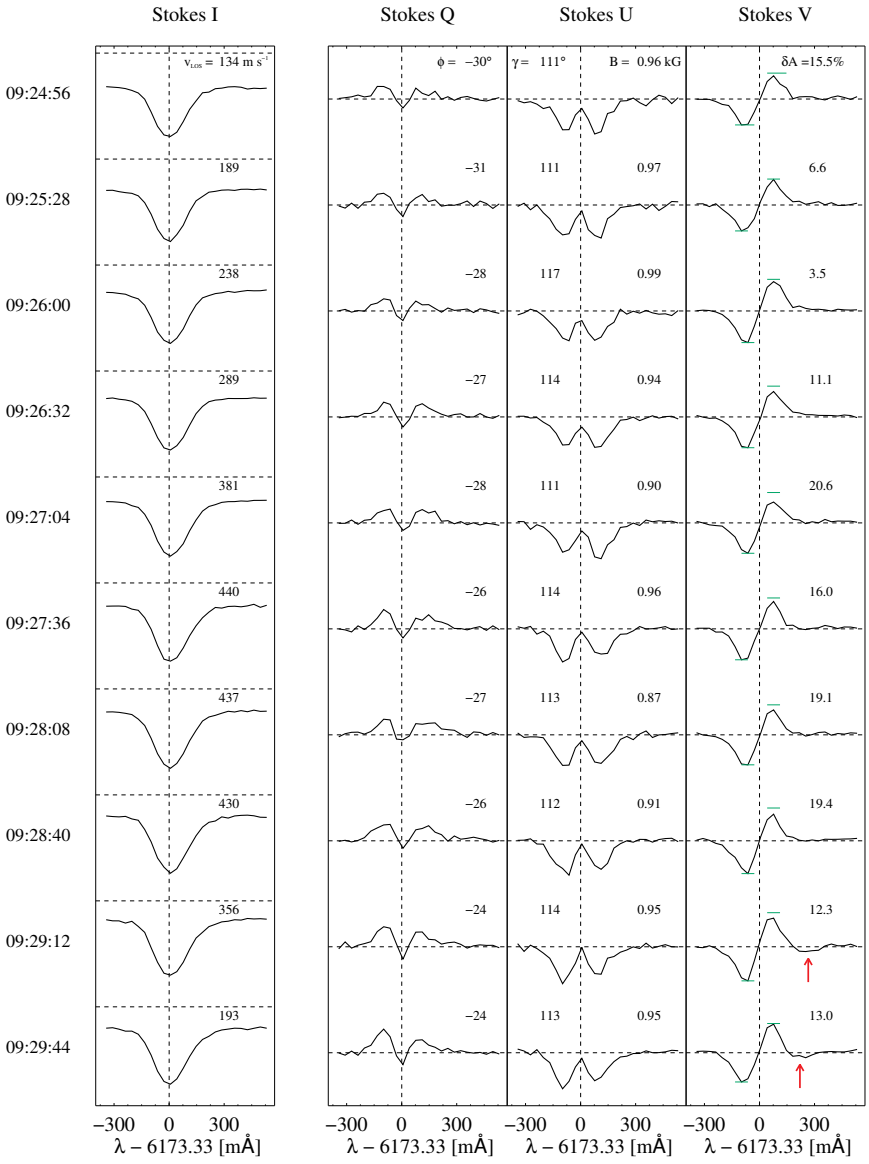

FIGURE 4.4:— Temporal evolution of the Stokes profiles emerging from the center of the lowermost lateral downflow in Figure 4.2. The horizontal lines in the intensity panels represent the continuum of the average quiet Sun profile, while those in the other columns indicate zero polarization signal. The Doppler velocity at the 70 % bisector level, the magnetic azimuth, the magnetic field inclination, and the Stokes V area asymmetry in percent are indicated in the upper positions of the subpanels corresponding to the same time stop. The magnetic parameters have been determined from an inversion of the observed Stokes profiles.

rities do not need to be cospatial (i. e., to lie side by side), as they can also be located at different heights in the atmosphere. Whether the third lobe is produced by dragging of the spot field lines by the downflows (as suggested

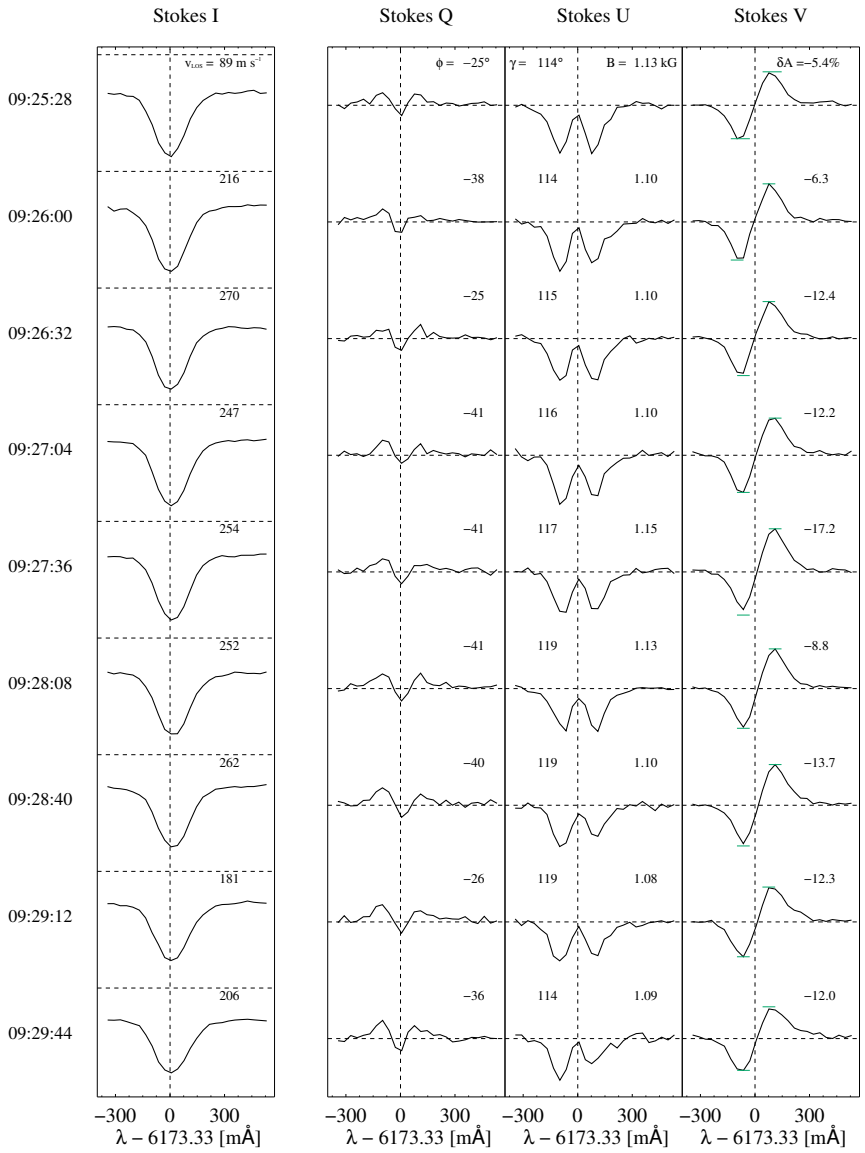

FIGURE 4.5:— Temporal evolution of the Stokes profiles emerging from the tail of the uppermost lateral downflow in Figure 4.2. The layout is the same as in Figure 4.4.

by Rempel, 2012) or by a stable field pointing to the solar surface remains to be investigated.

Figure 4.5 shows the temporal evolution of the Stokes profiles observed at the tail of the uppermost lateral downflow in Figure 4.2. The spectral signatures are similar to those found previously, but the line shifts are smaller here.

Once again, the circular polarization profiles show interesting features. The red lobes of the Stokes V profiles are more extended than the blue lobes

and their amplitudes are greater, unlike those from the other downflowing patch. Besides, there are no additional lobes in the Stokes V spectra. Such a diversity may indicate the existence of different physical gradients along the LOS in different pixels.

The values inferred for the flow channel are different from those of the lateral downflows. This is in agreement with previous analyses that obtained relative differences in magnetic field inclination of order 10-20° (Scharmer et al., 2013) and even with the latest 3D MHD simulations (Rempel, 2012).

4.3 General properties of lateral downflows in penumbral filaments

We have determined the properties of the lateral downflows through repeated application of the YAFTA[2] feature tracking code (Welsch & Longcope, 2003) to an area inside the disk-center penumbral region zoomed in Figure 3.6. We selected this region because it is parallel to the symmetry line and contains many lateral downflows.

A lateral downflow detected in a Dopplergram is called a patch. A set of patches that are associated with the same lateral downflow, which is moving coherently with time, is called a structure and labelled as an unique element. Thus, structures contain several patches, from their birth until their disappearance. Structures can undergo mergings or fragmentations during their lifetimes.

The YAFTA code consists of a suite of IDL programs that identify features in an image and matches them between consecutive images. These two tasks make it very useful for analyzing temporal sequences. YAFTA can use two different methods of identifying and labelling features:

- *Clumping method* (Parnell, 2002): It identifies contiguous, same-sign pixels above a certain threshold as features.
- *Downhill method* (Welsch & Longcope, 2003): It searches the pixels harbouring the maximum signals and associates surrounding, same-sign pixels above a threshold with a feature.

If a redshifted patch has two maxima, the clumping method will identify it as a single feature, while the downhill algorithm will take it as two different features. We have used the clumping method because we define patches as sets of contiguous, same-sign pixels above a threshold value. The criteria for identifying lateral downflow were as follow:

- Each patch must be formed by five or more pixels. Those that do not satisfy the minimum size criterion are discarded to avoid false detections due to noise or other problems.

[2]Yet Another Feature Tracking Algorithm

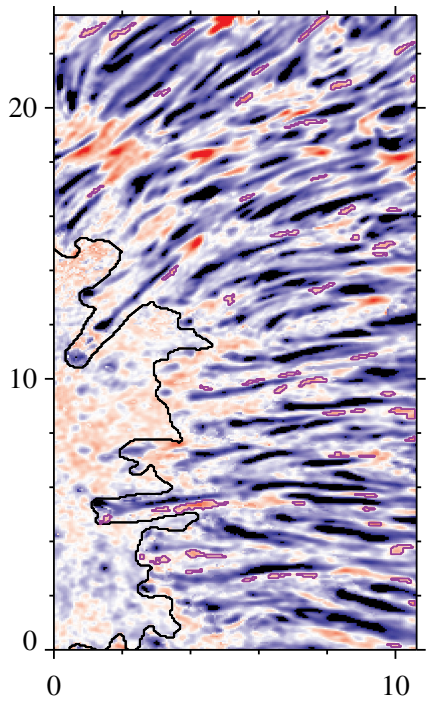

FIGURE 4.6:— Purple contours outline the patches detected by YAFTA at 09:26:00 UT. They are overplotted on the corresponding Dopplergram at the 70 % intensity level. The LOS velocities are scaled as in Figure 3.6. The black contour shows the umbra-penumbra border. Axes are labelled in arcseconds.

- The LOS velocity must range between 50 and 600 m s^{-1}. The upper limit for the velocity excludes redshifts at the tail of penumbral filaments that correspond to returning Evershed flows. Although the uncertainty of our velocity reference is 110 m s^{-1} (see Subsection 3.2.1), the lower limit used here is 50 m s^{-1}. Sometimes, pixels in between patches have LOS velocities smaller than 110 m s^{-1}. So, in order to avoid false fragmentations we have used a lower threshold.

- After experimenting with different thresholds, the YAFTA identifications were further refined by retaining only those structures visible in at least four consecutive frames (to avoid false detections due to noise) or coming from the fragmentation of another structure.

The features detected through application of these criteria were checked manually to ensure that they represent genuine lateral downflows. Figure 4.6 shows an example of the patches detected in a particular Dopplergram. As can be seen, weak redshifts that are unclear are not considered in this study. All in all, 754 structures (5328 patches) were identified and tracked in the Dopplergram time sequence.

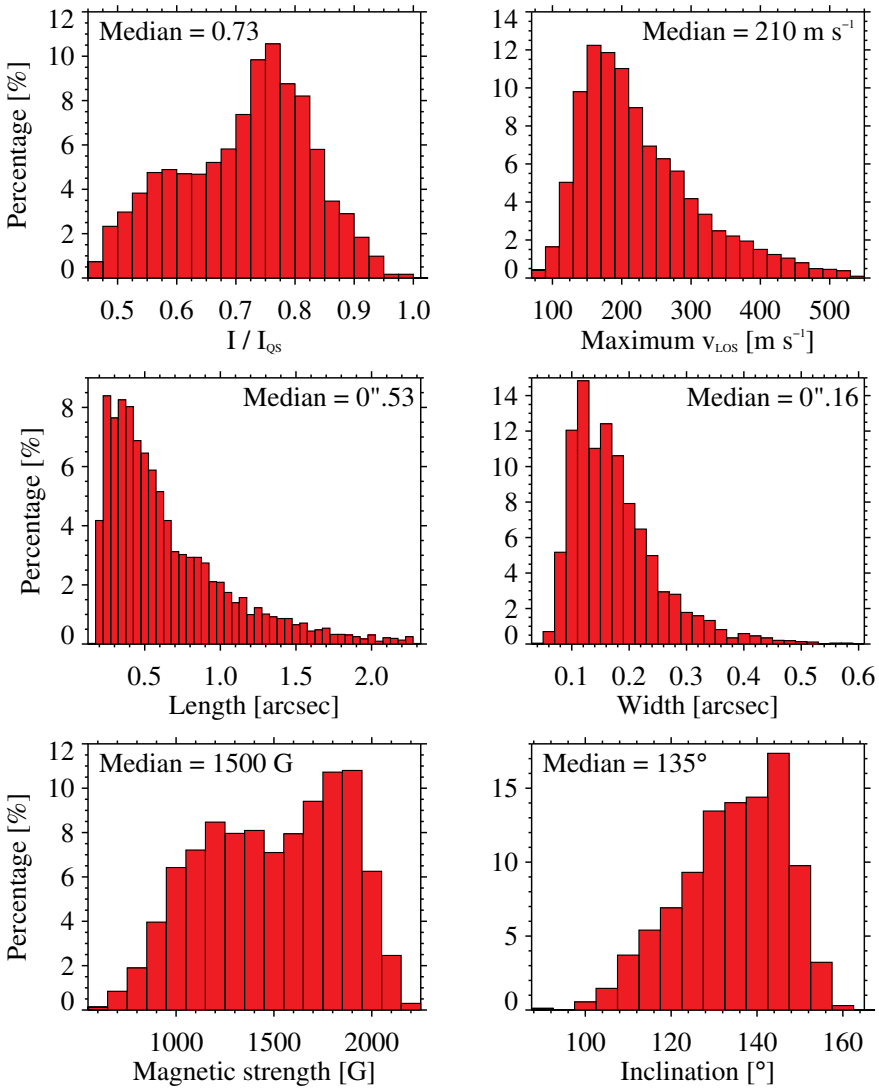

FIGURE 4.7:— Histograms of continuum intensity, maximum LOS velocity, length, width, magnetic field strength, and inclination of the redshifted patches observed at the edges of penumbral filaments, considered individually. The median of the distribution is indicated in the upper corner of the panels.

Figure 4.7 displays histograms of the continuum intensity, maximum LOS velocity, length, width, magnetic field strength, and inclination of the individual patches detected by YAFTA. The lateral downflows show a broad range of intensities, indicating that they appear both in dark regions next to the filaments and in the bright filament edges. The median value is 0.73 of the quiet Sun continuum intensity. Most patches have a maximum LOS velocity in the range 150-250 m s^{-1} with a median of 210 m s^{-1}. We have

fitted an ellipse to each patch to obtain its dimensions. The major axis of the ellipse corresponds to the length and has a median value of $0\farcs53$. The width is given by the minor axis, which varies between $\sim0\farcs1$ and $\sim0\farcs3$ with a median of $0\farcs16$. Therefore, the redshifted patches tend to be elongated and very narrow. The magnetic field strength of most patches ranges between 1000 and 2000 G with a median of 1500 G. All the patches included in the statistics have the same polarity as the sunspot, showing inclinations from $\sim$100 to 150° with a median of 135°.

Figure 4.8 summarizes the properties of the lateral downflows, considered as coherent structures that can be tracked in subsequent frames of the Dopplergram sequence. We show histograms of lifetimes, horizontal motions (proper motions), the ratios of maximum to initial intensities, LOS velocities and magnetic field strength, and differences between the maximum and the initial magnetic field inclination.

For the calculation of the lifetime we have considered only the structures that appear and disappear *in situ* (i.e., that do not undergo interactions) and those that appear *in situ* and fragment, but only until their first fragmentation. The fragments are excluded in order not to bias the statistics, since they usually have shorter lifetimes. For this reason it is appropiate to think of the lifetimes as detection times. Most of the lateral downflows are observed for 4-10 frames. The distribution decreases exponentially and the median value is 3.2 minutes (6 frames). Thus, they are short-lived features. This may be intrinsic to the physical mechanism driving the downflows or a consequence of our inability to identify structures when the LOS velocities become too small.

The second panel of Figure 4.8 shows the distribution of the mean horizontal speed of the downflowing structures. This parameter has been calculated using well-defined structures for which the direction of motion is clear. Positive (negative) values represent motions away from (to) the umbra. As can be seen, most patches move outward. The median horizontal speed is 85 m s^{-1}. About 75 % of the patches develop larger redshifts, stronger magnetic field and brighten during their evolution. The median ratios of maximum to initial intensities, LOS velocities and magnetic field strength are 1.22, 1.03 and 1.02, respectively, so the velocity increase is larger than the brightness and the magnetic strength increase. Finally, around 30 % of the patches has the same inclination during their life and the remainder becomes slightly more vertical ($\sim$14 % of them are more than 5° more vertical than at their birth). The median value of this difference is 1.30°.

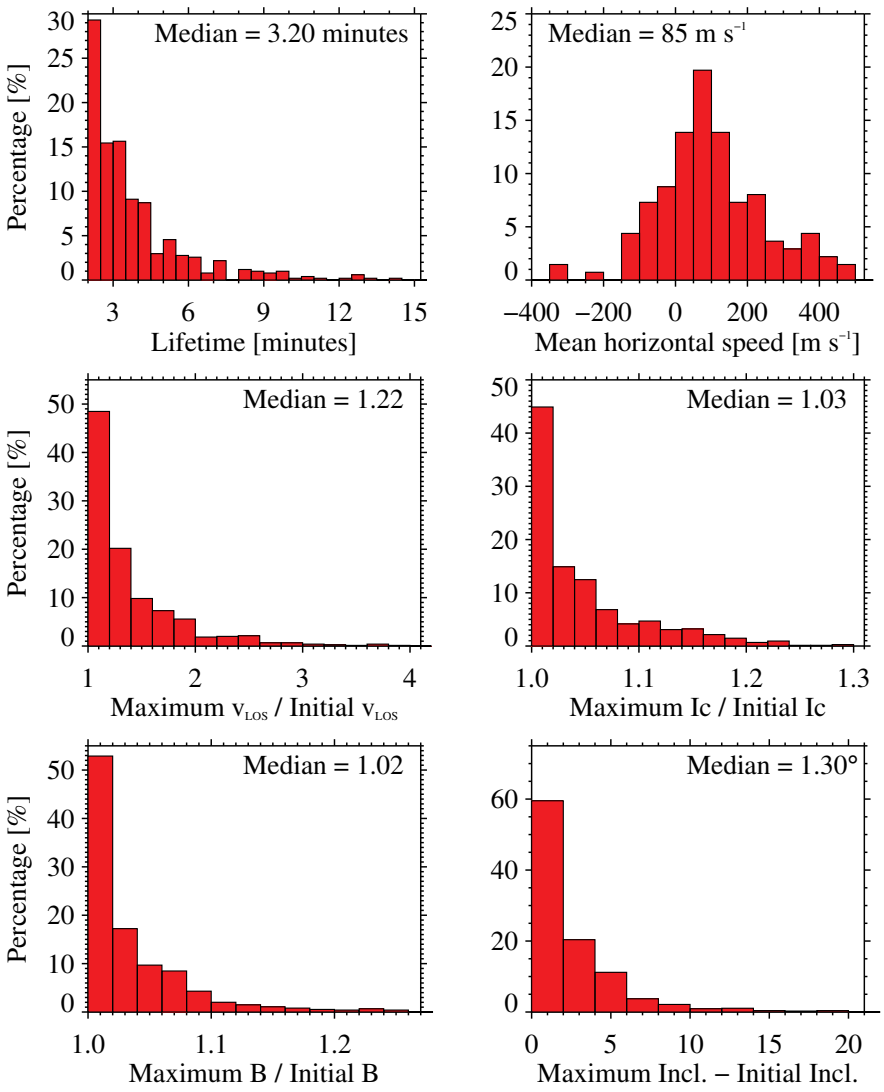

FIGURE 4.8:— Histograms of lifetime, mean horizontal speed, ratio of maximum to initial continuum intensity, ratio of maximum to initial LOS velocity, ratio of maximum to initial magnetic field strength, and difference between the maximum and the initial magnetic field inclination for the lateral downflows, considered as coherent structures that evolve from frame to frame. The median of the distribution is indicated in the upper corner of the panels.

4.4 Why is the detection of lateral downflows so challenging?

Sunspot penumbrae have been subject to intense scrutiny for years, using all observational techniques, from monochromatic imaging to Stokes spectropolarimetry, at moderate and high spatial resolution, and low and high

cadence. Yet the lateral downflows have consistently eluded detection (e.g., Jurcák et al., 2007; Franz & Schlichenmaier, 2009; Bellot Rubio et al., 2010; Franz, 2011). Having established their properties, we can now provide explanations as to how why their detection was so challenging.

The first problem is our inability to determine the three components of the velocity vector. Only the LOS component is accesible via spectroscopic measurements. Thus, in order to detect vertical motions unambiguously, it is necessary to observe sunspots as close as possible to the disk center, so that the LOS coincides with the normal to the local surface (Bharti et al., 2011). However, this kind of obervations are very scarce. Most measurements carried out so far correspond to spots away from the disk center, where the velocity field is dominated by the strong Evershed flow, effectively hiding the weak lateral downflows.

The second problem is that spectroscopy, and more so spectropolarimetry, is very demanding in terms of exposure time. The long exposures that are required generally mean lower spatial resolution because of stronger seeing degradation, unless the observations are made from space. The highest resolution measurements of sunspot penumbrae using a slit spectrograph were performed by Bellot Rubio et al. (2010) at the SST. Exposure times of 200 ms were needed and, despite the excellent seeing conditions, the achieved spatial resolution was not better than some $0\farcs2$. This is barely sufficient to detect the largest downflow patches, as the median width of these structures is only $0\farcs16$ (lateral downflows properties are calculated in Section 4.3). Lateral downflows are also out of reach for the Hinode spectropolarimeter, because of its resolution of about $0\farcs32$. This may explain why Franz & Schlichenmaier (2009) did not detect them in their careful analysis of sunspots at the disk center.

Of course, fingerprints of the weak lateral downflows must be present in the observed Stokes profiles even at moderate spatial resolution (e.g., the Doppler shifts they produce, their possible opposite polarities, etc.) but, being unresolved, separating them from the dominant signals of the strong Evershed flows is not easy −not even for complex Stokes inversions such as those performed by Bellot Rubio et al. (2003), Mathew et al. (2003), Bellot Rubio et al. (2004), Borrero et al. (2005) or Beck (2011). Recently, hints of the largest downflow patches may have been obtained by Franz & Schlichenmaier (2009) and Franz & Schlichenmaier (2013) using the Hinode spectropolarimeter. Assuming the penumbra to be a micro-structured magnetic atmosphere, however, Sánchez Almeida (2005) reported downflows and opposite magnetic polarities all across the penumbra from the inversion of spectropolarimetric measurements. These downflows were found to have velocities of up to 10 km s^{-1}.

The intermittent character of the lateral downflows, which often appear only on one side of the filaments, and for short periods of time (the median lifetime is 3.2 minutes, as can be found in Section 4.3), also imposes strong

limitations to slit instruments. The spectroscopic observations of Bellot Rubio et al. (2010), for example, sampled several penumbral filaments, but given the intermittency of the lateral downflows it was unlikely that just a single slit position could catch many instances of them, if any at all. Thus, in retrospect, the chances of success of those observations were low.

The key to detection is probably ultra-high spatial resolution. This is why imaging spectropolarimetric observations provided the first evidence of lateral downflows (Scharmer et al., 2011; Joshi et al., 2011). The measurements were subject to post-facto image restoration to reach the diffraction limit of the SST, which at $0\farcs13$ made it possible to resolve the smallest velocity structures ever. Still, corrections other than standard image reconstruction had to be applied to bring out the lateral flows. They were meant to compensate for substantial amounts of stray light and in practice involved strong deconvolutions of the data. For many observers, such corrections lowered the significance of the discovery.

Reaching ultra-high spatial resolution is not sufficient, however. One needs to subtract from the velocity measurements the oscillation pattern known to affect sunspot penumbrae. This pattern consists of large-scale velocity fluctuations with amplitudes of the order of 100 m s^{-1}, superposed onto the actual penumbral flow field. Not removing the oscillations may bias the velocities to the point of making some structures appear redshifted when in reality they do not harbor downward motions. Conversely, genuine lateral downflows can be effectively hidden by the oscillations during their blue excursions, since the amplitude of the latter is not much smaller than the LOS velocities of the former.

To subtract the oscillation pattern, one needs to secure time sequence under stable seeing conditions. This is extremely challenging. All imaging spectroscopic measurements presented to date are based on single snapshots and therefore thet are affected by oscillations in unknown ways, which casts doubts on the reliability of the reported lateral downflows. To illustrate the importance of this correction, Figure 4.9 shows the typical velocity patterns created by oscillations in our sunspot. They correspond to phases where the center-side penumbra is offset to the blue by an average of -92 m s^{-1} (top panel) and to the red by 88 m s^{-1} (bottom panel). These are the offsets that could not be subtracted in previous investigations because of the lack of temporal information.

The choice of spectral line is also relevant, although probably not of prime importance. The discovery paper used the extremely weak C I 538 nm line (Scharmer et al., 2011), which is thought to be one of the deepest-forming lines in the visible but nearly disappears in cool structures like the penumbral background that surrounds the flow channels. In addition, C I 538 nm is affected by molecular blends and cannot be used to set up a reliable velocity reference (Uitenbroek et al., 2012). Joshi et al. (2011) employed the traditional Fe I 630 nm lines, which do not show these problems

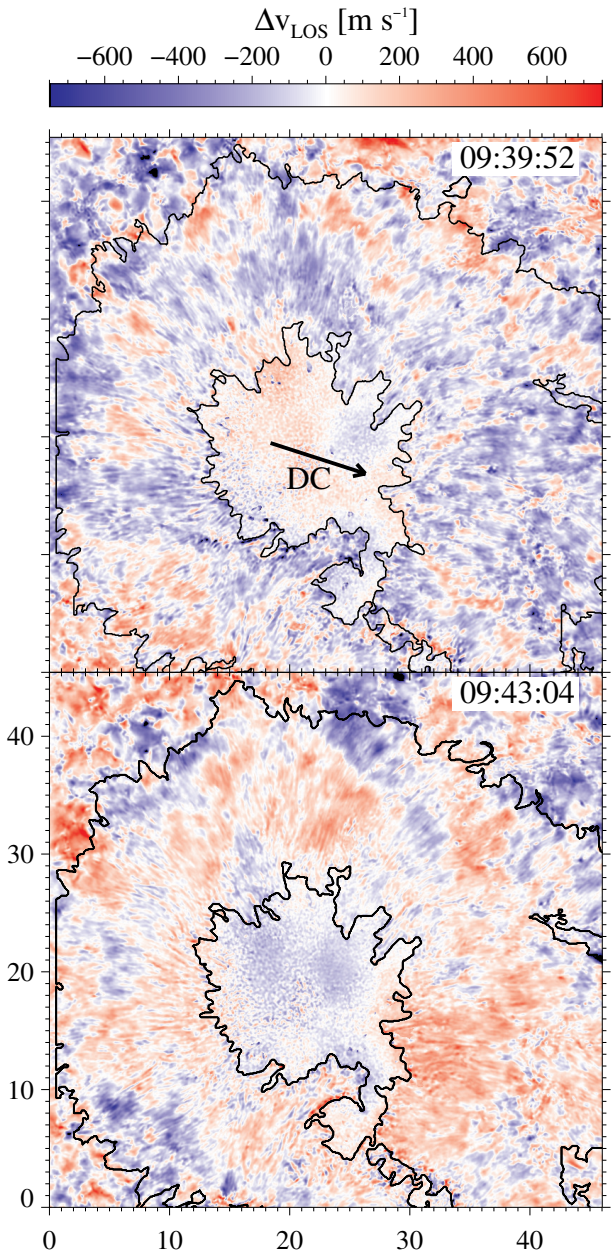

FIGURE 4.9:— Amplitudes of the 5-minute oscillation in two frames of our Dopplergram time sequence, corresponding to phases in which the center-side penumbra is offset to the blue by 92 m s^{-1} (top) and to the red by 88 m s^{-1} (bottom). Axes are labelled in arcsecs. The arrow marks the direction to the disk center.

in the penumbra but have two O_2 telluric lines distorting their red wings. This is precisely the most important region of the lines for observing down-

ward motions (redshifts), which again may raise doubts on the reliability of the detection. Other lines used in spectroscopic studies include Fe I 709 nm. This transition is narrow and therefore very sensitive to velocities (Cabrera Solana et al., 2005), but a CN blend at 709.069 nm distorts its red wing. The Fe I 617.3 nm line we have observed is also very narrow, with the additional advantage of its perfectly flat and clean red continuum (see Figure 2.5 in Section 2.4). However, it seems to be affected by an Eu II 617.3 nm blend and two other molecular lines in very cold umbrae (Norton et al., 2006).

On top of this all, we found that a precise correction of subtle instrumental effects is mandatory to unveil the existence of lateral downflows, given the extremely weak Doppler signals they generate. Having imaging spectropolarimetric observations at the diffraction limit and excellent seeing for long periods of time does not help much unless the etalon cavity errors are carefully corrected for. As mentioned in Section 2.5.1 they produce an orange peel pattern in the velocity maps, with amplitudes that easily exceed those of the lateral downflows themselves. The method we have used to remove the cavity errors produces velocity maps of unprecedented quality and remarkable smoothness.

In summary, the detection of lateral downflows is challenged by a large number of factors that conspire together to hide them in most but the best observations. A good knowledge of their properties, as established here, will hopefully help design new strategies to further study these features and their temporal evolution.

4.5 Comparison with theoretical models

The lateral downflows we have observed are compatible with several models of sunspot penumbrae. They are briefly described in the following.

Danielson (1961) suggested that penumbral filaments represent convective rolls (cells) lying next to each other, with their long dimension being parallel to the horizontal component of the magnetic field. As explained in Section 1.4.2, two of these rolls would form a filament as they turn in opposite directions, creating a bright upflow in the center and two downflows on the external sides of the rolls. These downflows could be the ones shown in this thesis. Thus, this model is still valid, despite Rempel (2011b) ruled out this scenario on the basis of a bad match with observation (mainly because at that time there was no evidence of lateral downflows at the filament edges).

Lateral downflows may also happen in penumbral flux tubes. Borrero (2007) derived the thermodynamic and magnetic configuration of flux tubes in perfect mechanical equilibrium with the surroundings. He found that flux tubes are stable structures if the magnetic field is mainly aligned with the tube axis and shows a small azimuthal component, i. e., if the field is

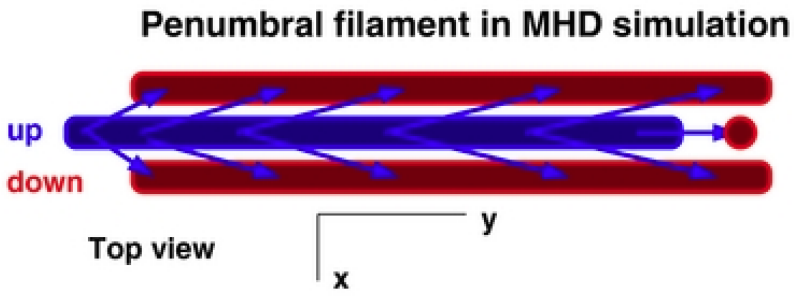

FIGURE 4.10:— Top view of the flow structure of a penumbral filament resulting from the 3D MHD simulations performed by Rempel (2012). The x and y axes denote the azimuthal and radial direction in the plane of the filament. Blue and red colors indicate gas moving toward or away from us, respectively. From Rempel (2012).

slightly twisted. In the plane perpendicular to the tube axis, the magnetic field topology resembles two convective rolls through which gas can flow aligned with the magnetic field. The flow would be mainly radial but would show an upward component at the center of the tube and downflows on the sides. Actually, this flow pattern is the one to be expected, since force balance requires the central part of the tube to be hotter than the external part, which would naturally trigger convective motions as described above. The model by Borrero (2007) produces penumbral filaments with central dark cores and is consistent with all sunspot magnetic field measurements performed to date.

Finally, the lateral downflows may also be the result of overturning convection in the penumbra, as first proposed by Scharmer et al. (2008). According to this model, penumbral filaments are elongated convective cells with two distinct velocity components (see Section 1.4.2). A schematic view is shown in Figure 4.10. Upflows emerge into the surface at the filament head and progressively get more inclined along the filaments until they sink at their tails. At the same time, the upward flows turn over laterally, becoming downdrafts at the filament edges. The resulting convective pattern is very similar to that observed in quiet Sun granules, except for the existence of a preferred direction: the one defined by the sunspot magnetic field.

From a pure kinematic point of view, our observations cannot rule out any of these models. Additional criteria need to be invoked to discern between the different scenarios.

Independently of the driver of the lateral downflows, the three models predict the existence of a flow connecting the central upflows with them. Such an azimuthal flow might be responsible for the so-called twisting motions. Therefore, the next step is to study them by spectroscopic means. This analysis could settle the problem of the gas flow in penumbral filaments at photospheric levels.

4.6 Comparison with 3D MHD simulations

The existence of overturning convection in the penumbra seems to be backed up by the latest 3D numerical simulations (e.g., Rempel et al., 2009a; Rempel, 2011a,b,c, 2012).

In this Section, we compare our results with those obtained from simulations of (Rempel, 2012). They model a sunspot in a 49.152 x 49.152 x 6.144 Mm domain, where the z axis refers to the vertical direction. The spatial resolution is 12 x 12 x 8 km. Details about the setup of the runs are described in Rempel (2012). This is a grey simulation and be downloaded from download.hao.ucar.edu/pub/rempel/sunspot_models/FineStructure

Figure 4.11 shows the temperature, vertical velocity, magnetic field strength, and inclination of the model sunspot at $\tau = 1$ and 0.1, respectively. Temperature maps display penumbral filaments that are similar to observed ones. As expected, the temperature, vertical velocity and magnetic field strength at $\tau = 1$ are higher than these at 0.1. In addition, magnetic field inclination at $\tau = 1$ shows higher values than $\tau = 0.1$. Indeed, there are more positions where magnetic polarity is reversed with respect to the sunspot one (inclination $\geq 90°$), i. e., pointing to the solar surface. Thus, inclination maps indicate a polarity reversal happening between the two atmospheric layers.

A close up of the temperature, the vertical velocity, the magnetic field strength, and the inclination of the filament in the rectangle of Figure 4.11 is displayed in Figure 4.12. This filament is protruding into the umbra and seems to be isolated from other filaments, thus the identification of its lateral downflows is easier.

Similarly to Figure 4.11, Figure 4.12 shows a filament with higher temperature in $\tau = 1$ than in 0.1. In both cases, the head of the filament is hotter than its body and the lateral edges are even darker. No dark core is clearly seen in this filament. At $\tau = 1$, the head of the filament is associated with a strong upflow (~ -2 km s^{-1}). This upflow becomes smoother in the body of the filament. At the same time, there are two lateral downflows on each side of the filament. The upper lateral downflow has a length comparable to the filament (around $2''$) and harbors a vertical velocity of about 1.5 km s^{-1}, reaching up to 2 km s^{-1} at some places. By contrast, the lower lateral downflow is shorter but it still covers almost all the filament. Its has smaller vertical velocities of about 600 m s^{-1}. At $\tau = 0.1$, the head of the filament has a smaller vertical velocity, of around -1 km s^{-1}. The velocity difference between the head and the body of the flow channel is smoother. Two lateral downflows appear on both sides of the blueshifted channel also here. The vertical velocity of the upper lateral downflow is 800 m s^{-1} (1.5 km s^{-1} in some regions), while those of the lower one are $\sim$500 m s^{-1}. The upper lateral downflow still has a length comparable to that of the filament, like in deeper down. However, there are some positions in the lower downflow where the vertical velocity has faded, leading to a

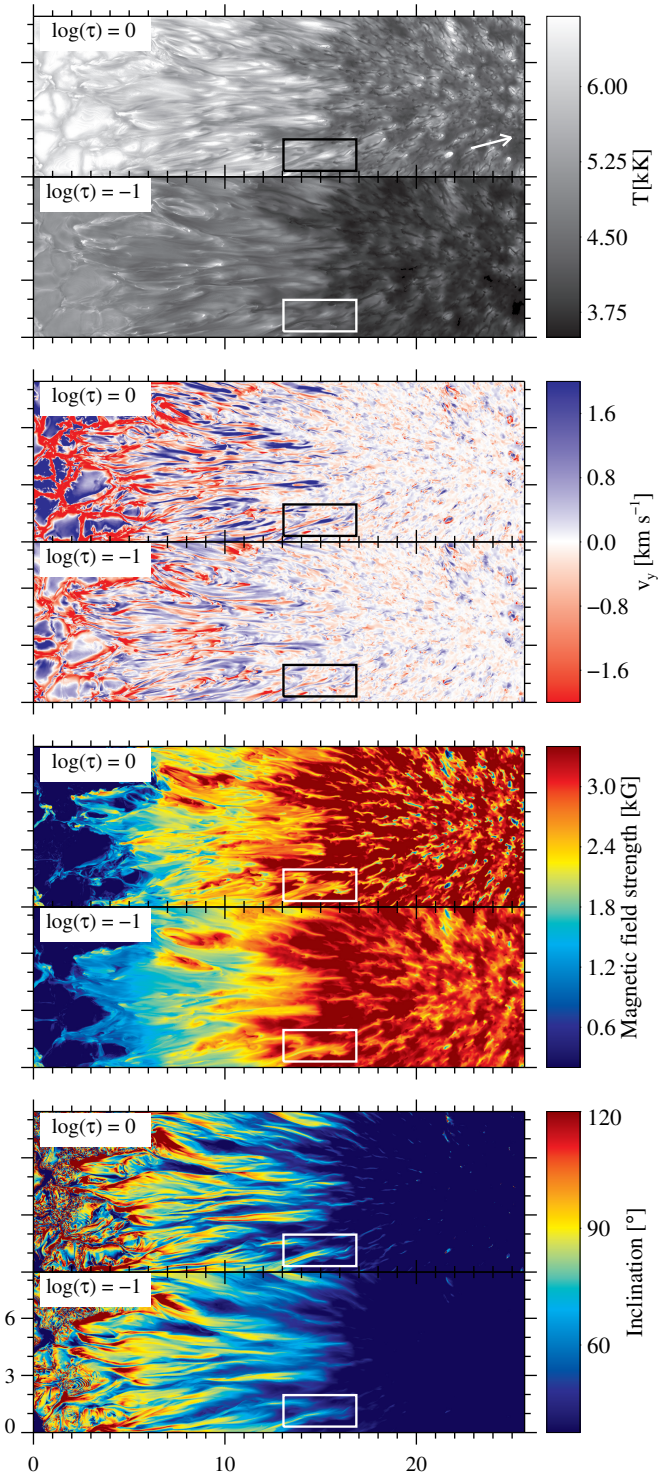

FIGURE 4.11:— Temperature, vertical component of the velocity field, magnetic field strength and inclination maps are shown from top to bottom at $\tau = 1$ and 0.1 (uppermost and lowermost row, respectively). These maps are derived from 3D MHD simulations of an entire sunspot (Rempel, 2012). The rectangle displayed in each panel encloses the FOV shown in Figure 4.12. The white arrow located in the upper panel points to the center of the umbra. Axes are labelled in arcsecs.

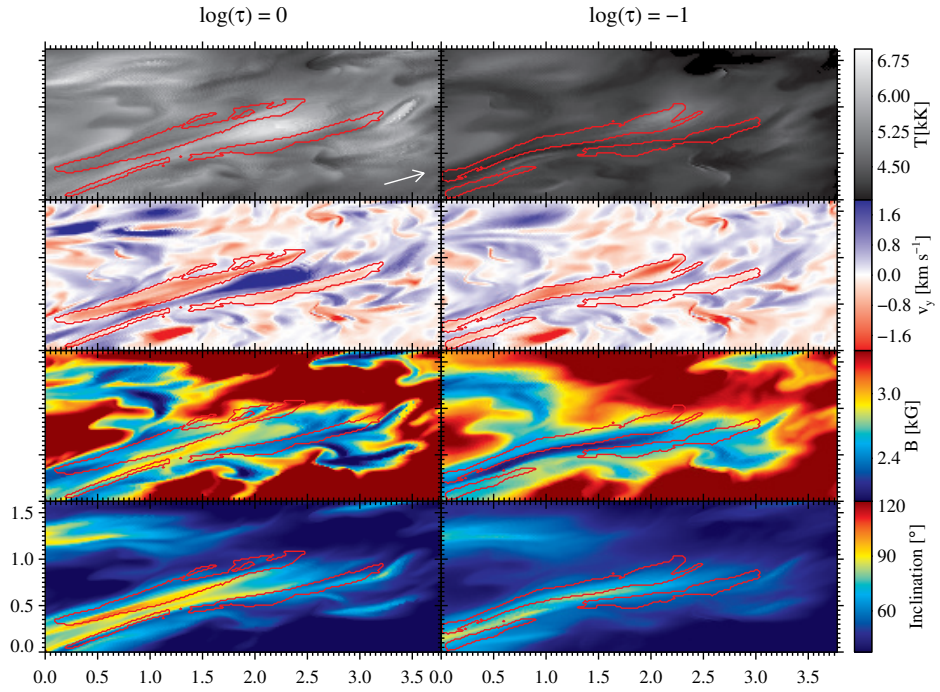

FIGURE 4.12:— Temperature, vertical velocity, magnetic field strength, and magnetic field inclination maps are shown from top to bottom inside the rectangle of Figure 4.11. Red contours outline regions with vertical velocities greater than 100 m s^{-1}. The white arrow points out the center of the umbra. Axes are labelled in arcsec.

patchy appearance.

As seen on the left column of Figure 4.12, the filament has a magnetic field strength of about 2400 G at the head and 2800 G in the body of the filament. The lateral downflows harbor a similar magnetic field strength to that at the head of the filament, although there are positions where it gets stronger (∼2600 G). In $\tau = 0.1$, there is a decrease of the magnetic field strength of the filament. Indeed, the magnetic field strength of the center of the filament is about 2000 G and the transition to the edges is smoother, where is ∼2500 G (reaching up to 2700 G in some places).

Finally, the magnetic field inclination at the head of the filament is around 50- 60°, indicating rather inclined magnetic field lines both at $\tau = 1$ and $\tau = 0.1$. As expected, the magnetic field becomes even more horizontal in the body of the filament. In the Figure, the polarity reversal occurring at some positions of the lateral downflows is clearly observed when comparing both layers: the inclination ranges from 70 to 105° in $\tau = 1$, and between 70 and 80° in 0.1. Besides, the inclination difference between the blueshifted channel and the lateral downflows is about 10–20°in both layers, which is similar as those found in observations (see Section 4.2).

Therefore, from Figure 4.12, we conclude that the parameters of the si-

mulations in $\tau = 0.1$ are similar to the observed ones, except in the vertical velocity of the lateral downflows. Furthermore, there appears a polarity reversal in the lateral downflows positions that seem to be linked to deeper layers. In consequence, observations of deep layers may be needed to unambiguously relate lateral downflows to magnetic field lines returning to the solar surface.

4.7 Summary

In this Chapter we have obtained the magnetic field vector of lateral downflows in penumbral filaments through a one-component inversion of the four Stokes profiles of the Fe I 6173 Åline observed by CRISP. We have used this information to characterize their magnetic and kinematic properties. We summarize them as follows:

- We find an exponentially decreasing distribution of lifetimes, with nearly all downflows lasting less than 6 minutes. The median lifetime is 3.2 minutes. Within this time span, they can fragment, disappear, and reappear. They seem to follow the wiggle of the filaments they are associated with. We speculate that forces derived from horizontal pressure balance are somehow responsible for this behavior.
- Lateral downflows show a median length of $0\farcs53$ and a width of $0\farcs16$. Therefore, high spatial resolution is needed to detect them.
- In the inner and middle penumbra, the downflowing patches move outward with a median horizontal speed of 85 m s^{-1}, whereas bright penumbral grains move inward (Müller, 1973; Sobotka & Sütterlin, 2001; Rimmele & Marino, 2006, and others). The outward horizontal motion decreases the LOS velocity observed in the lateral downflows, so the actual flow speeds could be larger than those indicated by Doppler measurements.
- Lateral downflows show a wide range of magnetic field strengths, from 1000 to 2000 G, with a median value of 1500 G. In the inner penumbra, the magnetic field strength of the center of blueshifted channels is of order 1000 G while is around 1600 G in the lateral downflows. However, we observe the inverse behavior in other penumbral regions, where lateral downflows harbor a weaker magnetic field strength (of about 900 G) that is 200 G less than that found in blueshifted channels.
- The median of the magnetic field inclination in the lateral downflows is $\sim$135°. Lateral downflows have field inclinations between 110 and 150°. They do not show polarity reversals. Nonetheless, some Stokes V profiles show an additional red lobe that suggests the presence of opposite polarity fields.

- The magnetic field azimuth infered from the inversion has a spatial distribution that might be in agreement with what is expected for magnetoconvection, where a lateral downflow has an azimuth greater that that of the blueshifted channel while the other is lower.

Regarding the morphology of the lateral downflows, we find that their widths are very similar to those resulting from 3D MHD simulations, but this is not the case for the length since the simulations show much larger lenghts (by a factor of 4). This suggests that the observed lateral downflows are fragmented possibly due to a lack of spatial resolution and/or sensitivity of our velocity measurements.

The velocities we observe in the downflows are significantly smaller than those resulting from the simulations, but become more similar after correcting the data for stray light. The remaining physical parameters computed from the simulations resemble those resulting from the observations. Due to the discrepancy in the LOS velocities obtained from the simulations and the observations, the association of lateral downflows with overturning convection is not completely unambiguous. In fact, other theoretical scenarios, such as the convective rolls proposed by Danielson (1961) or the twisted horizontal magnetic flux tubes of Borrero (2007) are also compatible with our observations from a pure kinematical point of view.

The simulations show a polarity reversal that coincides with the location of lateral downflows from $\tau = 1$ to 0.1. This suggests that penumbral observations at $\tau = 1$ are needed to link lateral downflows with polarity reversal.

5

Supersonic Evershed downflows at high resolution

To me, photography is an art of observation.
It is about finding something interesting
in an ordinary place...
Elliott Erwitt

5.1 Introduction

Great efforts have been made to disentangle unknown aspects about the penumbral velocity field. However, the higher the spatial resolution, the more intriguing the penumbra is, since it seems to consist of a zoo of structures from an observational point of view. One of these structures are the supersonic Evershed downflows, which existence is known since the beginning of the 1960s but have not been completely characterized.

Supersonic Evershed downflows were firstly noticed as line flags on both penumbral sides (Bumba, 1960). Other contemporaneous authors (e. g., Holmes, 1961; Maltby, 1964) considered line flags as an inherent part of the Evershed effect. According to Stellmacher & Wiehr (1971) and Wiehr (1995), line flags are due to the superposition of a strongly shifted satellite line and an unshifted main component in unresolved fine penumbral structure observations. In consequence, satellite lines can be separated from the main component and detected if the spatial resolution is high enough. Otherwise, their combination is seen as a line asymmetry.

Advances in the spatial resolution of observations and in inversion techniques enable to survey the penumbra in an unprecedented way. Bellot Rubio et al. (2004) noticed that magnetic field and velocity vectors are aligned in

the penumbra. Besides, these authors found that magnetic field lines return back to the solar surface and flow velocity is nearly supersonic in the outer penumbral boundary. Previously, Westendorp Plaza et al. (1997) also found flux returning in the outer regions of the penumbra but with a weaker velocity. Using Hinode data, Ichimoto et al. (2007b) linked supersonic Evershed downflows in the mid and outer penumbra to signal enhancements in the far-wing magnetograms. Recently, van Noort et al. (2013) described the physical properties of the supersonic Evershed downflows applying the coupled inversion technique. However, this study arises doubts because the inferred values are the highest ever registered in the penumbra.

In this Chapter, we use time sequence of high-resolution spectropolarimetric data (as previously, in Chapters 3 and 4) to scrutinize their temporal behavior of the supersonic Evershed downflows. Furthermore, thanks to be able to spatially resolve them, we describe in-depth their morphology and characterize their physical properties. Finally, our results are compared to those obtained in previous studies.

5.2 Supersonic Evershed downflows detected in observables

Velocity field in the sunspot shows strong redshifts that are concentrated in areas located at the end of flow channels (as in Figure 3.6). These redshifted patches indicate positions where the Evershed flow is returning back to the solar surface. According to Bellot Rubio et al. (2010) and van Noort et al. (2013), these redshifted concentrations harbor supersonic and nearly vertical LOS velocities, although the bisector computing yields more moderated values of $\sim$2 km s^{-1}.

On the top panel of Figure 5.1, a Dopplergram shows the LOS velocities computed for the sunspot's upper half acquired at 09:51:04 UT. LOS velocities have been calibrated and filtered for subsonic oscillations. There are many locations showing strong Evershed downflows. These are usually found in the outer and mid penumbra, being weaker in inner parts. Although they are most easily detected in the center side penumbra (thanks to the contrast over the blueshifted background), they also appear in the limb side penumbra. Black squares mark the position of examples of strong Evershed downflows located on each penumbral side. These examples are shown in detail below the upper panel of Figure 5.1.

The example 1 corresponds to a strong downflow situated in the middle part of the center side penumbra. On the left column, from top to bottom, a close up of a continuum intensity filtergram, a Dopplergram and a magnetogram in the far wing of the spectral line[1] (i. e., an ichimotogram) are

[1] Circular polarization maps at +420 mÅ, corresponding to a LOS velocity of 22 km s^{-1}.

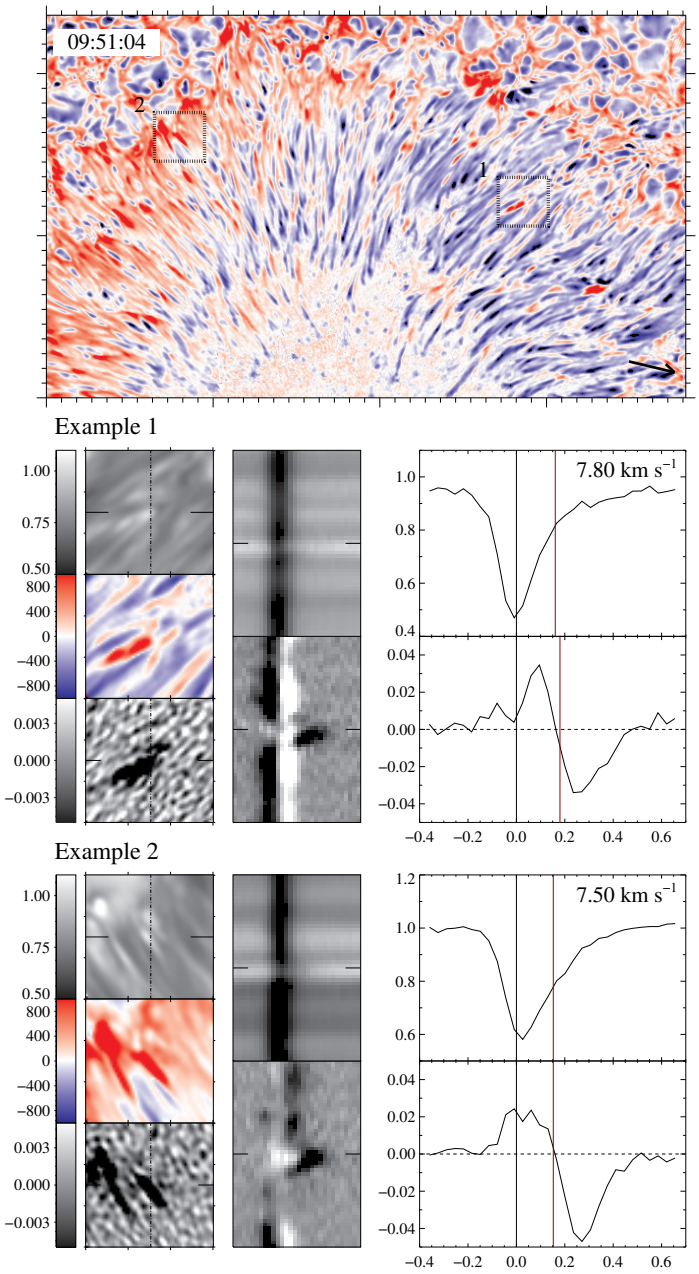

FIGURE 5.1:— Supersonic Evershed downflows detected from observables. The upper half of a Dopplergram acquired at 09:51:04 UT shows two examples of supersonic Evershed downflow enclosed by two black squares (top panel). Each major tickmark represents 10″. Each example is described below, as mentioned in the text. Each tickmark denotes 1″.

displayed over an square of 3″x 3″containing the example (each tickmark corresponds to 1″). The strong downflow coincides with a bright structure in the continuum intensity map. Regarding to the ichimotogram, a enhanced signal is associated with the strong downflow. Two horizontal dashes on both sides of each panel point out the vertical position of the strong downflow. On the middle column, there are shown the Stokes I and V spectra (top and bottom panel, respectively) emerging along the vertical slit drawn in the continuum intensity and ichimotogram close-ups. As on the left column, the position of interest is shown by two vertical dashes on both sides of each panel. Although here the Stokes I spectra is brighter than in other heights, the most remarkable feature is observed in the Stokes V spectra. In such position, the Stokes V spectra has a reversed polarity and is strongly shifted to the red at a whole. The corresponding Stokes I and V profiles are plotted in the rightmost panels (the upper and lower one, respectively). The dashed horizontal line plotted in the Stokes V profile panel indicates the zero polarization signal. The red wing of the Stokes I profile is more extended than the blue one, but the profile is unshifted, which cause weak LOS velocity values when computing line bisectors. However, the Stokes V profile has two regular lobes that appear reversed and strongly redshifted. The zero-crossing Stokes V value is shifted around 0.18 Å to the red, which means that the Doppler velocity is $\sim$8.75 km s^{-1}.

The example 2 is located in the outer boundary of the limb side penumbra. Its corresponding panels are in the lower position of Figure 5.1 and have the same layout as the previous ones. The strong downflow also coincides with a bright structure in the continuum intensity filtergram and a strong signal in the ichimotogram. Here, the Stokes I spectra clearly appears weaker in the line core and brighter in the wings than in the previous example. The Stokes V spectra also reveals a polarity reversal and is totally shifted to the red. The Stokes I profile is slightly redshifted and its red lobe is more extended than the red one. Finally, the Stokes V profile is regular with two reversed lobes and is also redshifted. In this case, the zero-crossing Stokes V yields 0.150 Å, i. e., a Doppler velocity of about 7.50 km s^{-1}.

According to these examples, supersonic Evershed downflows are present in our observations. The high spatial resolution and cadence of the time sequence of spectropolarimetric data enable us to study the physical properties and the temporal evolution of the supersonic Evershed downflows.

5.3 Searching for supersonic Evershed downflows

In order to characterize the physical properties and the temporal evolution of the supersonic Evershed downflows, it is needed to search for more examples. For this purpose, we have used some observables to detect signals that might be linked to the presence of supersonic Evershed downflows.

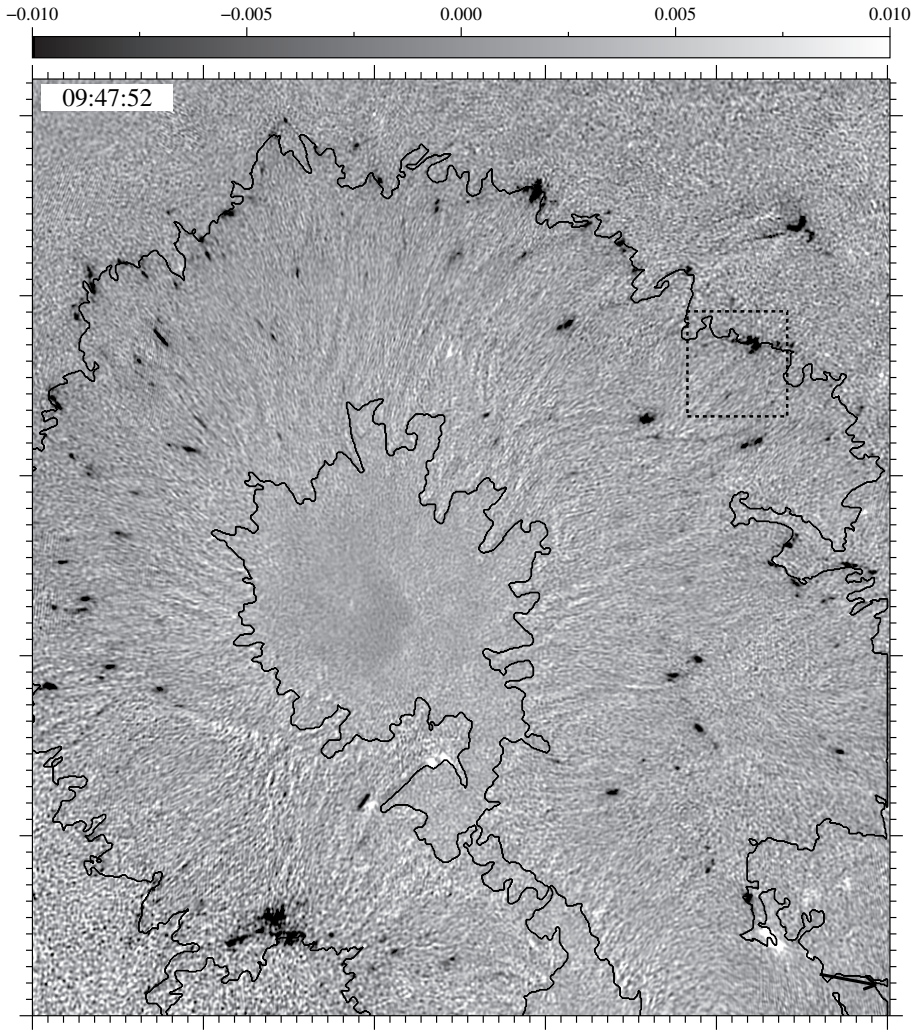

FIGURE 5.2:— Ichimotogram at +420 mÅ of Fe I 617.3 nm acquired at 09:47:52 UT. Dark patches represent locations where the amplitude of Stokes V at +420 mÅ is greater than the background noise. A black dashed square encloses the region shown in Figure 5.3. Black contours outline the penumbral boundaries. The black arrow points to the solar disk center. Each major tickmark corresponds to 10″.

Following Ichimoto et al. (2007b), we have used ichimotogram at +420 mÅ in the red wing of the Fe I 617.3 nm to search for positions with enhanced signal. Figure 5.2 shows patches with enhanced signal at that wavelength. These patches consist of pixels where the amplitude of the emerging Stokes V profile is greater from the background noise. Therefore, the features that cause the appearance of enhanced signals in the ichimotogram are lineshifts due to the existence of strong LOS velocities (Doppler effect), extended lobes as a result of the existence of strong magnetic fields (Zeeman splitting),

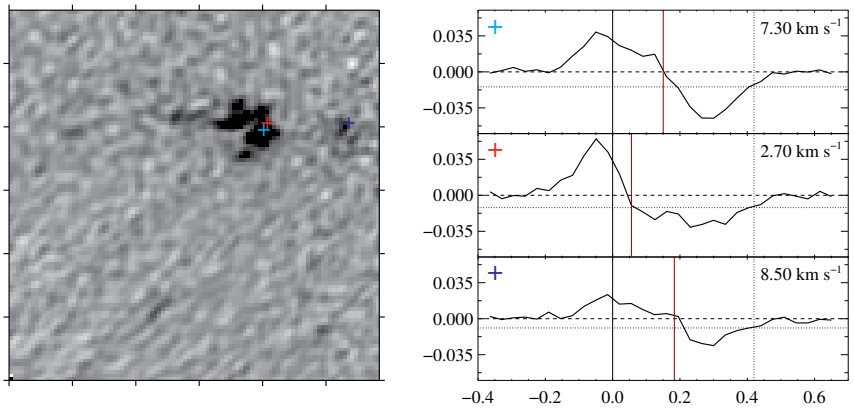

FIGURE 5.3:— Comparison between Stokes V profiles emerging from pixels with different ichimotogram signals within the region enclosed by a square in Figure 5.2. On the left side, a close-up of the region is shown. Each tickmark indicates a spacing of 1″. On the right hand, the Stokes V profiles emerging from each pixel are plotted. The x axis contains the relative wavelength position from 617.3 nm and is labelled in Å. Pixels of interest are marked with plus symbols of different colours, which are also used to identify the corresponding Stokes V profile. A black solid vertical line shows the quiet position. Red vertical lines indicate Stokes V zero-crossing values, which are expressed in km s^{-1} in the upper right corner of each panel. A black dotted vertical line shows the wavelength position considered for the ichimotogram and the horizontal ones indicate the amplitudes of Stokes V profiles at such a position.

and/or a combination of both effects. These concentrations are usually found in the mid and outer penumbral regions, being not observed in inner parts.

Figure 5.3 displays a close-up of a region that contains an enhanced signal in Figure 5.2. This area is located in the outer boundary of the center side penumbra. Patches are clearly identified as dark concentrations on the left side of Figure 5.3. Coloured plus symbols mark pixels whose Stokes V profiles are plotted on the right side. The blue symbol indicates a pixel where there is an enhanced signal in the ichimotogram and the LOS velocity given by the zero-crossing Stokes V value is supersonic (7.30 km s^{-1}). Here, the Stokes V profile is shifted as a whole. The red one also shows an enhanced signal in the ichimotogram but the zero-crossing Stokes V value yields a weak LOS velocity of about 2.70 km s^{-1}. In this case, the red lobe is more extended than the blue one but the profile is not as extended as the previous one. This suggests that there is a range of LOS velocities harboring this pixel. Finally, despite the purple symbol is located over a weak signal in the ichimotogram, the LOS velocity is around 8.50 km s^{-1}. This Stokes V profile shape shows a strong redshift and lobes broadening.

In addition, amplitudes of Stokes V profiles at +420 mÅ might have values close to the background noise. This feature produces fluctuations along

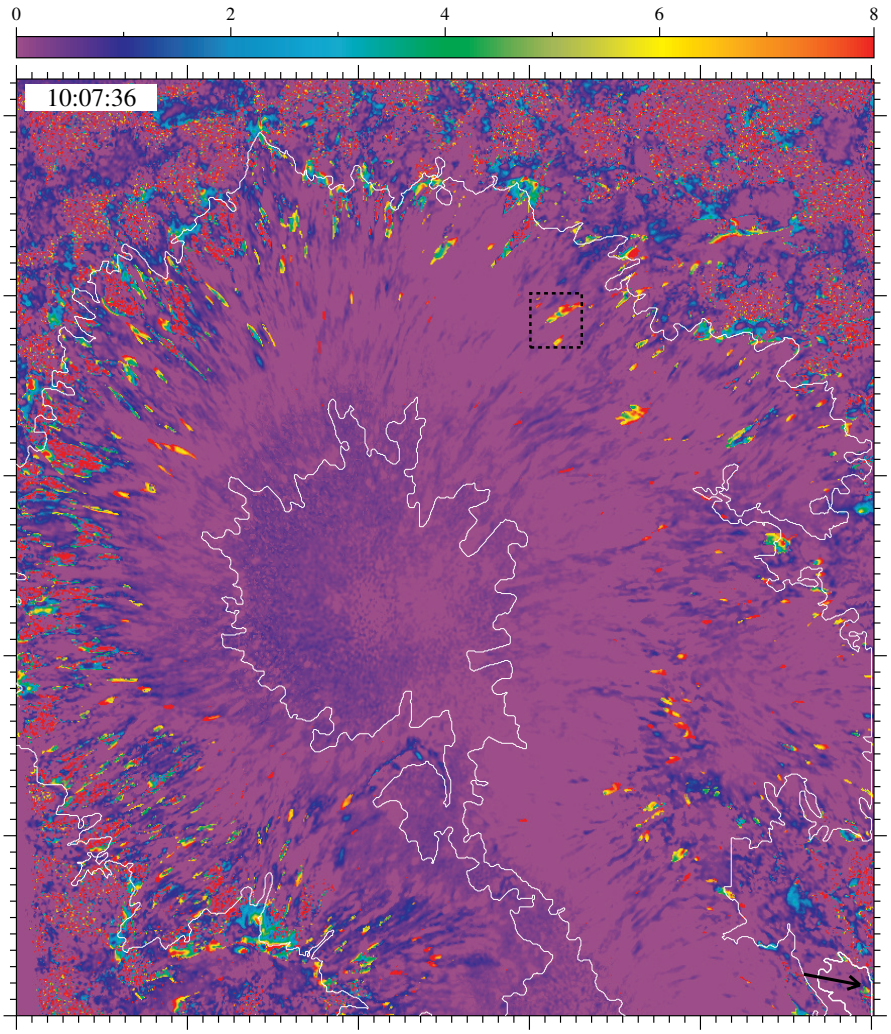

FIGURE 5.4:— Doppler velocities given by the Stokes V zero-crossing values at 10:07:36 UT. Only are represented positive values. A black dashed square encloses the region shown in Figure 5.5. White contours outline the penumbral boundaries. The black arrow points to the solar disk center. Each major tickmark corresponds to 10″.

the time sequence that hinder the following of these patches. This shortcoming can be observed in the movie available at http://spg.iaa.es/downloads

Therefore, ichimotograms are tools that enable us to identify locations susceptible to harbor pixels with supersonic Evershed downflows. Thus, it is necessary to analyze individually each Stokes V profile to distinguish those containing supersonic downflows.

We have computed the LOS velocities given by the Stokes V zero-crossing values in order to search for pixels with supersonic LOS velocities. Figure 5.4

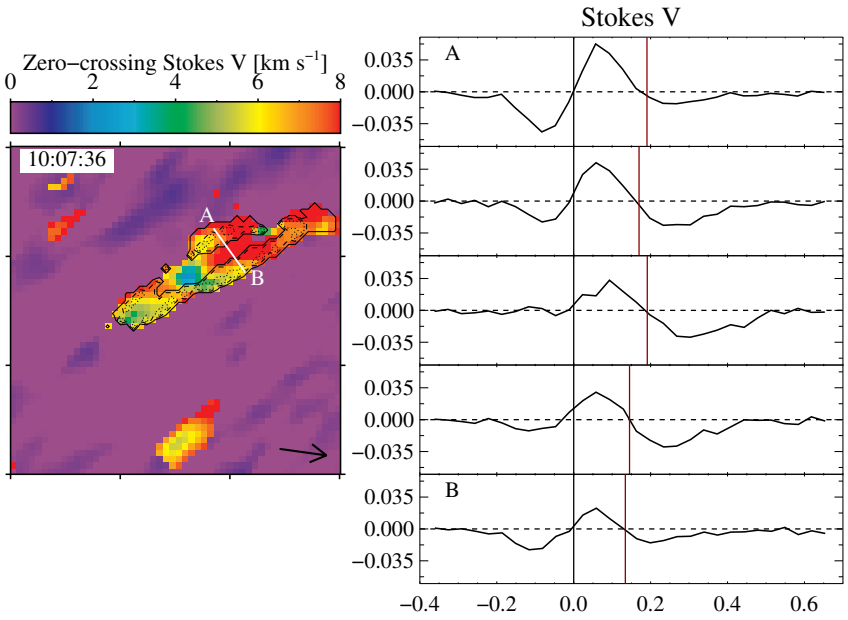

FIGURE 5.5:— Comparison between Stokes V profiles emerging from pixels with different ichimotogram signals within the region enclosed by a square in Figure 5.2. On the left side, a close-up of the region is shown. Each tickmark indicates a spacing of 1″. On the right hand, the Stokes V profiles emerging from each pixel are plotted. The x axis contains the relative wavelength position from 617.3 nm and is labelled in Å. Pixels of interest are marked with plus symbols of different colours, which are also used to identify the corresponding Stokes V profile. A black solid vertical line shows the quiet position. Red vertical lines indicate Stokes V zero-crossing values, which are expressed in km s^{-1} in the upper right corner of each panel. A black dotted vertical line shows the wavelength position considered for the ichimotogram and the horizontal ones indicate the amplitudes of Stokes V profiles at such a position.

shows the Doppler velocities acquired at 10:07:36 UT using this technique. There are only represented values greater or equal to zero. Non-purple positions indicate pixels harboring downflows according to the Stokes V zero-crossing. Thus, supersonic downflows might be situated in orange-red locations that form patches in different positions in the penumbra.

However, this simple method does not always work. Figure 5.5 shows an enlargement of the region outlined by the black square in Figure 5.4. A well-defined patch of downflows is clearly observed within this area. Although there are other small patches inside the represented area, we focus in the bigger one. It has an elliptical shape, being its length of order 2″ and its width approximately 0.″70. We have inspected the aspect of the Stokes V profiles inside this patch and not all of them have two regular lobes.

On the right side of Figure 5.5, at the top panel we observe a Stokes V profile with three lobes, where the additional one is located in the red

continuum and is small. After that, the amplitude of the additional one is greater than above and is comparable to the blue one. In the middle panel, there is a regular two-lobed Stokes V profile that is strongly redshifted. Then, a small additional lobe appears in the blue continuum that increases until be greater than the red one (having the same aspect as that plotted in the top panel). Thus, we have distinguished three types of 3-lobed Stokes V profiles: 1 non-reversed two-lobed Stokes V profiles with an additional red lobe (top and bottom panels), 2 reversed two-lobed Stokes V profiles with an additional small blue lobe (fourth panel), and 3 three-lobed Stokes V profiles with two minima of comparable amplitudes (second panel). In order to identify the locations of each type of Stokes V profile, different contours are overplotted on the patch: solid lines enclose type 1, dotted lines type 3, and dashed lines type 2. Pixels situated in the mid region of the patch, which are not contained in any contour, have two-lobed Stokes V profiles. Although Stokes V profile types seem to be somehow organized, this is not shared by other patches located in different locations. Besides, not all types are always present, often patches only contain three-lobed Stokes V profiles.

Therefore, as we only can trust in the LOS velocities given by the zero-crossing value of two-lobed Stokes V profiles, if we just consider them, the information provided by many pixels should be discarded.

In order to overcome this shortcoming, after the manual tracking of some stable patches, their observed Stokes profiles have been inverted using the SIR code. Figure 5.6 represents the four Stokes profiles emerging from pixels contained in the patch displayed in Figure 5.5. Specifically, the upper four panels correspond to the Stokes profiles emerging from the pixel selected for the second panel of Figure 5.5, while the lower ones are those from the pixel whose Stokes V profile is plotted in the third panel of such a Figure. Despite the shape of the Stokes V profile of each pixel is different, the remaining Stokes profiles shares some aspects. None of the Stokes I, Q, and U reveals any significant clue that indicates a supersonic Evershed downflow, excepting an extended red wing in the Stokes I profiles. This feature suggests us that there might be two different atmospheres (one fast and another slow) coexisting in the same pixel. Another possibility is that these Stokes profiles might be resulting of the existence of two different stratifications (again, one fast and another slow) along the LOS. Therefore, inversions have been performed considering two different atmospheres in each pixel.

The atmospheric parameters describing the two components of the model are assumed to be constant with height except for the temperature, which is allowed to have two nodes. In particular, the magnetic field vector and the LOS velocity are constant in two components. Macroturbulence[2], microturbulence and straylight were set to zero. Although this choice is reasonable

[2]The macroturbulence velocity is set to 0.01 km s^{-1}.

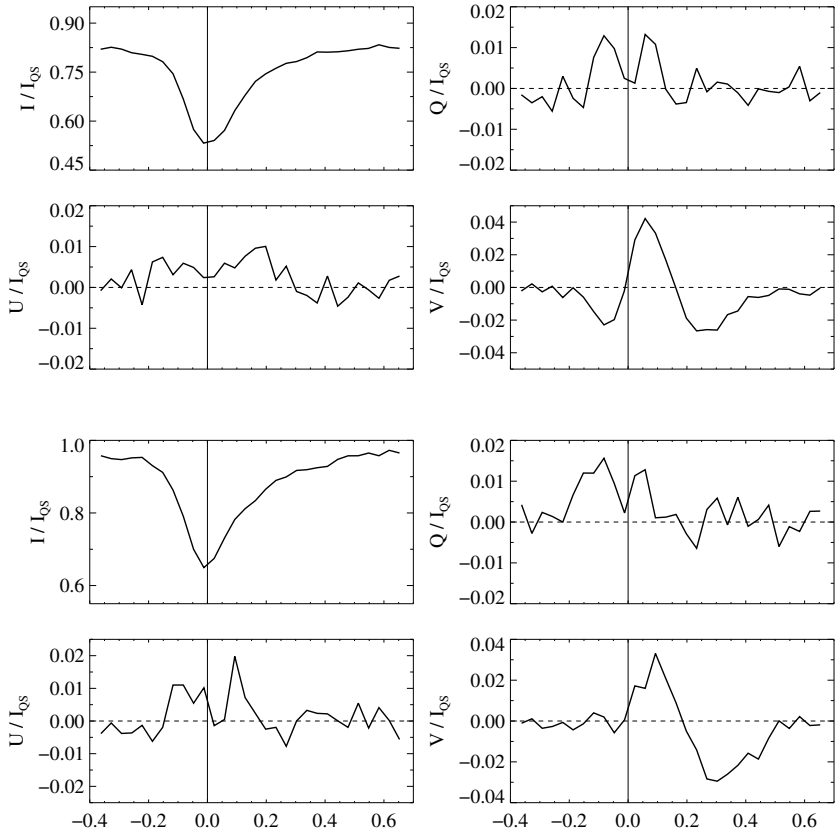

FIGURE 5.6:— Stokes profiles emerging from two pixels represented in the second and third panels of Figure 5.5.

TABLE 5.1:— Atmospheric parameters considered for the inversions.

Parameters	**Fast component**	**Slow component**
LOS velocity	11 km s^{-1}	0.5 km s^{-1}
Magnetic field strength	2 kG	1 kG
Magnetic field inclination	50°	130°
Filling factor	95 %	5 %

according to the Stokes profiles plotted in Figure 5.6, it results in a significant simplification of the problem. Throughout this Section, the two components of the model will be referred to as *fast* and *slow* atmospheres. These components are mixed according to a filling factor that determines the fractional

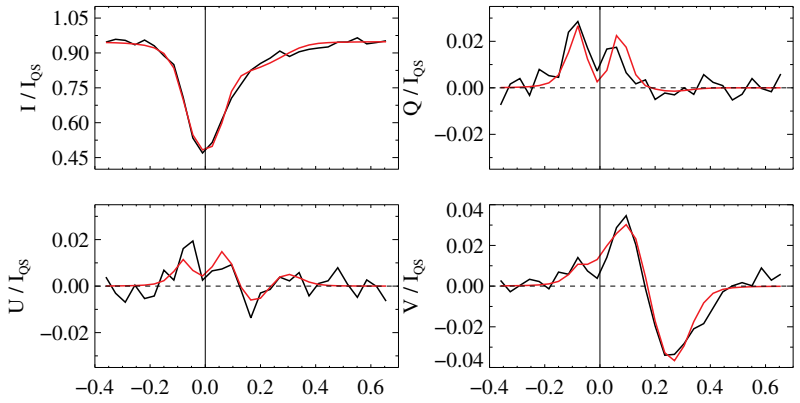

FIGURE 5.7:— Comparison between the observed Stokes profiles and the synthetic ones (black and red profiles, respectively). Horizontal dashed lines mark zero polarization signals. The x axes represent the relative wavelength position from 617.33 nm and are labelled in Å.

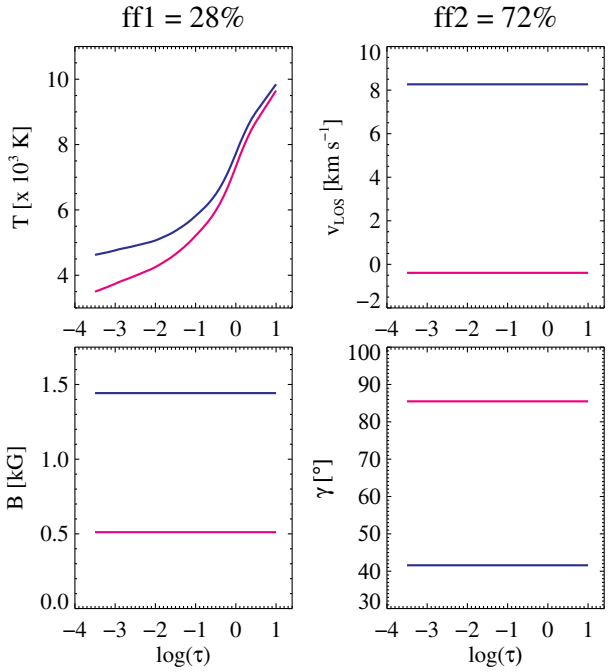

FIGURE 5.8:— Physical parameters resulting from the inversion for the fast and slow components (blue and magenta lines, respectively).

area of the pixel occupied by each one. The initial parameters set to each component are shown in Table 5.1.

Figure 5.7 shows an example of the synthetic lines fitting with respect to the observed ones, which are the same represented as the example 1 in Figure 5.1. Despite linear polarization signals are noisy and the fitting is not good enough, synthetic Stokes I and V profiles are very similar to those observed emulating the most interesting observational clues. In addition, Figure 5.8 illustrates some physical parameters resulting from the inversion as a function of height. Fast and slow components are represented by blue and magenta lines, respectively, and they occupy 28 and 72 % of the total area of the pixel. Temperature exponentially drops from the photosphere to the chromosphere in both components and the fast component is always hotter (brighter) than the slow one in all heights. The LOS velocity of the fast component is supersonic ($\sim$8 km s^{-1}), while the slow one is around -0.5 km s^{-1}, representing an upflow. Regarding the magnetic field, there is a great difference between both components. The fast component harbors a magnetic field of almost 1.5 kG with an inclination of about 40°(its polarization is opposite to that of the sunspot), and the slow component has a magnetic strength of 0.5 kG and its magnetic lines are close to be horizontal ($\sim$90°). Therefore, from this pixel we can extract that the fast component is supersonic and its magnetic field is much greater than the slow one and is vertically returning back to the solar surface.

It is noticed that we have only carried out the inversions in pixels where the LOS velocity obtained from the Stokes V zero-crossing is greater than 2.5 km s^{-1}, because we are just interested in those pixels with strong downflows. The FOV displayed in the panels of the Figure 5.9 is the same as in the example 1 of Figure 5.1. On the top panels of Figure 5.9, the continuum intensity, ichimotogram and the LOS velocities obtained from the Stokes V zero-crossing are displayed. The same structure is clearly appreciable in the three panels. The main characteristics of this structure is its brightness in the intensity map, the enhanced signal in the ichimotogram and its redshifted LOS velocities.

The second row of the Figure 5.9 shows the magnetic field strength, inclination and LOS velocity retrieved for the fast component. Most of the patch has a magnetic field of about 1.5 kG and inclinations of 50°approximately, i. e., harboring reverse polarity. The LOS velocity covers a wide range of values, from $\sim$3 km s^{-1} to more than 8 km s^{-1}. Besides, strong redshifted pixels coincide with those where the magnetic field is more vertical and are brighter. However, a relation with the magnetic field strength is not found.

Regarding the slow component (third row of the Figure 5.9), the magnetic field has more moderated values and its inclination is closer to 90°, reaching up to 120°. This latter means than the field lines are horizontal or has the same polarity as the sunspot. This component often shows negative LOS velocities (~ -0.3 km s^{-1}), except in some pixels in the lower right

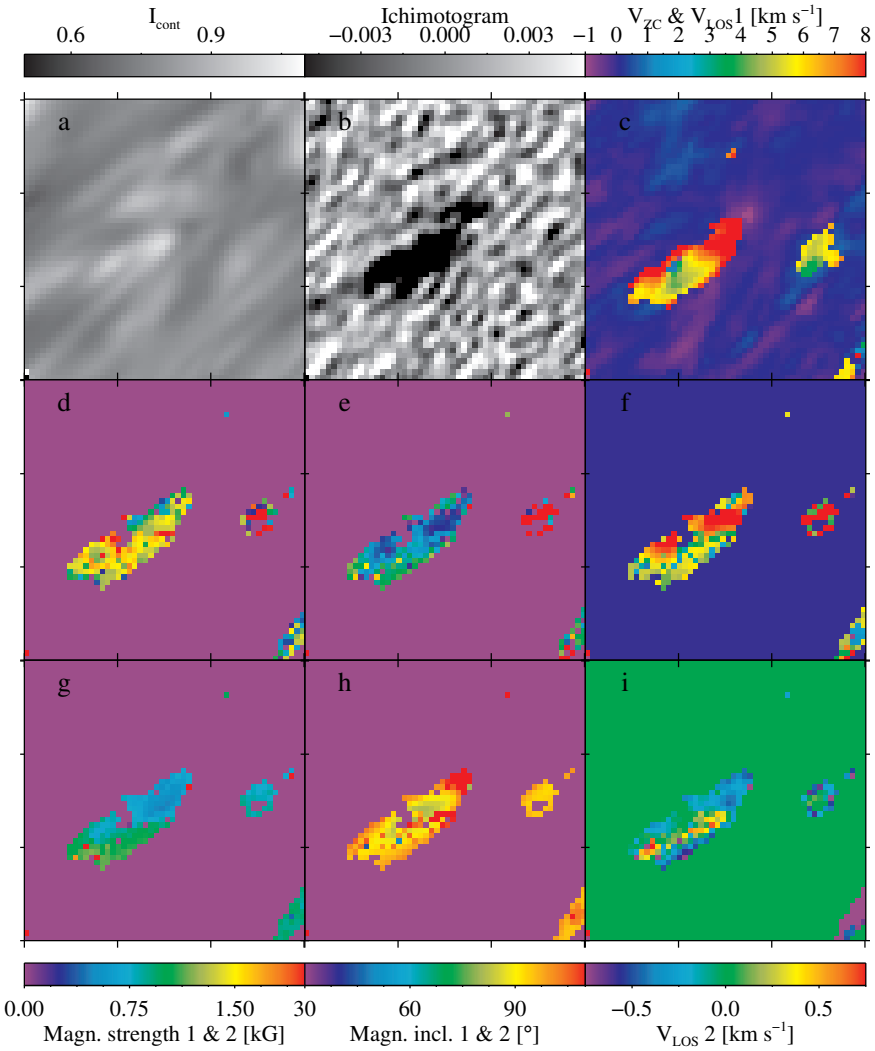

FIGURE 5.9:— Maps of some physical parameters retrieved for each component in the surroundings of the pixel described in Figures 5.7 and 5.8. This pixel is contained in the central patch. *a*, Intensity continuum filtergram; *b*, ichimotogram; *c*, LOS velocity given by the Stokes V zero-crossing value; *d, e, f*, magnetic field strength, inclination and LOS velocity of the component 1 (fast); *g, h, i*, the same for the component 2 (slow). Each axis tickmark represents 1″.

part of the patch were the inversion has not been as successful as in other parts.

In conclusion, in order to identify patches containing supersonic downflows we have follow a rough examination of the ichimotograms and the Stokes V zero-crossing values that has been polished using the information retrieved from the inversions.

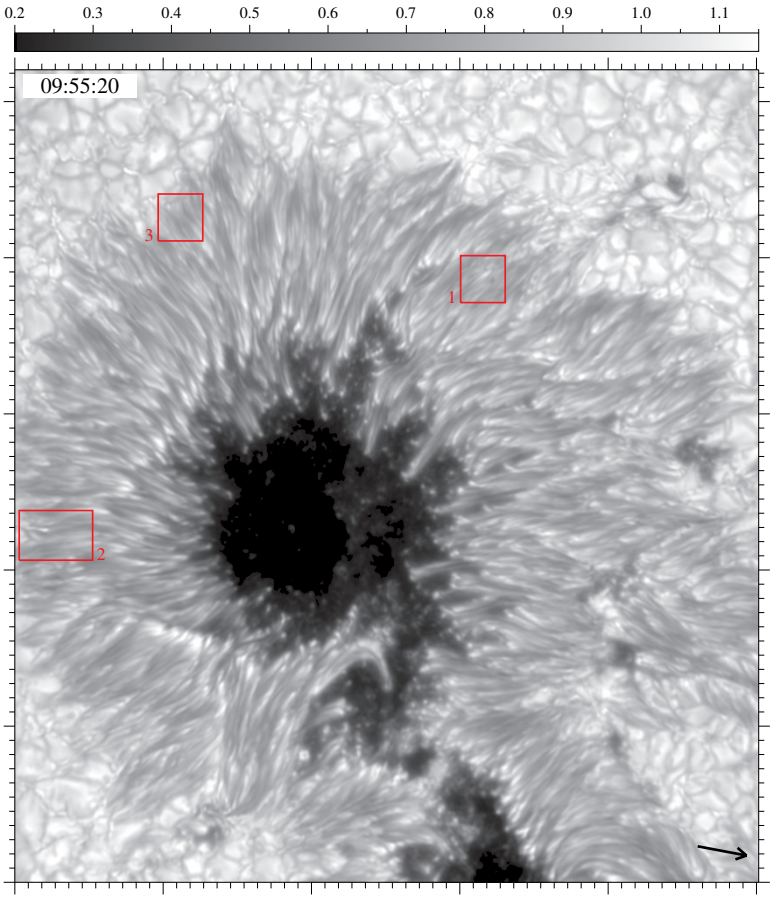

FIGURE 5.10:— Locations of the examples described in Section 5.4 and displayed in Figures 5.11–5.13 overplotted on a continuum intensity filtergram. Each major tickmark represents 10″. The arrow points to the disk center.

5.4 Temporal evolution of supersonic Evershed downflows

We have detected forty examples of patches containing supersonic Evershed downflows. They are usually located on the outer of both penumbral sides. Some of them are also found in the middle penumbra. However, after repeating several times the tracking of the detected examples, the non-stability during their lifetime, the emergence of rare and irregular Stokes V profiles, or any doubt about their authenticity were the most common causes to discard some of them. Finally, we have studied the temporal evolution of thirteen patches, whose behaviors are well-represented by three examples, whose positions are described in Figure 5.10. These examples are described in this Section. The complete sequence is available in spg.iaa.es/downloads.

Movies also show the Stokes profiles of the selected pixel.

In order to follow each patch with time, we have taken into account a compromise between all the information described in the previous Section. Therefore, the selected criteria is to manually track the position where the LOS velocity values (that obtained for the fast component from the inversion and the one given by the zero-crossing value of the Stokes V) are the highest. This is not an easy task in some moments due to the appearance of fluctuations of the values (mainly caused by the simplicity of the models used to perform the inversions). To solve these situations, we have considered those pixels that makes the tracking as smoother as possible which is enough to disentangle the main aspects of the supersonic Evershed downflows behavior.

5.4.1 Example 1

Figure 5.11 shows the temporal evolution of a patch in the middle part of the center side penumbra that contains supersonic Evershed downflows. It is located at the end of a filamentary structure. In order to be visually clearer, the most significant non-consecutive scans are displayed. Although the patch is clearly observed in all maps from 09:42:00 UT, there was already visible before but hard to follow the position of the supersonic downflow.

The point of interest appears in the boundary of the patch but just in the middle of a bright structure. Soon after, there is a contribution from a bright structure, which interaction is also observed in the ichimotogram, the velocity and the inclination panels (second row). At that moment, the marked pixel indicates a supersonic downflow. It seems that the appearance of the supersonic downflow is a consequence of that merging. The supersonic downflow is now located at middle of the patch and of the bright structure. From the second to the tenth row, the marked pixels show a supersonic downflow, with LOS velocities from 7.2 to 9 km s^{-1}, heading the bright structure that moves outward. This trend breaks at 10:06:00 UT when the patch is fragmentated and the LOS velocity is much lower (the fast component has a velocity of around 3 km s^{-1}). However, it is restored a few scans before becoming again supersonic in the last row.

During the life of this patch, there occur almost four interactions with structures harboring supersonic downflows. Some of them seem to contribute to the analyzed pixel, boosting its LOS velocity.

Regarding the magnetic field, it remains vertical with values between 25 and 55° during all the sequence. It is noticed that positions with the more vertical inclinations coincide with those with stronger LOS velocities during interactions. The magnetic field strength usually varies between 1 and 1.5 kG and no relation with other parameters is found.

5.4.2 Example 2

This case represents a patch that is located between the mid and outer limb side penumbra and ends beyond the outer border. It remains visible during all the sequence, i. e., its lifetime is of at least 50 minutes although it surely lasts more. It is located in a very bright structure ($\sim$1.1 I_{QS}) that moves outward at the end of a filament. As in the previous case, the patch shape looks different when comparing the panels corresponding to the observables and the parameters retrieved from the inversion.

The LOS velocity of the fast component is usually greater than 5 km s^{-1}, reaching up to more than 9 km s^{-1} during some periods of time. In spite of the fluctuations observed in such a parameter, the LOS velocity of the fast component is recurrent and seven enhancements (and decreasings) are observed. Not all of them have the same duration but they reach supersonic values. Thus, some of moments these recurrences are displayed in Figure 5.12. The LOS velocity shows supersonic velocities in all row (except in the fifth and the ninth, which are used to display how the pixel is when the LOS velocity is not supersonic).

Besides recurrences, at least two fragmentations are present in this example. They start as brightenings that move towards the head of the patch. This causes an acceleration of the proper motion outward at the head of the patch that lengthen it (an example is illustrated in the fourth row). As a consequence, the enhanced LOS velocity region inside the patch is also extended until it breaks, although in intensity it is still observed as an entire structure. At the moment of the rupture, the LOS velocity of the separated region grows, as well as its intensity. Two or three frames later, it fades. However, the second part of the patch (which has lagged behing) continues its trajectory without being influenced by the fragmentation.

The magnetic field strength covers a wide range of values, from 1 to 2 kG. No correlation has been observed between the magnetic field strength and the LOS velocity. The magnetic field inclination has values around 20° and 60°, pointing to a vertical magnetic field lines with opposite polarity to the sunspot. The inclination is more vertical in those positions with greater LOS velocity. However, it does not mean that the highest LOS velocity are related to the more vertical magnetic field.

5.4.3 Example 3

Figure 5.13 shows the last example, which is located on the limb side. Here, we illustrate a fragmentation and follow the patch moving outwards. The initial patch starts in the middle penumbra and moves outward continuing beyond the outer penumbral border. All the process lasts 12 minutes approximately, maybe it is present longer but we are not able to identify the patch in more frames. It is firstly noticed as a bright structure at the

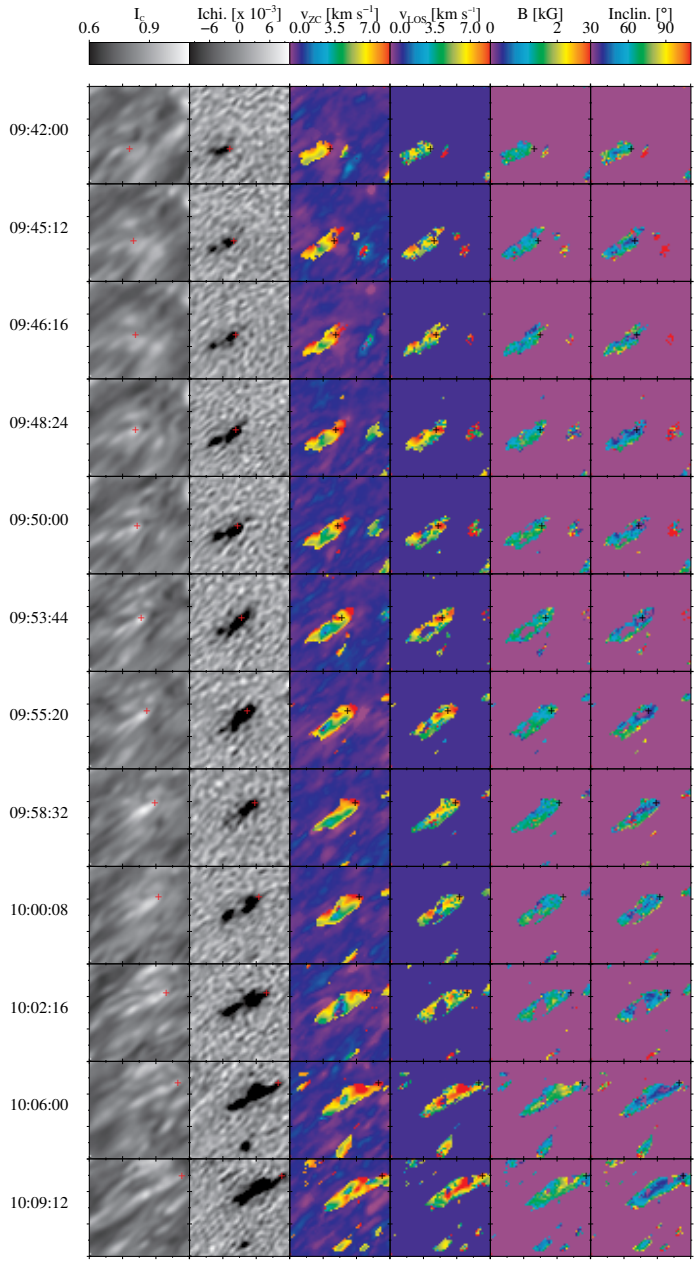

FIGURE 5.11:— Temporal evolution of the physical parameters of a patch located in the center-side penumbra (marked as 1 in Figure 5.10). From left to right: continuum intensity filtered for subsonic oscillations, ichimotogram, LOS velocity given by the Stokes V zero-crossing wavelength, LOS velocity, magnetic field strength and inclination of the fast component given by the inversions. A plus symbol indicates the pixel that is followed. Time increases from top to bottom, as indicated on the left-hand side. Each major tickmark represents 1″.

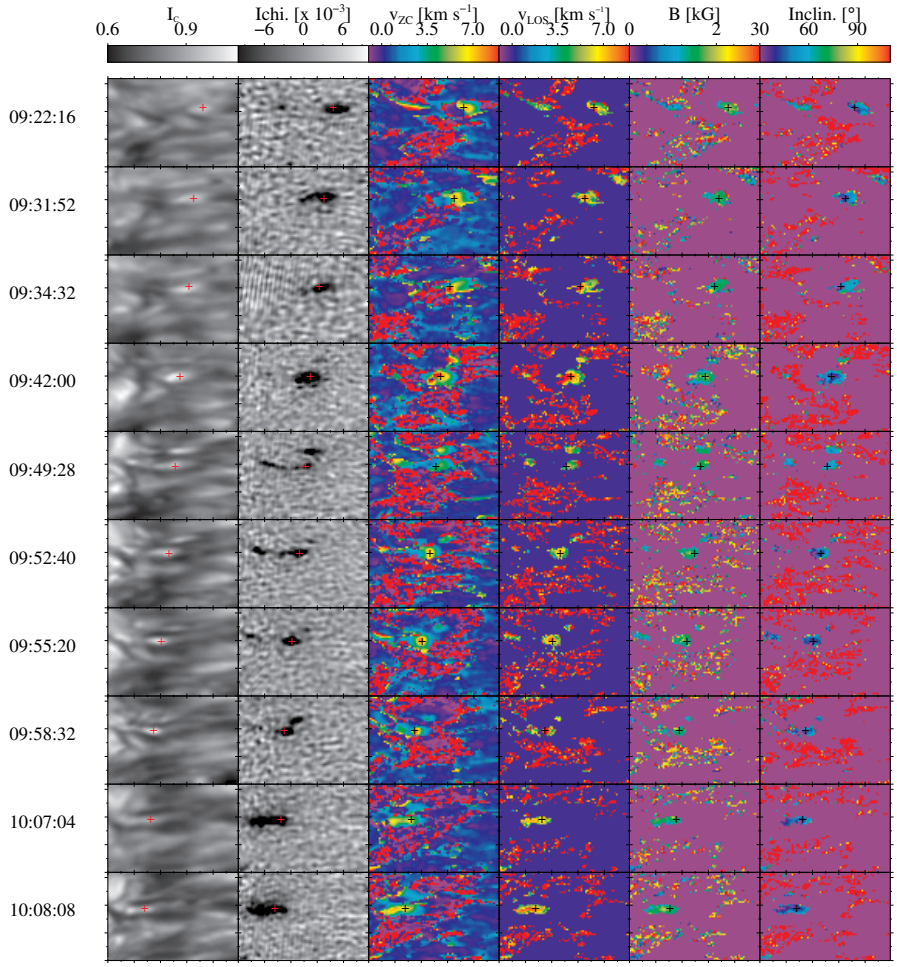

FIGURE 5.12:— Example of patch harboring a supersonic Evershed downflow located in the middle limb side penumbra (example 2 of Figure 5.10). The layout is the same as in Figure 5.11.

end of a filament. Four frames later, it brightens, is accelerated and the Stokes V profile is shifted. Panels of Figure 5.13 display frames where we have carried out the inversion because the Stokes V profile shifting suggests the presence of a supersonic downflow. Unlike in the previous cases, the patch shape remains approximately unchanged when comparing it between the different parameters displayed. The selected pixel is centered in the patch in all parameters except in the ichimotogram where is shifted to the left.

The LOS velocity of the fast component reveals a sudden increase from $\sim$4 to 8 km s^{-}1 (two first rows of Figure 5.13). Just after that, the patch suffers a fragmentation. However, in this case, the part of the patch with the enhancement of LOS velocity becomes motionless and darker. After nine

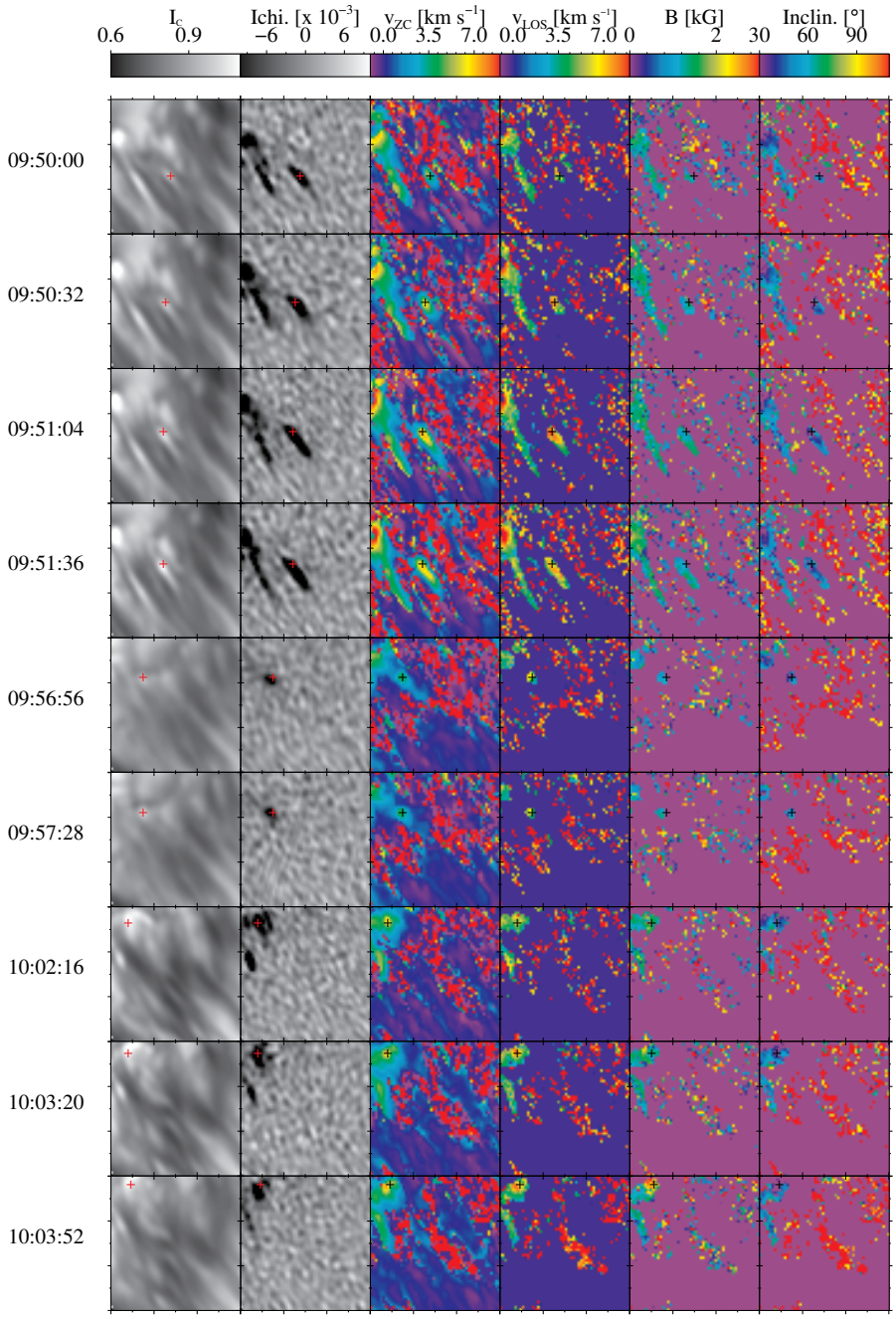

FIGURE 5.13:— Patch harboring a supersonic Evershed downflow located near the outer limb side penumbra (example 3 of Figure 5.10). The layout is the same as in Figure 5.11.

frames, it fades. In the meantime, the fragmented part gets brighter and accelerates its motion toward the outer penumbra. Therefore, the increase

of LOS velocity is not accompanied by any brightening. When the patch achieves the outer penumbral border, the LOS velocity abruptly grows from 6 to 8 km s^{-1} (seventh and eighth rows), subsequently falling down (last row).

Despite the magnetic field strength is around 1–1.3 kG at the beginning, there is a great rise of $\sim$1 kG at the end of the sequence (when the selected pixel protrudes into the quiet Sun) that causes wider Stokes V profiles. All the selected pixels have magnetic inclinations of about 20–50°, i. e., they harbors vertical magnetic field lines with opposite polarity as previously.

In this case, as can be seen in Figure 5.13, there is a correlation between the magnetic field parameters and the LOS velocity. However, as before, this relation is not one-to-one.

Therefore, detected supersonic Evershed downflows have a wide range of lifetimes. They can be detected during just two frames (i. e. 1 minute) or more than ten frames ($\sim$5 minutes). Their LOS velocities are greater than 7.2 km s^{-1}, reaching up to 10 km s^{-1}. They harbor strong and vertical magnetic fields (of $\sim$1.5 kG and 20–60°, respectively) of opposite polarity to the sunspot. The main properties of the temporal behavior of the supersonic Evershed downflows can be summarized as follows:

1. Supersonic Evershed downflows are usually observed in the outer penumbra. Sometimes, they are detected in the middle penumbra, but not in the inner penumbra where their LOS velocities are weaker.

2. They are contained in compact patches that move outward. Pixels usually display strong ichimotogram signals but some of them not.

3. These patches are always located at the end of penumbral filaments and coincide with bright intensity structures.

4. Their LOS velocity increases until a peak value and, after that, they fade. In some cases, the patch disappears but sometimes there are recurrences.

5. Positions with high LOS velocity coincide with those harboring more vertical magnetic field. However, not always a relation between LOS velocity and magnetic field is found.

6. When a patch is at the outer penumbral boundary, there is an enhancement of LOS velocity and magnetic field strength. However, there are no clear changes in the magnetic inclination. Some frames later, as the patch moves beyond the sunspot it is integrated as part of the quiet Sun.

7. Patches suffer mergings and fragmentations that share common physical aspects. When there is a merging, the LOS velocity increases as well as the magnetic field inclination and the continuum intensity, but no changes has been detected for the magnetic field strength. In fragmentations, the intensity structure brightens and its proper motion is accelerated. At that moment, the supersonic downflow heads the structure breaking the patch and vanishes some frames later.

5.5 Statistical analysis of the supersonic Evershed downflows

We have carried out an statistical analysis of the supersonic Evershed downflows using the physical parameters of the fast component retrieved from the inversions. As not all the inversions have worked, we have examined the synthetic profiles that better match to the observed ones in order to not include wrong results. We have observed that only some types of Stokes V profiles fit well. Following the clasification performed in Section 5.3, these are types 1, 2 and 3 with a very small additional lobe, and 4 when the amplitude of the central lobe is greater than those of the other two lobes. Besides, the last criterion involves the value of χ^2 to finally decide if it is a good fitting or not.

Therefore, all in all, the statistical analysis has been carried out considering 16486 pixels within the thirteen patches. From all of these pixels, 3750 harbor supersonic LOS velocities on the fast component.

Figure 5.14 displays histograms of the LOS velocity, magnetic field strength, inclination and filling factor of the fast component. The pixels within the patches shows a broad range of positive LOS velocities with a peak in 5.5 km s^{-1}. Most of the supersonic ones have LOS velocities in the range between 7.5 and 9.5 km s^{-1}. Their distribution decreases exponentially, with a median value of 8 km s^{-1}. The histograms of magnetic field strength and filling factor of supersonic pixels are similar to those obtained if all the pixels are considered. The median value of the magnetic field strength of the supersonic pixels is about 1.5 kG, and that of the filling factor is 30 %.

The most significant difference is found when comparing the inclination distributions obtained for each sampling in Figure 5.14. The inclinations of the supersonic pixels vary between 10 and 65°with a median of 45°, while the other sampling covers a range from 5 to 110°. This suggests that the polarity of all the supersonic pixels is opposite to that of the sunspot and are more vertical. Finally, the distribution of the continuum intensity of the supersonic pixels is shifted to higher values than those found for the other sampling, which means that the supersonic pixels tend to coincide with brighter intensity positions. The median value of the continuum intensity of

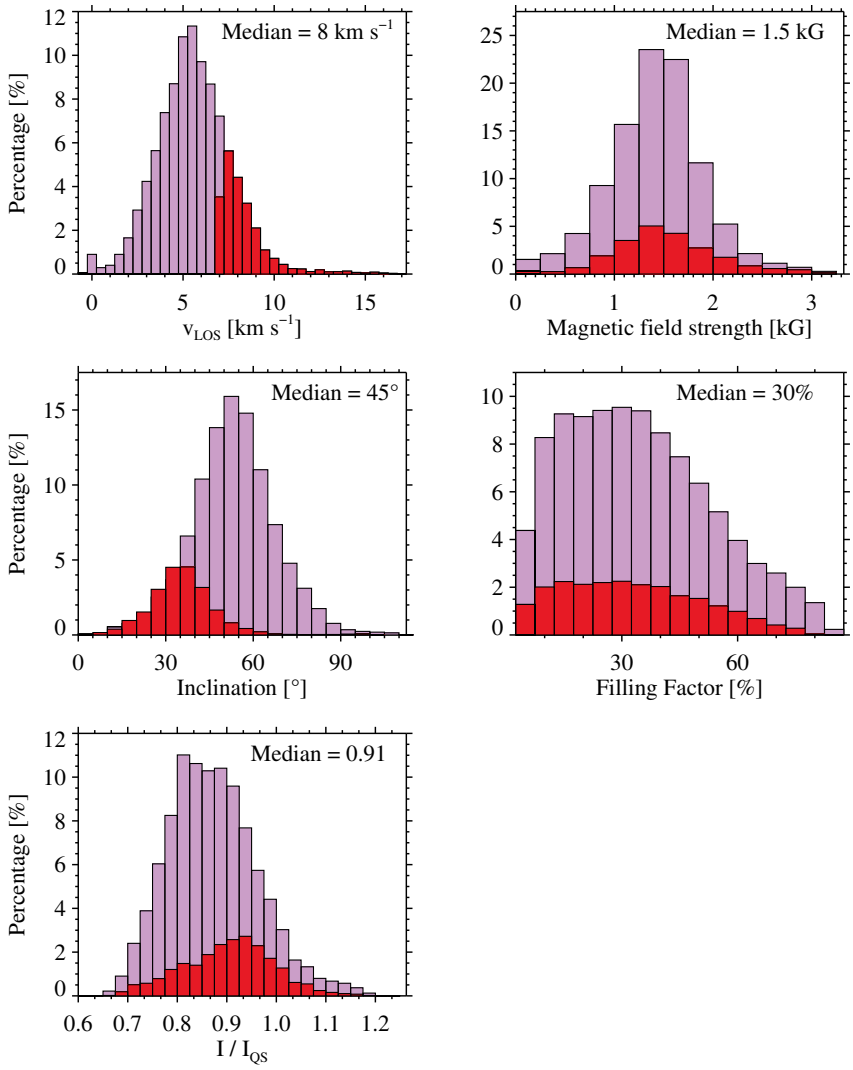

FIGURE 5.14:— Histograms of LOS velocity, magnetic field strength, inclination, filling factor (of the fast component) and continuum intensity of all the pixels considered for the statistics and of those having supersonic LOS velocities (purple and red boxes, respectively). The median values of each red distribution is indicated in the upper right corner of the panels.

the supersonic pixels is 0.91.

5.6 Comparison with previous studies

The supersonic Evershed downflows we have analyzed qualitatively share many aspects with previous studies. In this Section, we compare our results with those from previous studies.

Our results point to the same direction as those obtained by Bellot Rubio et al. (2004). They found that the azimuthally average LOS velocity is about 6 km s^{-1} from outer penumbral regions until the boundary. This suggests that there have to exist pixels with LOS velocities greater than that one so close to be supersonic. Here, we obtain that the median value of the supersonic velocities is 8 km $s^{-}1$, only considering pixels harboring supersonic LOS velocities and located at different penumbral regions. Considering the distribution of all the pixels contained in the analyzed pixels (purple distribution in Figure 5.14), the median of the LOS velocity is approximately 6 km s^{-1}. Regarding the magnetic field, Bellot Rubio et al. (2004) obtained magnetic inclinations for the flux tube component between 85 to 100° toward the outer sunspot border. Despite their magnetic field lines have an opposite polarity to the sunspot (at least those closer to the outer border), they are more horizontal than the ones found in this thesis (median inclination of 45°). The magnetic field strength retrieved from our inversions is stronger than the one from Bellot Rubio et al. (2004) (1.5 vs 1 kG). Regardless the cuantitative values, the tendency found by Bellot Rubio et al. (2004) is similar to that obtained in this thesis. In addition, these authors showed that the magnetic field and velocity vectors are aligned. We cannot discuss this point because we have not decomposed the velocity vector in its different contributions.

As in del Toro Iniesta et al. (2001), we have also detected supersonic Evershed downflows in the middle penumbra. Besides, these authors found that Evershed downflows are concentrated in cold magnetic tubes and have LOS velocities of order 16 km s^{-1}. However, according to this chapter, the pixels showing supersonic downflows tend to be bright, i. e., to be hot. In del Toro Iniesta et al. (2001) the background component temperature is hotter than the downstreaming one (see Figure 3 therein), but the opposite situation is shown in Figure 5.8. The LOS velocity given by the inversion carried out by these authors is of order 16 km s^{-1}, which doubles the median value obtained in Section 5.5. In addition, we have observed that these values are not commonly found in the penumbra, representing only a 1 % of those studied here. There are also discrepancies when comparing the magnetic field inclinations obtained in both studies. While the inclination found by del Toro Iniesta et al. (2001) is similar to that of Bellot Rubio et al. (2004), our results indicate that magnetic field lines are more vertical. In spite of this, both inversions relate supersonic downflows with opposite directed magnetic field lines. Finally, the magnetic field strength is similar on both studies.

Using a set of magnetograms in the far red wing (ichimotograms) of the Fe I 630.2 nm, Ichimoto et al. (2007b) related the detection of strong signals with the presence of vertical supersonic Evershed downflows in the mid and outer penumbra. These locations also have polarity opposite to that of the sunspot, suggesting to be the sinks of the Evershed flow. Bellot Rubio et al. (2010) showed that a pixel with enhanced ichimotogram signal had strongly

redshifted Stokes V profiles and a LOS velocity of order 9 km s^{-1}. These results are alike those obtained in this thesis. However, we have demonstrated that these enhanced signals in the ichimotogram are not only caused by strong lineshifts since they can also indicate the presence of a strong magnetic field (see Section 5.3.). Therefore, not all the positions with increased signals necessarily indicate supersonic Evershed downflow.

Normal supersonic Evershed downflows observed at the end penumbral filaments in the outer penumbra by van Noort et al. (2013) are brighter in photospheric layers and have maximum LOS velocities of order 10 km s^{-1}, magnetic field strengths between 2–2.5 kG and inclinations of 150–180° (opposite to the polarity of the studied sunspot). Therefore, our results are compatible with these ones, except the LOS velocity and magnetic strength which are stronger in van Noort et al. (2013). These authors also found *peculiar* supersonic downflows in the outer edge of the penumbra when this is bordered by a region with strong magnetic field (such as plages or pores). They are also bright in the photosphere but have very strong LOS velocities of order 22 km s^{-1}, magnetic field strengths reaching up to 7kG and inclinations of about 130°(with the same polarity of the sunspot as going upward in the solar atmosphere). We do not find any case that could be identified as a *peculiar* supersonic Evershed downflow so our results are incompatible with these. Therefore, maybe this type of supersonic downflows may exist but only in some special conditions, i. e., when its position is close to a strong magnetic area.

5.7 Conclusions

In this Chapter we have studied the temporal evolution of the supersonic Evershed downflows and characterize them physically. This has been performed thanks to the high spatial resolution and the excellent seeing quality of our spectropolarimetric data of a sunspot located very close to the disk center that enables us to have LOS velocities little affected by projection effects. In order to detect the supersonic Evershed downflows, we have considered information from the continuum intensity filtergrams, LOS velocities given by the Stokes V zero-crossing wavelength and the ichimotograms, together with the LOS velocity and the magnetic field vector inferred by two-component inversions of the four Stokes profiles of the patches harboring supersonic Evershed downflows.

The supersonic Evershed downflows are detected at different locations between the mid and outer penumbra, so they are not only located near the outer penumbral border. They are contained in compact patches moving outward. These patches not always show strong ichimotogram signals. In continuum intensity filtergrams, these patches are observed as bright structures located at the end of a single filament or a more complex filamentary

structure. However, sometimes is not easy to identify the related filament. The lifetimes of the analyzed supersonic Evershed downflow vary from one to more than ten minutes.

Most of the supersonic Evershed downflows show a LOS velocity between 7.5 and 9.5 km s^{-1}, with a median value of 8 km s^{-1}. Their magnetic field lines tend to be more vertical, with a median of 45°, than the pixels surrounding them inside the patch. This also means that the polarity of the magnetic field related to the supersonic Evershed downflows is opposite to that of the sunspot. The magnetic field strength of the supersonic Evershed downflows has a median value of 1.5 kG. We have also noticed that supersonic downflows tend to be cospatial with bright pixels, being the median value of the continuum intensity of 0.91.

From the study of time sequences showing some representative examples of supersonic Evershed downflows, we extract that they appear, their LOS velocity increases until a peak value, fading some frames later. Then, they can manifest two different behaviors: the patch disappears and there are no more supersonic downflows, or the patch is still visible and a recurrent supersonic downflow is observed some frames after. Besides, patches are susceptible of suffering mergings and fragmentations. When patches merge, the LOS velocity increases as well as the magnetic field inclination and the continuum intensity, but the magnetic field strength remains unchanged. This indicates that the Evershed flow associated to different filaments can sinks at the same position. In the case of fragmentations, the intensity structure brightens and boosted outward. At that moment, the supersonic downflow heads the structure breaking the patch.

During the evolution of the patch, it is noticed that regions with the stronger LOS velocities also have the more vertical magnetic field, but it does not mean that there is a relation one-to-one between the LOS velocity and the magnetic field inclination. However, not always is observed that areas with high LOS velocities have strong magnetic field strength. We have also found that those patches crossing the outer penumbral border experiment LOS velocity and magnetic field increament, staying inclination unchanged. After that, these enhancements suddenly drop down and the patch blends with the quiet Sun.

Although these patches resemble Evershed clouds (e. g., Shine et al., 1994; Rimmele, 1994; Cabrera Solana et al., 2006, 2007), we do not found any indication of two velocity packages inside the patch travelling outward as a whole. Besides, Cabrera Solana et al. (2007) found that each package of the Evershed cloud has an opposite magnetic polarity when crossing the border of the sunspot, which has not been detected in any of our examples.

We suggest that the Evershed flow returns back to the solar surface at the end of flow channels. When this downflow has supersonic velocities and reaches denser layers, it is abruptly stopped producing a shock. As a consequence of that shock, there is an enhancement of temperature that is

manifested above as bright intensity structures.

6

Conclusions and Future work

Nous avons toute la vie pour nous amuser
et toute la mort pour nous reposer.
Georges Moustaki

In this thesis we have characterized the physical properties of the small-scale flows present in sunspot penumbrae and their temporal evolution. To this aim, we used a time sequence of nearly diffraction-limited spectropolarimetric scans of the Fe I 6173 Å line taken with the CRISP instrument at the Swedish 1-m Solar Telescope. This chapter summarizes the conclusions obtained in the thesis and draw our future work plans.

In order to carry out an in-depth study of how mass moves in the smallest scales of the penumbra, we use time sequences of high cadence, spatial resolution spectropolarimetric data that satisfy stringent requirements. These are needed to study the temporal evolution of spatially-resolved penumbral structures and to infer their physical properties in an unprecedented way. We have used the Fe I 6173 Å spectral line which is very narrow, so very sensitive to velocities, and has a perfectly flat and clean red continuum. Although this may not be of prime importance, is also relevant. Finally, the observed sunspot was located very close to the disk center. In that position, the velocity field is less affected by projection effects (i. e., the strong Evershed flow) and vertical motions are mostly represented.

For the first time, we report the ubiquitous presence of lateral downflows in penumbral filaments without stray light compensating data. For this purpose, we compute Dopplergrams at different heights from the observed intensity profiles using line bisectors and filter them for subsonic oscillations. Lateral downflows are observed as elongated redshifted patches at the edges of the upflowing penumbral filaments. Their temporal evolution

can be summarized as:

- Lateral downflows are mostly located in dark areas close to penumbral filaments, but sometimes they appear on bright filament edges.
- Lateral downflows have an intermittent life and undergo mergings and fragmentations quiet frequently. Furthermore, they seem to follow the same wiggle of the filaments they are associated with. We suggest that forces derived from horizontal pressure balance might be responsible for this behavior.
- The LOS velocity of the lateral downflows ranges between 150 and 300 m s^{-1}. Maximum values of order 500 m s^{-1} have been detected in some cases. Besides, their mean LOS velocity increases as a function of depth.
- After compensating our data for different stray light levels, we have observed that lateral downflows detected in the original data are found at the same location as in stray light compensated data, but with enhanced LOS velocity. Therefore, at least those lateral downflows coinciding in stray light compensated and in original data are not produced by mathematical artifacts.

Our observations suggest that penumbral filaments can be understood as elongated convective cells with upflows along their length, weak downflows at the edges and a strong downflow at the end. Therefore, in the azimuthal direction of the penumbral filaments, matter from neighboring cells is strongly squeezed and allowed to fall down. The evolution of the penumbral velocity field is similar to that of the quiet Sun, and supports the existence of overturning convection in the penumbra (Scharmer et al., 2008). However, from a kinematical point of view, this scenario is also compatible with other theoretical scenarios, such as the convective rolls models (Danielson, 1961) or the twisted horizontal magnetic flux tubes (Borrero, 2007). Distinguishing between the different theoretical scenarios requires the analysis of the magnetic field vector in penumbral filaments.

In order to continue with the physical characterization of the lateral downflows, we have inferred the magnetic field vector of the detected lateral downflows carrying out an one-component inversion of the four Stokes profiles of the Fe I 6173 Å line. The magnetic and kinematic properties of the lateral downflows are summarized as:

- Most of the lateral downflows last less than 6 minutes. Their median lifetime is 3.2 minutes.
- Lateral downflows show a median length of $0\farcs53$ and a width of $0\farcs16$. Therefore, high spatial resolution is really needed to detect them.

- In the inner and middle penumbra, the downflowing patches move outward with a median horizontal speed of 85 m s^{-1}.
- The magnetic field strength of the center of blueshifted channels is of order 1000 G while is around 1600 G in the lateral downflows, in the inner penumbra. However, we observe the inverse behavior in other penumbral regions. The median value of the magnetic field strength of the lateral downflows is 1500 G.
- The median value of the magnetic field inclination of the lateral downflows is$\sim$135°. They do not show polarity reversals. However, some Stokes V profiles show an additional red lobe that suggests the presence of opposite polarity fields.
- The magnetic field azimuth has a spatial distribution that might be in agreement with what is expected for magnetoconvection.

We have compared our results with those obtained from recent 3D MHD simulations (Rempel, 2012). The main difference is that LOS velocities obtained from observed lateral downflows are significantly smaller than those from simulations, which remains also after stray light compensation. This discrepancy arises doubts about the association of the lateral downflows with overturning convection. In consequence, we cannot to discard the other theoretical scenarios previously suggested. We notice that simulations show a polarity reversal between $\tau = 1$ and 0.1 at the position of the lateral downflows, suggesting that penumbral observations are needed to relate lateral downflows with polarity reversal areas.

Finally, although supersonic Evershed downflows have been studied before, we have performed an analysis to describe the temporal evolution and the physical properties of spatially-resolved supersonic Evershed downflows. For this purpose, we have considered information from some observables (as the continuum intensity filtergrams, LOS velocities given by the Stokes V zero-crossing wavelength and the ichimotograms) combined with the LOS velocity and the magnetic field vector of the patches harboring supersonic Evershed downflows obtained from two-component inversions of the four Stokes profiles of the Fe I 617.3 nm line.

Supersonic Evershed downflows are detected inside compact patches moving outwards. These patches are present at different locations between the mid and outer penumbra and observed as bright structures located at the end of filamentary structures. The lifetimes of the analyzed supersonic Evershed downflow vary from one to more than ten minutes. Their main physical properties are the following:

- Most of the supersonic Evershed downflows show a LOS velocity between 7.5 and 9.5 km s^{-1}, with a median value of 8 km s^{-1}. Their LOS velocity increases until a peak value, fading some frames later.

- Their magnetic field lines tend to be more vertical than other pixels inside the patch, with a median of 45°. Thus, the polarity of the magnetic field related to the supersonic Evershed downflows is opposite to that of the sunspot.

- The magnetic field strength of the supersonic Evershed downflows has a median value of 1.5 kG.

- Supersonic downflows tend to be cospatial with bright pixels, with a median value of the continuum intensity of 0.91.

We have observed that patches have two different behaviors after the vanishing of the supersonic velocity: the patch disappears or it is still visible and there occur another supersonic downflow some frames after. Besides, patches also suffer mergings and fragmentations. When patches merge, the LOS velocity increases as well as the magnetic field inclination and the continuum intensity, but the magnetic field strength remains unchanged. This indicates that the Evershed flow associated to different filaments are mixed, returning together to the solar surface. In the case of fragmentations, the intensity structure brightens and boosted outward. At that moment, the supersonic downflow heads the structure breaking the patch. There are also patches that cross the outer penumbral border experimenting LOS velocity and magnetic field increment, staying inclination unchanged. After that, these enhancements suddenly drop down and the patch blends with the quiet Sun.

According to these results, we suggest that supersonic Evershed downflows are suddenly stopped in denser layers below producing a shock. As a consequence of this shock, there is an enhancement of temperature that travels upward and manifestates as a brighter intensity structure.

From this thesis we can extract that lateral downflows exist in sunspot penumbrae. This is a relevant result since it supports some theoretical models intensively debated. However, other models need to be reformulated to consider the presence of lateral downflows. Also, the detection of lateral downflows corroborates that simulations are on the right track, although some discrepancies have appeared. In addition, we have physically characterized supersonic Evershed downflows and followed them during their lifetime. At high-resolution, these structures are more intriguing than it was expected. In fact, our results suggest that they play an important role in denser layers below that needs to be study in depth.

Maybe, the key to know how matter moves in the penumbra is hiden in the azimuthal component of the velocity field of the penumbral filaments. It is thought that twisting motions may be the tracers of the azimuthal component of the velocity field. These features were discovered as a new type of dark lanes along penumbral filaments a few months after the Hinode launch

in 1996. Although we attempted to analyze twisting motions (Esteban Pozuelo, 2012), the used data had some problems related to the reduction process. We think that this is an interesting way to continue resolving the penumbral problem.

From the study of supersonic Evershed downflows and simulations of penumbral filaments, we have noticed that processes occurring at deeper layers affect to the observed penumbral structures. Therefore, another future analysis could be based on deep layers observations to shed light on what it is happening just below penumbral filaments.

Bibliography

Beck, C. (2011), *A&A* **525**, A133.

Beckers, J. M. (1977), *ApJ* **213**, 900–905.

Bellot Rubio, L. R. (2010), The Evershed Flow and the Brightness of the Penumbra, *in* S. S. Hasan & R. J. Rutten, eds, 'Magnetic Coupling between the Interior and Atmosphere of the Sun', p. 193.

Bellot Rubio, L. R., Balthasar, H. & Collados, M. (2004), *A&A* **427**, 319–334.

Bellot Rubio, L. R., Balthasar, H. & et al. (2003), *A&A* **403**, L47.

Bellot Rubio, L. R., Collados, M., Ruiz Cobo, B. & Rodríguez Hidalgo, I. (2002), *Nuovo Cimento C Geophysics Space Physics C* **25**, 543.

Bellot Rubio, L. R., Langhans, K. & Schlichenmaier, R. (2005), *A&A* **443**(1), 7–10.

Bellot Rubio, L. R., Schlichenmaier, R. & Langhans, K. (2010), *ApJ* **725**, 11–16.

Bharti, L., Schüssler, M. & Rempel, M. (2011), 2011arxiv1107.0398B.

Biermann, L. (1941), *VAG* **76**.

Borrero, J. M. (2007), *A&A* **471**, 967–975.

Borrero, J. M. & Ichimoto, K. (2011), *Living Review Solar Physics* **8**(4).

Borrero, J. M., Lagg, A., Solanki, S. K. & Collados, M. (2005), *A&A* **436**, 333–345.

Brault, J. & Neckel, H. (1987), 'Spectral atlas of solar absolute disk-averaged and disk-center intensity from 3290 to 12510 å'.

Brekke, K. & Maltby, P. (1963), *Annales d'Astrophysique* **26**, 383.

Bumba, V. (1960), *Izv. Krim Astr. Obs* **23**(212).

Cabrera Solana, D., Bellot Rubio, L. R., Beck, C. & del Toro Iniesta, J. C. (2006), **649**, L41–L44.

Cabrera Solana, D., Bellot Rubio, L. R., Beck, C. & del Toro Iniesta, J. C. (2007), *A&A* **475**, 1067–1079.

Cabrera Solana, D., Bellot Rubio, L. R. & del Toro Iniesta, J. C. (2005), *A&A* **439**, 687.

Casini, R., de Wijn, A. G. & Judge, P. G. (2012), *ApJ* **757**(1), 45.

Collados, M., Rodríguez Hidalgo, I., Bellot Rubio, L. R., Ruiz Cobo, B. & Soltau, D. (1999a), TIP (Tenerife Infrared Polarimeter): a near IR full Stokes Polarimeter for the German Solar Telescopes at Observatorio del Teide, *in* R. E. Schielicke, ed., 'Astronomische Gesellschaft Meeting Abstracts', Vol. 15 of *Astronomische Gesellschaft Meeting Abstracts*, p. 13.

Cowling, T. G. (1953), p. 532.

Danielson, R. E. (1961), *ApJ* **134**, 289.

de Boer, C. R., Kneer, F. & Nesis, A. (1992), *A&A* **257**, L4.

de la Cruz Rodríguez, J. (, private communication).

de la Cruz Rodríguez, J., Löfdahl, M. G., Sütterlin, P., Hillberg, T. & Rouppe van der Voort, L. (2015), *A&A* **573**, A40.

de la Cruz Rodríguez, J., Rouppe van der Voort, L., Socas-Navarro, H. & van Noort, M. (2013), *A&A* **556**.

del Toro Iniesta, J. C., Bellot Rubio, L. R. & Collados, M. (2001), *ApJL* **549**, L139–L142.

Dialetis, D., Mein, P. & Alissandrakis, C. E. (1985), *A&A* **147**, 93–102.

Elmore, D. F., Lites, B. W. & Tomczyk, S. e. a. (1992), The Advanced Stokes Polarimeter - A new instrument for solar magnetic field research, *in* D. H. Goldstein & R. A. Chipman, eds, 'Polarization Analysis and Measurement', Vol. 1746 of *Society of Photo-Optical Instrumentation Engineers (SPIE) Conference Series*, pp. 22–33.

Esteban Pozuelo, S. (2012), Master's thesis, Universidad de Granada.

Esteban Pozuelo, S., Bellot Rubio, L. R. & de la Cruz Rodríguez, J. (2015), *ApJ* **803**, 93.

Evershed, J. (1909), *MNRAS* **69**, 454.

Franz, M. (2011), PhD thesis, Kiepenheuer Institut für Sonnenphysik.

Franz, M. & Schlichenmaier, R. (2009), *A&A* **508**(1453).

Franz, M. & Schlichenmaier, R. (2013), *A&A* **550**, A97.

Gonsalves, R. A. (1982), *Opt. Eng.* **21**(5), 829.

Hale, G. E. (1908), *ApJ* **28**, 315.

Heinemann, T., Nordlund, A. . & Scharmer, G. B. (2007), *ApJ* **669**, 1390–1394.

Henriques, V. (2012).
URL: *http://dx.doi.org/10.1051/0004-6361/201220344*

Henriques, V. M. J. (2013), PhD thesis, Stockholm University.

Hirzberger, J. & Kneer, F. (2001), *A&A* **378**, 1078–1086.

Holmes, J. (1961), *MNRAS* **122**, 301.

Ichimoto, K., Shine, R. A., Lites, B. & Kubo, M. (2007b), *PASJ* **59**, 593.

Ichimoto, K., Suematsu, Y. & Tsuneta, S. e. a. (2007a), *Science* **318**(1597).

Jahn, K. & Schmidt, H. U. (1994), *A&A* **290**, 295–317.

Joshi, J., Pietarila, A. & Hirzberger, J. e. a. (2011), *ApJL* **734**(1).

Jurcák, J., Bellot Rubio, L. R. & Ichimoto, K. e. a. (2007), *PASJ* **59**, 601–606.

Keller, C. U. & von der Lühe, O. (1992), *A&A* **261**, 321–328.

Kentischer, T. J., Schmidt, W., Sigwarth, M. & Uexkull, M. V. (1998), *A&A* **340**, 569–578.

Kitiashvili, I. N., Kosovichev, A. G., Wray, A. A. & Mansour, N. N. (2009), *ApJL* **700**, L178–L181.

Kosugi, T., Matsuzaki, K., Sakao, T., Shimizu, T. & Sone, Y. e. a. (2007), *Solar Physics* **243**.

Küveler, G. & Wiehr, E. (1985), *A&A* **142**, 205–211.

Lites, B. W. (1987), *Appl. Opt.* **26**, 3838.

Lites, B. W., E. D. F. S. K. (2001), The solar-b spectro-polarimeter, *in* M. Sigwarth, ed., '20th International Sacramento Peak Summer Workshop, Advanced Solar Polarimetry - Theory, Observation, and Instrumentation', Vol. 236, ASP Conference Series, pp. 33–40.

Lites, B. W., Elmore, D. F., Seagraves, P. & Skumanich, A. P. (1993), *ApJ* **418**(928).

Livingston, W. C. & Harvey, J. (1975), A New Component of Solar Magnetism - The Inner Network Fields, *in* 'Bulletin of the American Astronomical Society', Vol. 7 of *Bulletin of the American Astronomical Society*, p. 346.

Löfdahl, M. G. (1996), PhD thesis, Stockholm University.

Löfdahl, M. G. (2002), *Proc SPIE.* (4796), p.146.

Löfdahl, M. G. & Scharmer, G. B. (1994), *A&A Suppl.* **107**, 243.

Löfdahl, M. G. & Scharmer, G. B. (2012), *A&A* **537**, A80.

Löfdahl, M. G., van Noort, M. J. & Denker, C. (2007), *in* F. Kneer, K. G. Puschmann & A. D. Wittmann, eds, 'Modern Solar Facilities - Advanced Solar Science'.

Maltby, P. (1964), *Astrophysica Norvegica* **8**, 205.

Martínez Pillet, V., Collados, M. & Sánchez Almeida, J. e. a. (1999), Lpsp & tip: Full stokes polarimeters for the canary islands observatories, *in* T. R. Rimmele, K. S. Balasubramaniam & R. R. Radick, eds, 'High Resolution Solar Physics: Theory, Observations, and Techniques', Vol. 183 of *Astronomical Society of the Pacific Conference Series*, p. 264.

Mathew, S. K., Lagg, A., Solanki, S. K., Collados, M., Borrero, J. M., Berdyugina, S., Krupp, N., Woch, J. & Frutiger, C. (2003), **410**.

Meyer, F. & Schmidt, H. U. (1968), *Mitteilungen der Astronomichen Gesellschaft* **25**(194).

Montesinos, B. & Thomas, J. H. (1997), *Nature* **390**, 485–487.

Müller, R. (1973), *Sol. Phys.* **29**, 55–73.

Noll, R. J. (1976), *J. Opt. Soc. Am.* **66**(3), 207–211.

Norton, A. A., Graham, Pietarila, J., Ulrich, R. K., Schou, J., Tomczyk, S., Liu, Y., Lites, B. W., López Ariste, A., Bush, R. I. & Socas-Navarro, H. (2006), *Solar Physics* **239**(1-2), 69–91.

Ortiz, A., Bellot Rubio, L. R. & Rouppe van der Voort, L. (2010), *ApJ* **713**(1282).

Parnell, C. E. (2002), *MNRAS* **335**, 389–398.

Paxman, R. G., Schulz, T. J. & Fienup, J. R. (1992), *J. Opt. Soc. Am.* **9**(7), 1072.

Pesnell, W. D., Thompson, B. J. & Chamberlin, P. C. (2012), *Sol. Phys.s* **275**, 3–15.

Rempel, M. (2011a), 3D numerical MHD modeling of sunspots with radiation transport, *in* D. Prasad Choudhary & K. G. Strassmeier, eds, 'IAU Symposium', Vol. 273 of *IAU Symposium*, pp. 8–14.

Rempel, M. (2011b), *ApJ* **729**(1).

Rempel, M. (2011c), *ApJ* **740**, 15.

Rempel, M. (2012), *ApJ* **750**, 62.

Rempel, M., Schüssler, M., Cameron, R. H. & Knölker, M. (2009a), *Science* **325**(171).

Rempel, M., Schussler, M. & Knolker, M. (2009b), *ApJ* **691**, 640–649.

Rezaei, R., Schlichenmaier, R., Beck, C. & Bellot Rubio, L. R. (2006), *A&A* **454**, 975–982.

Rimmele, T. & Marino, J. (2006), *ApJ* **646**.

Rimmele, T. R. (1994), **290**, 972–982.

Rimmele, T. R. (1995).

Roddier, N. A. (1990), *Opt. Eng.* (29), 1174–1180.

Rouppe van der Voort, L., Löfdahl, M. G., Kiselman, D. & Scharmer, G. B. (2004), *A&A* **414**(2), 717–726.

Ruiz Cobo, B. & Asensio Ramos, A. (2013), *A&A* **549**, L4.

Ruiz Cobo, B. & Bellot Rubio, L. R. (2008), *A&A* **488**, 749–756.

Ruiz Cobo, B. & del Toro Iniesta, J. C. (1992), *ApJ* **398**, 375.

Scharmer, G. B. (2006), *A & A* **447**, 1111.

Scharmer, G. B. (2014), *A&A* **561**, A31.

Scharmer, G. B., Bjelskjo, K., Korhonen, T. K., Lindberg, B. & Petterson, B. (2003a), *Proc SPIE* **4853**(341).

Scharmer, G. B., de la Cruz Rodríguez, J., Sütterlin, P. & Henriques, V. M. (2013), *A&A* **553**, A63.

Scharmer, G. B., Dettori, P. M., Löfdahl, M. G. & Shand, M. (2003b), *Proc SPIE* **4853**(370).

Scharmer, G. B. & Henriques, V. M. J. (2012), *A&A* **540**, A19.

Scharmer, G. B., Henriques, V. M. J., Kiselman, D. & de la Cruz Rodríguez, J. (2011), *Science* **333**(6040).

Scharmer, G. B., Nordlund, A. & Heinemann, T. (2008), *ApJL* **677**, L149.

Scharmer, G., Gudiksen, B. V., Kiselman, D., Löfdahl, M. G. & Rouppe van der Voort, L. (2002), *Nature* **420**, 151–152.

Scharmer, G. & Spruit, H. C. (2006), *A&A* **460**, 605–615.

Scherrer, P. H., Schou, J. & Bush, R. I. e. a. (2012), *Solar Physics* **275**, 207–227.

Schlichenmaier, R. (2002a), *Astronomische Nachrichten* **323**, 304–308.

Schlichenmaier, R. (2003), *ASP Conference Series* **286**, 211–225.

Schlichenmaier, R. & Collados, M. (2002b), *A&A* **381**, 668–682.

Schlichenmaier, R. & Franz, M. (2013), *A&A* **555**, A84.

Schlichenmaier, R., Jahn, K. & Schmidt, H. U. (1998), *ApJ* **493**, 121–124.

Schlichenmaier, R. & Schmidt, W. (2000), *A&A* **358**, 1122.

Schnerr, R. S., de la Cruz Rodríguez, J. & van Noort, M. (2011), *A&A* **534**(A45).

Schou, J., Scherrer, P. H. & Bush, R. I. e. a. (2012), *Solar Physics* **275**, 229–259.

Schulz, T. J. (1993), *J. Opt. Soc. Am. A* **10**(5), 1064–1073.

Schüssler, M. & Vögler, A. (2006), *ApJ* **641**, 73–76.

Selbing, J. (2005), Master's thesis, Stockholm University.

Sheeley, N. R. (1972), *Sol. Phys.* **25**, 98–103.

Shine, R. A., Title, A. M., Tarbell, T. D., Smith, K., Frank, Z. A. & Scharmer, G. (1994), **430**, 413–424.

Smithson, R. C. (1975), Observations of Weak Solar Magnetic Fields with the Lockheed Diode Array Magnetograph, *in* 'Bulletin of the American Astronomical Society', Vol. 7 of *Bulletin of the American Astronomical Society*, p. 346.

Sobotka, M. & Sütterlin, P. (2001), *A&A* **380**, 714–718.

Solanki, S. K. (2003), *The Astronomy and Astrophysics Review* **11**(2-3), 153–286.

Solanki, S. K. & Montavon, C. A. P. (1993), *A&A* **275**(283).

Solanki, S. K., Montavon, C. A. P. & Livingston, W. (1994), *A&A* **283**, 221–231.

Solanki, S. K., Rüedi, I. & Livingston, W. (1992), *A&A* **263**, 339–350.

Spruit, H. C. (1981), Small scale phenomena in umbras and penumbras - The role of convective processes, *in* L. E. Cram & J. H. Thomas, eds, 'The Physics of Sunspots', pp. 359–368.

Spruit, H. C. & Scharmer, G. (2006), *A&A* **447**, 343–354.

Stein, R. F. & Nordlund, A. (1998), *ApJ* **499**(2), 914.

Stellmacher, G. & Wiehr, E. (1971), *Solar Physics* **17**, 21–30.

Stix, M. (2002), *The Sun.*, Springer.

Straus, T., Deubner, F. L. & Fleck, B. (1992), *A&A* **256**, 652.

Stürenburg, S. & Holweger, H. (1990), *A&A* **237**, 125–136.

Sütterlin, P., Bellot Rubio, L. R. & Schlichenmaier, R. (2004), *A&A* **424**, 1049–1053.

Sánchez Almeida, J. (2005), *ApJ* **662**, 1292–1313.

Sánchez Almeida, J. (2009), *"Magnetic Coupling between the Interior and the Atmosphere of the Sun", eds. S. S. Hasan & R. J. Rutten, Astrophysics and Space Science Proceedings, Springer-Verlag* .

Sánchez Almeida, J. & Lites, B. W. (1992), *ApJ* **398**, 359–374.

Sánchez Almeida, J. & Lites, B. W. (2000), *ApJ* **532**, 1215–1229.

Sánchez, F., Collados, M. & Vázquez, M. (1991), *Solar Observations: Techniques and Interpretation.*, Cambridge University Press.

Thonhofer, S., Bellot Rubio, L. R. & Utz, D. e. a. (2015), Parallelization of the sir code for the investigation of small-scale features in the solar photosphere, *in* K. N. Nagendra, S. Bagnulo, R. Centeno & M. J. Martínez González, eds, 'Polarimetry: From the Sun to Stars and Stellar Enviroments', Proceedings IAU Symposium No. 305. arXiv:1503.03710v1.

Title, A. M., Tarbell, T. D., Topka, K. P., Ferguson, S. H., Shine, R. A. & Team, S. (1989), *ApJ* **336**, 475.

Tiwari, S. K., van Noort, M., Lagg, A. & Solanki, S. K. (2013), *A&A* **557**, A25.

Tsuneta, S., Ichimoto, K. & Katsukawa, I. e. a. (2008), *Solar Physics* **249**(2), 167–196.

Uitenbroek, H., Dumont, N. & Tritschler, A. (2012), The Influence of Molecular Lines on the Measurement of Photospheric Velocities, *in* T. R. Rimmele, A. Tritschler, F. Wöger, M. Collados Vera, H. Socas-Navarro, R. Schlichenmaier, M. Carlsson, T. Berger, A. Cadavid, P. R. Gilbert, P. R. Goode & M. Knölker, eds, 'Second ATST-EAST Meeting: Magnetic Fields from the Photosphere to the Corona.', Vol. 463 of *Astronomical Society of the Pacific Conference Series*, p. 99.

van der Noort, M., Rouppe van der Voort, L. & Löfdahl, M. G. (2005), *Solar Physics* **228**, 191.

van Noort, M. (2012), *A&A* **548**, A5.

van Noort, M., Lagg, A., Tiwari, S. K. & Solanki, S. K. (2013), *A&A* **557**, A24.

van Noort, M. & Rouppe van der Voort, L. (2008), *A&A* **489**(429).

von der Lühe, O. (1993), *A&A* **268**, 374.

Watanabe, H., Bellot Rubio, L. R., de la Cruz Rodríguez, J. & Rouppe van der Voort, L. (2012), *ApJ* **757**(1), 49.

Welsch, B. T. & Longcope, D. W. (2003), *ApJ* **588**, 620.

Westendorp Plaza, C., del Toro Iniesta, J. C., Ruiz Cobo, B. & Martínez Pillet, V. (2001), *ApJ* **547**(2), 1148–1158.

Westendorp Plaza, C., del Toro Iniesta, J. C., Ruiz Cobo, B., Martínez Pillet, V., Lites, B. & Skumanich, A. (1997), *Nature* **389**(47-49).

Wiehr, E. (1995), *A&A* **298**, L17.

Wiehr, E., Knölker, M., Grosser, H. & Stellmacher, G. (1986), *A&A* **155**, 402–406.

Yau, K. K. (1988), PhD thesis, University of Durham.

Zodet, H. (2015), 'Esocast 76: A polarised view of stellar magnetism', URL: http://www.eso.org/public/announcements/ann15071/.